Direct wafer bonding dynamics

Etienne Navarro

UNIVERSITÉ DE GRENOBLE

THÈSE

Pour obtenir le grade de

DOCTEUR DE L'UNIVERSITÉ DE GRENOBLE

Spécialité : **Matériaux, Mécanique, Génie civil, Electrochimie (2MGE)**

Arrêté ministérial : 7 août 2006

Présentée par

Etienne NAVARRO

Thèse dirigée par **Yves BRÉCHET**

préparée au sein du **SIMaP**
Laboratoire de Science et Ingénierie des Matériaux et Procédés
et de **l' École doctorale IMEP-2**

Dynamique de l'assemblage de wafers par adhésion moléculaire

Direct Wafer Bonding Dynamics

Thèse soutenue publiquement le **19/05/2014**,
devant le jury composé de :

Prof. Kevin. T. TURNER
University of Pennsylvania, Rapporteur
Prof. Dominique LEGUILLON
Université Pierre et Marie Curie (UPMC, Paris 6), Rapporteur
Prof. Elisabeth BOUCHAUD
École supérieure de physique et de chimie industrielles de la ville de Paris (ESPCI), Examinatrice
Prof. Yves BRÉCHET
Institut polytechnique de Grenoble (Grenoble-INP), Directeur de thèse
Prof. Thomas PARDOEN
Université Catholique de Louvain (UCL), Co-Encadrant de thèse
Prof. Jean-Pierre RASKIN
Université Catholique de Louvain (UCL), Co-Encadrant de thèse
Dr. Ionut RADU
R&D Soitec, Co-Encadrant de thèse
Dr. François RIEUTORD
CEA Grenoble, Invité

Abstract

The direct wafer bonding process involves a coupled physical system, formed by the elastic deformation of the wafers and a thin layer of fluid trapped in-between the two wafers. Dynamics of the system during the contacting step has many practical consequences on the quality of the assembled stack. A model for the bonding dynamics is formulated using the thin plate theory and the Reynolds equation. The transient equation is solved numerically, allowing to study both the initiation and the propagation of the bonding. The model is supported by the measurement of the vertical movement of the wafer during the bonding, using an original setup involving optical sensors. Subsequently, an analytical model for the final curvature of the bonded stack is derived, as a function of the different load components acting on the wafers during the bonding, using the thin plate theory and by considering a transverse strain discontinuity locked at the bonding interface. Experimental validation is performing using two different wafer thicknesses. The measured bonded wafer profiles are well described by the model. In addition, a model for the work of adhesion is developed, taking into account both the interface roughness and the amount of adsorbed water. The interface energy controlling the adhesion is found different than for the separation because of the different distribution of water along the interface, in agreement with the experimental observations. At last, a new method to accurately measure the work of adhesion for the entire wafers geometry is proposed, using an elongated bubble intentionally created at the bonding interface and by measuring the induced wafer deflection.

Résumé

Lors de l'assemblage de wafers par adhésion moléculaire, un mince film d'air est piégé entre les deux wafers, créant ainsi un système fluide/structure couplé. La qualité finale de l'assemblage dépend fortement de la dynamique de ce système. L'initiation et la propagation du collage ont été étudiées, en régime transitoire, en utilisant un modèle de plaques minces couplée avec l'équation de Reynolds. La résolution numérique de l'équation, ainsi que la mesure optique du déplacement vertical de la plaquette durant le collage, nous a permis de valider le modèle et de mieux comprendre la dynamique du collage. Dans la continuité de cette étude, nous avons proposé une expression analytique de la courbure finale de l'assemblage en fonction des forces en jeu pendant le collage, ceci en utilisant à nouveau la théorie des plaques minces et en considérant l'existence d'un saut de déformation transverse le long de l'interface collée. Ce modèle a été validé par une expérience, impliquant le collage de wafers d'épaisseur différentes et en prenant soin de contrôler l'ensemble des forces agissant sur ces wafers. Nous observons une influence importante du film d'air sur la forme finale des wafers. En complément, un modèle du travail d'adhésion a été développé prenant en compte, à la fois, la rugosité d'interface et la quantité d'eau adsorbée. La différence de répartition de l'eau à l'interface de collage, nous permet d'expliquer les résultats expérimentaux montrant des valeurs d'énergie de séparation supérieure à celle de l'adhésion. Enfin, nous proposons une nouvelle méthode de mesure du travail d'adhésion pour la géométrie entière des wafers, utilisant la mesure de la taille d'une bulle cylindrique intentionnellement créée, par un petit objet, à l'interface de collage.

Contents

Acknowledgements

Je tiens à remercier, tout d'abord, l'ensemble des membres du jury d'avoir accepté d'évaluer ce travail et de venir à Grenoble (certains d'assez loin) pour assister à la soutenance.

Ensuite, je souhaite remercier mon directeur de thèse, Yves Bréchet, pour toute l'aide apportée et le temps consacré pendant les nombreuses réunions de travail, entre autres au Bureau des Longitudes, ou des traversées de Paris comme dans les films et surtout pour avoir été toujours disponible (particulièrement le weekend). Je remercie chaleureusement Thomas et Jean-Pierre pour les nombreux échanges, remarques et questions que l'on a eu au cours de ces mêmes réunions. Je vous remercie pour toutes les corrections sur le manuscrit et sur les articles, et aussi pour vos encouragements.

J'ai pu mener à bien ce projet et travailler sereinement à Soitec grâce à Ionut et Alexandre, et je les en remercie. Cela a été un réel plaisir de travailler quotidiennement ensemble. Ionut, je suis toujours impressionné par ta capacité d'organisation et de prise de décision. Merci aussi pour avoir fait les nombreux aller-retour à Paris et en Belgique. Alexandre, merci beaucoup pour toute l'aide apportée au cours du projet, toutes les discussions techniques et les autres. J'adresse un grand merci à Christophe les très précieuses aides techniques apportées, ainsi que les sorties d'escalades et de ski! Encore un immense merci à vous deux. Je vous souhaite le meilleurs pour la suite! Je remercie également toutes les autres les personnes côtoyées à Soitec: William, Laurent, Didier, Yann, Oleg, Marcel, Arnaud, Luciana, Yves-Mathieu, Christophe, Jean-Marc, Gaël, Fréderic, Philipp, Fabrice, Daniel, Cécile, Fanny, Sébastien, les stagiaires et alternants et tous les autres. J'adresse tous mes encouragements aux thésards restants, en espérant quand même qu'ils ne seront pas les derniers à Soitec, Raphaël, Guillaume, Xavier et Mehdi, bonne chance!

Enfin, un immense merci à Pablo, qui est en réalité co-auteur de la thèse. Ces trois années ont vraiment été superbes autant pour le travail que pour tout le reste et c'est, en très très grande partie, grâce à toi. Pour l'escalade, les haut plateaux de la Chartreuse, toutes les sorties de ski, toutes les bières et soirées. Et aussi, pour tous les soirs au boulot à être les derniers du troisième étage, à se prendre la tête sur la courbure d'une poutre, la diffusion du silicium ou la compilation latex, et pour conclure, en général, que cela dépend de la fréquence. Je remercie chaleureusement Onitza pour l'énergie, l'escalade et les soirées. Bon courage pour la suite! De même, un très grand merci à Damien. C'est bête que l'on n'est pas trouvé le temps de grimper plus souvent la dernière année, et aussi que l'on n'ai jamais vraiment eu la possibilité de discuter sérieusement de collage (c'est quoi déjà, le sujet de ta thèse ?).

Finalement, je remercie tous mes coloc: Corentin, Adrien, Julien, Floriane, Amélie, Sylvain, mes parents Jean, Odette, mon frère Emmanuel, et sans oublier Sarah et Nina!

Merci à vous!

General Introduction

Direct bonding is related to the spontaneous adhesion between solids. “Direct” stands for “without glue” or “without any intermediate adhesive materials”. Direct adhesion between solids does usually not occur because surfaces are too rough or too dusty to allow effective and wide contact area. However, with sufficiently flat and clean surfaces, direct bonding is possible with most materials.

Silicon based semiconductor wafers constitute the main raw material used to fabricate electronic devices and integrated circuits. They are made of thin disks from a few centimeters up to 45 centimeters in diameter and less than one millimeter in thickness. Because of the high quality required in microelectronics, standard single crystalline silicon wafers can be directly bonded together, without much additional precautions.

The direct wafer bonding technology has received a recrudescence of interest since it has been used to fabricate silicon-on-insulator wafers (SOI), and it is nowadays introduced in many other advanced applications, involving for example III-V compounds or processed electronic devices. In addition, many physical phenomena unique to the direct bonding of materials, make it a rich and fascinating scientific research topic.

However, industrial process improvement, as the use of direct wafer bonding for future applications, requires better fundamental understanding of the physics involved in the process. In particular, mechanical deformation of the wafers during the bonding has become critical, since for instance, high alignment and very low pattern distortion are required for circuit layer bonding.

A thin air layer remains trapped in between two wafers when they are brought close to each other. The direct contact is, then, prevented. Nonetheless, the strong adhesion forces between the wafers are able to squeeze and expelled out the thin viscous air layer, leading to a bonding front propagation. While the contacted area expands through the entire wafers area, the wafers are significantly deformed by both the fluid pressure and by the strong adhesion forces. Therefore, the bonding process is dynamic and transient, and leads to an interesting coupled system, formed by the fluid flow, the mechanical deflection of the wafers, and by the adhesion forces.

The objective of the thesis is to investigate experimentally and to contribute to better model description of the underlying physics involved in the dynamics of the direct wafer bonding process.

Both experimentation and modeling efforts have been put into the most standard and simple process condition, which is the hydrophilic direct bonding of bulk silicon wafer,

20 cm in diameter, under ambient atmosphere and temperature.

A transient model of the bonding system has been developed, and an experimental method allowing the characterization of the out-of-plane wafer displacement during the bonding has been used. Thanks to the obtained understanding of the bonding dynamics, the influence of the bonding process on the final bonded wafers curvature has been studied and an analytical model has been derived. The proposed explanation, of the final wafers curvatures, has been validated using a simple experimental procedure. The key parameter of these both models is the energy per surface area which drives the bonding dynamics, denoted as the work of adhesion. It is therefore important to understand its physical dependence on the structural and physico-chemical effects, as well as to precisely measure its value. For this reason, a theoretical description of the interface adhesion has be derived, based on previous molecular dynamics simulation results. In addition, a new experimental procedure, allowing an accurate measurement of the work of adhesion between entire wafers has been suggested.

The manuscript is structured in four chapters. Chapter I includes the state-of-the-art of direct wafer bonding. In Chapter II, the study about the bonding dynamics, including the bonding front propagation is detailed. Chapter III presents the analysis of the final wafer curvatures. And, lastly, in Chapter IV, a theoretical description of the work of adhesion, and a measurement method specific to the wafer geometry, are proposed. Each chapter is made of a theoretical part, followed by the experimental study. Then the results are presented, and discussed. At last, perspectives are suggested in the concluding part.

The present work was supported by the Soitec company, a french semiconductor industry based in Bernin, near Grenoble. The flagship product is Silicon-On-Insulator wafers (SOI), fabricated using the Smart Cut™ technology. This work was carried out within a partnership involving the SIMaP laboratory, based in Grenoble, and the Université catholique de Louvain (UCL), in Belgium.

Notations

a	position of the bonding front (m)
$D = \frac{E\,t^3}{12(1-\nu^2)}$	flexural rigidity of the wafer $(N.m)$
e, t	thickness of the wafer (m)
E	Young's modulus $(N.m^{-2})$
E	bonding energy or work of decohesion $(J.m^{-2})$
$\bar{E} = E/(1-\nu^2)$	plane strain modulus $(N.m^{-2})$
ϵ	elastic strain
Δ	Laplace operator
$\Delta\epsilon$	elastic strain discontinuity at the interface
g	gravity acceleration, $g = 9.81\,m.s^{-2}$
h	vertical position of the wafer (m)
$\dot{h}$	vertical velocity of the wafer $(m.s^{-1})$
h_c	cut-off length of the propagation model (m)
k	curvature of the wafer (m^{-1})
μ	viscosity of the fluid $(Pa.s)$
M	bending moment $(N.m$ or $N)$
N	in-plane force $(N$ or $N.m^{-1})$
ν	Poisson ratio
P	fluid pressure (Pa)
$\phi \in [0,\,1]$	sliding coefficient of the interface
r	radius position (m)
R	radius of the wafer (m)
ρ	density of the wafer $(kg.m^{-3})$
σ_1, σ_2	surface roughness (m)
$\sigma = \sqrt{\sigma_1^2 + \sigma_2^2}$	interface roughness (m)
t	time
w	deflection of the wafer (m)
W	work of adhesion $(J.m^{-2})$
x, y, z	spatial coordinates
$bow = k/2R^2$	deflection of the external wafer edge, assuming the wafer shape is quadratic only : $w(r) = k/2\,r^2$.

Chapter I
State of the Art

Abstract

In this chapter the state of the art of direct wafer bonding is presented. In particular the previous reports on bonding dynamics are highlighted, including the underlying physics of adhesion, the bonding front propagation and the mechanical deformation induced by the bonding process. In addition, a short review about the interplay between elastic deformation and adhesion, and about the bonding interface evolution in time and temperature, is proposed.

Contents

Introduction

The state of the art of direct wafer bonding is presented in six different sections. The first section includes a short review of the history of direct bonding and some examples of modern applications are presented. The following sections present the state of the art related to the three main chapters: the bonding dynamics, the final wafer deformation and the work of adhesion. The two last sections are related to the interplay between elastic deformation and adhesion, and the bonding interface evolution in time and temperature. This two last topics are not further discussed in the thesis. Reading them, is in consequence, not mandatory to understand the developments proposed in this thesis results, but it is still useful to get a global picture of the direct wafer bonding technology.

There are two main reference books about wafer bonding. The first, "Semiconductor Wafer Bonding" by Q.Y. Tong and U. Gösele, published in 1999, is about the physics of direct wafer bonding [1]. The second one, "Wafer bonding, Applications and Technology" by M. Alexe and U. Gösele, published in 2004, deals with the applications of wafer bonding (not only direct bonding) [2]. In addition, comprehensive reviews of direct bonding have been published by A. PlöBl et al. [3] and J. Haisma et al. [4].

It should be noted that "direct bonding" is also known as "fusion bonding" or "molecular bonding".

1 | History of direct bonding and applications

The direct bonding phenomenon is known for a long time. In 1725, J.T. Desaguliers demonstrated cold welding by joining two lead spheres. Bonding as strong as the bulk material was obtained at ambient temperature. Direct bonding of brittle materials was observed for the first time by contacting two well polished glass lenses. Because the light reflection at the interface disappears, due to atomic contact, the original name of direct bonding was "optical contact". The first application of direct bonding was the fabrication of optical devices. Early modern studies were made by J. W. Obreimoff in 1930 and by Lord Rayleigh in 1936 [5, 6]. J. W. Obreimoff has studied the splitting energy of a mica sheet. Lord Rayleigh studied the direct bonding of two polished microscope glass plates and measured both the adhesion and the splitting energy.

Direct bonding gained more interest leading to a great development since 1980 years, because of the specific use for the fabrication of silicon-on-insulator (SOI) substrates. Direct bonding of silicon wafers was first suggested almost simultaneously by M. Shimbo et al. [7] and J. B. Lasky et al. [8]. Both groups reported room temperature silicon bonding followed by high temperature annealing to create covalent bonds across the bonding interface.

The range of applications of direct bonding is wide. Most of the applications are in the area of semiconductor electronic devices, but not only. Here, some examples are selected in order to illustrate the interest of studying the direct wafer bonding. Many more

applications and related developments can be found in the reference book by M. Alexe and U. Gösele [2].

Most layer transfer techniques are based on direct wafer bonding, allowing the transfer of a thin layer of material from a donor wafer to a handle substrate. Most of the time, the layer to be transferred is not self-supporting, i.e. its thickness is less than a few micrometers.

Many layer transfer techniques have been developed: The Smart Cut^{TM} technology is based on ion implantation and thermal fracture activation (see Fig. 1) [9, 10]. The ELTRAN process uses a porous silicon layer and the separation is performed by water jet [11]. Laser lift-off technique consists of the decomposition of a sacrificial layer by a laser beam [2, p. 377]. Several mechanical separation methods have been also proposed, see [12] and [2, p. 473]. When a separation method is not possible, the initial wafer can be grinded and etched back to the desired layer thickness (BESOI [8]).

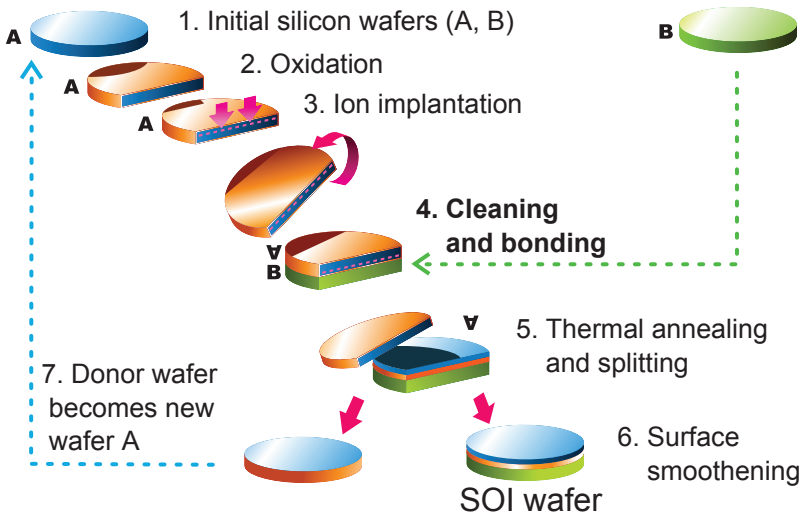

Fig. 1: Schematic representation of the Smart-Cut^{TM} process. The silicon-on-insulator wafer is a silicon wafer having on its surface a thin ($<\sim 1\,\mu m$) single crystalline silicon layer lying over a insulating layer (amorphous silicon oxide).

Because single crystalline material can be transferred, direct wafer bonding can be used as a substitute to the epitaxial growth. More complex structures can be build, since no lattice matching is needed. Recently, the use of direct bonding in the fabrication of high efficient solar cell has been reported [13, 14].

A processed chip may also have to be transferred to a bulk substrate. This is the case, for instance, of the backside illumination sensors application [15]. There, the circuit layer is flipped during the process, in such a way that the incoming light has no more to go through the metallic wiring layers in order to reach the detectors.

Another promising application of the direct bonding is the 3D CMOS integration [16–18]. On a chip, transistors lay typically on a unique plane (thus parallel to the wafer surface). A solution to increase the transistor density, as to achieve more complex function and higher

performance (for example, combine the logic with the memory), is to stack many processed CMOS chips, on top of one another. Many assembly technology have been developed. Direct bonding would allow the highest density integration, since no intermediate layer is needed. An example of three circuit layers stacked together is shown in Fig. 2.

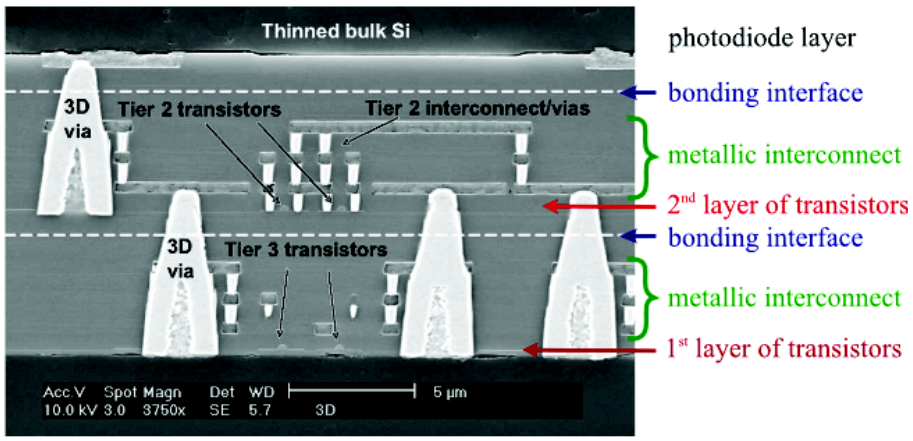

Fig. 2: Cross-sectional scanning electron micrograph (SEM) of three circuit layers stacked by direct wafer bonding (from [16]).

Direct bonding is also used as a building tool for the fabrication of microelectromechanical systems (MEMS) [19–21], often, to hermetically enclose the device. An extreme example of direct wafer bonding application is the building of micro rocket engine or micro gas turbine engine, by stacking, in both cases, up to six silicon wafers [22, 23]. Scaling down engine size is a way to rise the power to weight ratio.

Also, it is worth mentioning the use of direct bonding in order to create a regular dislocation network in a thin silicon film [24–26]. Such system is interesting for fundamental studies, as to elaborate future nanometric devices.

2 | Adhesion

Adhesion constitutes a very wide multidisciplinary field of research with practical impacts on our daily life from adhesion tapes, water capillarity, or natural biological systems such as Gecko lizard (see Fig. 3) [27, 28].

Fig. 3: Gecko lizard adhering to a GaAs semiconductor wafer (from [27]).

First, the variety of intermolecular forces, responsible for the adhesion between materials, are detailed. Subsequently, the specific case of hydrophilic direct bonding is considered. At last, some examples of related studies are provided.

All intermolecular forces originate from the electromagnetic force, among the four known fundamental forces. The simplest is the Coulomb force between two electrically charged particles. More complex interaction forces involve, at least one, no charged particle: between two polar molecules, between a polar molecule and an electric charge and even between two non-polar molecules there is a mutual induced dipoles interaction. They are the van der Waals forces. The strongest type of intermolecular forces involve the metallic and covalent bonds. In this case, the electronic state is shared between the atoms and quantum mechanics is required to explain it.

Hydrogen bonding is the last known class of intermolecular force, as a mix of covalent and electrostatic interactions [29]. It is caused by the strong polarization induced when a high electronegative atom (O, N, F and Cl) is linked to a hydrogen atom. The strength of the hydrogen bond is between 10 and 40 $kJ.mol^{-1}$. This is one order of magnitude stronger than the pure van der Waals force (around 1 $kJ.mol^{-1}$), and one order of magnitude less than the covalent and metallic bonds (around 500 $kJ.mol^{-1}$). Hydrogen bonding is responsible, for instance, for the unique properties of water.

One of the most definitive treatment and presentation of intermolecular forces is certainly the book "Intermolecular and surface forces" written by J. N. Israelachvili [30].

Although the final goal of the direct wafer bonding process is to create covalent bonds between the two wafers, adhesion occurs first through van der Waals or hydrogen bonds. Two different kind of direct bonding are distinguished: hydrophilic bonding and hydrophobic bonding.

Hydrophobic bonding is used for specific applications which require an oxide free interfaces. In this case, the silicon surface is hydrogen-terminated (Si-H) and adhesion occurs through van der Waals forces. When hydrofluoric acid (HF) etching is used to remove the oxide, adhesion can occur through fluor mediated hydrogen bonding.

Hydrophilic bonding uses the strong oxygen mediated hydrogen bond to join the two surfaces. In this case, the bonding involves an oxide layer, as an adsorbed water layer. Hydrophilic bonding is more often used than hydrophobic bonding.

It is interesting to note that covalent bonding can be achieved, at room temperature, under ultra high vacuum condition (UHV) and after a thermal treatment, prior to bonding, allowing the desorption of the hydrogen from the wafer surface [1, p. 277].

The next part of the section focuses on the hydrophilic bonding of silicon wafers, which is the most standard process condition.

Hydrophilic direct bonding. Silicon wafer surfaces are usually covered by an amorphous silicon oxide layer (SiO_2), most of the time, because an oxide is, on purpose, grown on the wafer. Otherwise, a native oxide layer forms naturally on silicon. Water interaction

with a silica surface is widely studied in the literature, well beyond the field of direct bonding [31,32]. Silica is one of the most common material present in nature, and plays an important role in many industrial processes. At room temperature, the silica surface reacts with water to form silanol groups (Si–OH), also called hydroxyl groups. The hydrated surface of silica is hydrophilic. Therefore, one or a few layers of water molecules are physically adsorbed by hydrogen bonds on the silicon oxide. The degree of hydrophilicity is related to the surface density of silanol groups, as to their chemical structure (see Fig. 4). A surface treatment can modify the degree of hydrophilicity, in the form of a thermal pre-treatment or a chemical cleaning (Standard Cleaning SC1 and SC2, or hydrofluoric acid, HF) [1,33–35].

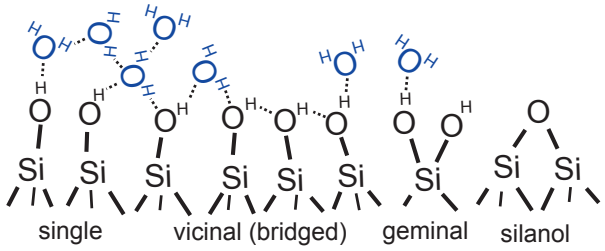

Fig. 4: Types of silanol groups and siloxane bridges on the surface of amorphous silica and adsorbed water molecules [31,32]. Solid lines represent covalent bonds and dashed lines the hydrogen bonds.

Molecular dynamics computations have been performed for the bonding of surfaces of silicon oxide covered by a water layer [36–39]. The adhesion surface energy between two silica surfaces is simulated as a function of the amount of water molecules present at the interface, and as a function of the separation distance. Fig. 5, generated by molecular dynamics computations, gives an idea of the interface structure at the atomic level. For more than 2 mono-layers of water, twice the surface tension of water is retrieved (i.e. $\sim 144\,mJ/m^2$ at $25\,°C$). A maximum value of about $180\,mJ/m^2$ is obtained for one mono-layer of water per wafer surfaces [38]. This value, higher than the surface tension of water, is explained by an ordering of the water molecules, due to the oxide surface. Also, an ice-like structure of the first monolayer of water adsorbed on the oxide surface has been suggested in other studies [40–42].

Work of adhesion. Although the concept of work of adhesion is used in many fields [30, p. 312], we limit, here, the definition of the work of adhesion to the direct wafer bonding application. The work of adhesion is the energy per unit area which drives the bonding process. In other words, it is the energy gain by the creation of an interface, at the moment the interface is being closed.

It is usually considered that direct wafer bonding at room temperature is reversible. However, interface aging (discussed in the following Section 6) leads to the increase of the interface energy subsequent to its closure. D. S. Grierson et al. have shown that, even for short time elapsed after the contact, an hysteresis effect is observed [43]. This effect

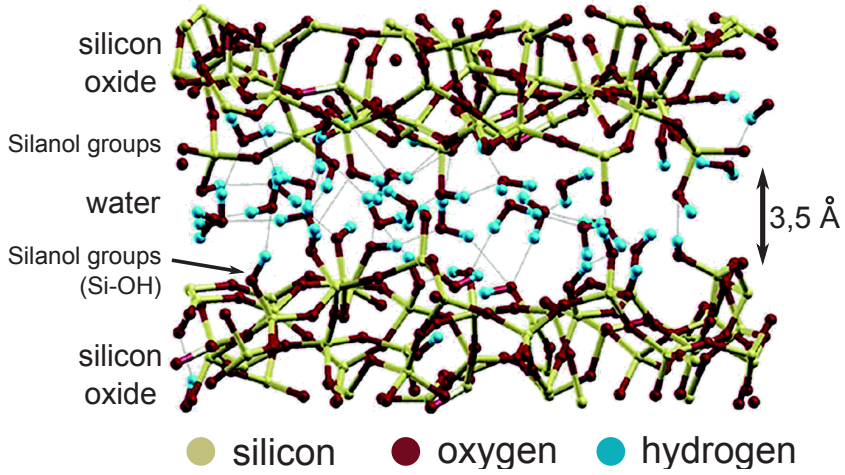

Fig. 5: Schematic representation of the bonding interface obtained from a molecular dynamic simulation (from S. Leroch et al. [39]). Grey lines account for hydrogen bonds.

is quite important for this study, since a predictive modeling of the propagation of the bonding front requires a value of the energy gain by the interface closure. Moreover, most values discussed in the bonding literature are obtained by opening the interface. Hence, we make the strong distinction between "work of adhesion", noted W, which represents the energy involved in the formation of the interface, and the "bonding energy", noted E, which represents the value obtained with a common blade insertion measurement, as "work of decohesion".

It is interesting to note that Lord Rayleight in 1936 obtained a value equal to $142\,mJ/m^2$ when stripping two glass plate, and $74\,mJ/m^2$ when the two glass plates are contacted [6]. K. T. Turner et al. used a dedicated set-up in order to measure the work of adhesion [44]. First, one wafer is bowed by deposited a stressed film. Hence, a minimum surface energy is needed to propagate the bonding front. Secondly, the energy density available to propagate the bonding front is reduced along the bonding front path, by etching a pattern on the wafer surface. Therefore, the bonding front propagation stops at a fixed radius, which is dependent of the work of adhesion. A mechanical model is then used to extract the work of adhesion value.

And, as mentioned, D. S. Grierson et al. [43] measured the work of adhesion and the work of separation, as a function of the relative humidity, is the case of silicon hydrophilic direct bonding. The measurement method consists of an actuated micro-sized silicon beam brought in adhesive contact with a silicon substrate.

To conclude, the expected parameters that have an influence on the work of adhesion in direct wafer bonding are, the density of hydroxyl groups at the surface, the type and chemical structure of hydroxyl groups, the amount of water and the water layer structure (i.e. the ambient humidity), and finally the surface micro-roughness.

Related studies. Adhesion, actually, constitutes the main failure mechanisms in micro-electromechanical systems (MEMS). Many studies address the stiction issue [45–49]. Often, the free-standing structures are pulled into contact with the substrate by capillary forces, during the drying process.

Adhesion between very rough surfaces can occur through capillary bridges (root mean square roughness value ∼10 Å) [50–52]. In this case, some parts of the interface are filled by water and meniscus are formed at the water/air interfaces. Wafer bonding using capillary force has been previously reported [53]. Here, the interface is first entirely filled by liquid methanol. As the methanol evaporates, the two surfaces attract one another by the Laplace pressure. In the hydrophilic direct bonding case, it is assumed that the quantity of water is not sufficient to form a meniscus at the bonding front, and the interface roughness is too small to form capillary bridges between the two surfaces.

And, finally, surface adhesion effect is also experienced when using an atomic force microscope (AFM). Therefore, AFM is often used to study interaction forces between a sphere and a surface as for instance when looking at the friction at the nanoscale [40, 42, 54, 55]. Despite the wide literature on the subject, it is quite difficult to adapt to the direct bonding field, mainly because the geometry is not the same (for instance, force value is usually considered instead of an energy per unit area).

3 | Bonding front propagation

Direct wafer bonding leads to an unique adhesion front propagation mechanism. When placing the two wafers in front of each other, a thin air layer (less than 30 μm in thickness) remains trapped between the two wafers, preventing immediate spontaneous adhesion. In practice, a light pressure has to be applied locally on the top wafer in order to create the first contact point. Afterwards, adhesion forces pull the wafers surfaces into contact. The bonded area expands by it-self by expelling the remaining air across the entire wafer area. The propagation of the bonding front, also called “bonding wave”, can be observed and quantitatively analyzed [1, p. 33]. Fig. 6 gives a typical example of a bonding front propagation observation using infrared light transmission through the silicon wafers.

Many experimental studies have measured the bonding propagation velocity as a function of various parameters: wafer thickness and wafer diameter [56], bonding chamber pressure and gas viscosity [57], bond strength, storage time after a HF treatment and pH of the drying solution [58], and, finally, as a function of the wafer temperature during the bonding [59]. Bonding speed of $1 - 2\, cm/s$ are typically observed for hydrophilic bonding.

F. Rieutord et al. has proposed a theoretical analysis of the bonding system [60]. The wafer is considered as a thin elastic plate. The air flow between the two wafers is modeled using a Poiseuille flow assumption. Then, a relationship between the bonding velocity and the work of adhesion is obtained, in the permanent regime, as a function of the fluid viscosity, of the wafer flexural rigidity and of a cut-off distance taken equal to the molecular mean free path in the gas.

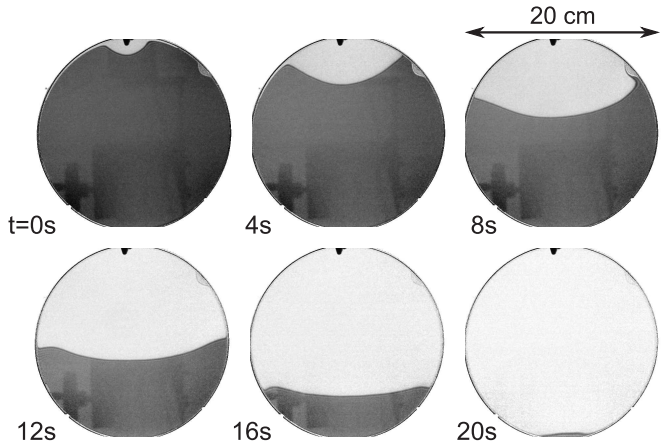

Fig. 6: Infrared light observation of a typical bond front propagation between two silicon wafers (200 mm in diameter). About 20 seconds is needed for the bonding to spread across the entire wafer area. The darker area is non bonded.

Viscous dissipation inside a thick liquid layer at the interface has been theoretically studied using a cohesive zone model approach by D. V. Kubair et al. (the adhesion force is expressed using a force-distance function) [61–63]. The viscous dissipation is assumed to come from a liquid meniscus at the bonding front. This model is relevant in the case of very thick adsorbed liquid layer on wafer surfaces (for example, in the specific use of liquid adhesive inter-layer).

4 | Final curvature of the bonded wafers

Wafers are thin disks and they are usually flat. But, sometimes, wafers can be slightly curved at the macroscopic scale. This is the case, for example, when a material with a different thermal expansion coefficient is deposited at high temperature on one of the wafer surface. Therefore, studying how the bonding process is affected by the wafer curvature is important. This is even more important, since it is known that the bonding process can induce itself a curvature in the wafers stack.

A theoretical study has been first proposed by K. T. Turner et al. [64]. Two cases are distinguished: the free configuration and the clamped configuration. It is assumed that, the free configuration occurs when adhesion forces between the surfaces are strong enough to pull wafer surfaces in contact. The clamped configuration occurs when an external load is applied on the entire wafer area in order to bring the two surfaces in contact (for example thermo-compression or eutectic bonding).

The expression of the final curvature k_f is obtained, in both cases, as a function of the initial curvature of the wafers k_1 and k_2, the material properties (Young's modulus, Poisson ratio and wafer thicknesses) and, for the clamped configuration, as a function of the bonding curvature k_b, which is given by the chucking system. Both cases are illustrated in Fig. 7. A way to understand these two situations, it to consider that the bonding interface

is able to slide in the free bonding configuration, while in the clamped configuration no sliding occurs at the bonding interface.

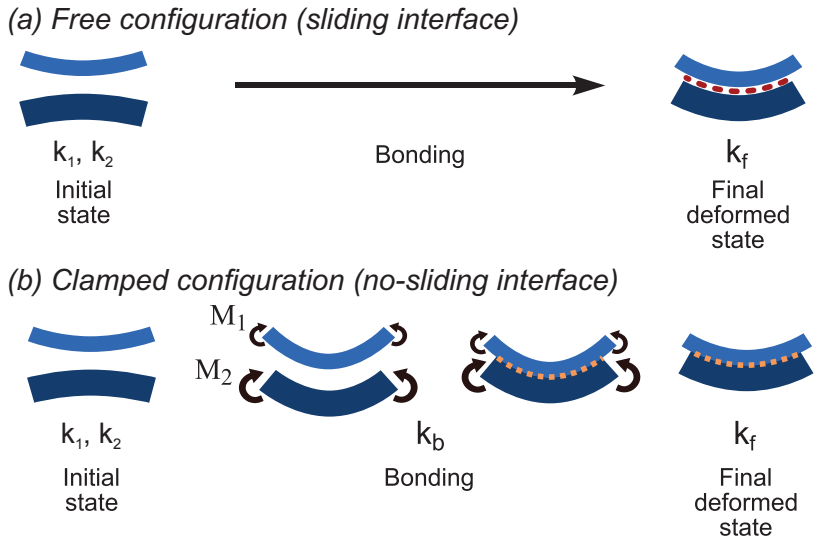

Fig. 7: Mechanism used to explain how a bowed stack can be obtain by joining two wafers. Inspired from [64].

Some applications of mechanical deformation of the bonding system have been studied. It is known that the electrical properties of a transistor can be improved when a mechanical strain is applied on the channel of the transistor. Hence, it can be interesting to create a strained layer by applying, on purpose, a mechanical deformation on the two wafers during the bonding [65–68] and [1, page 198]. By thinning one side of the bonded wafer, the deformation strain is essentially transferred to the thinned wafer.

However, the deformation induced by the wafer bonding process may also have detrimental consequences on the final system. For instance, in the case of the transfer of a circuit layer, the bonding deformation can lead to a pattern distortion, preventing subsequent lithography (related to the overlay issue) or preventing an accurate device to device alignment [69–71]. It is worth mentioning that K. T. Turner et al. have studied the related issue, which consists in deriving the relationship between the wafer curvature and the pattern distortion generated when the wafer is flattened on a chucking system (in a lithography equipment) [72, 73].

5 | Elastic deformation and adhesion

The interplay of adhesion and elastic deformation of solids has been studied for a long time. The wafer surfaces are not perfectly flat and the adhesion forces can deform elastically the material. Depending on the material elastic properties, and the geometry of the material, a good adhesion can be achieved or not. Advanced models are, therefore, needed to evaluate the influence of the geometrical aspects on the adhesion.

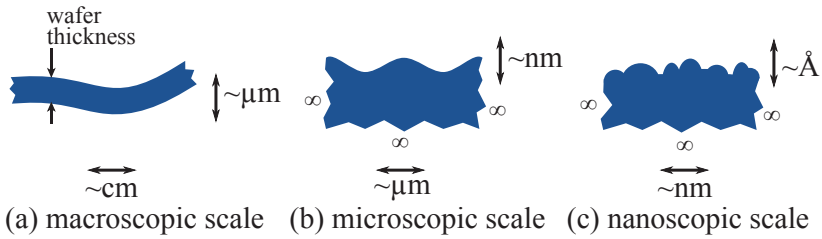

Fig. 8: Three scales of flatness variation considered in direct bonding. (a) Wafer curvature. (b) Wafer surface topology. (c) Surface roughness.

The wafer geometry is commonly divided in three scales. Boundaries of the scale division can be defined, for instance, as a function of the origin of the no-flatness variation or its influence on the bonding [74, p.28]. Actually, each scale range can be seen as the validity domain of the assumptions used in each corresponding model.

When the considered in-plane dimension is much larger than the wafer thickness, the thin plate model can be used (see Fig. 8a). Hence, only the wafer curvature is used to describe the wafer geometry. At this scale, the thin plate model is applied [74, 75]. It is interesting to note that C. Majidi et al. considered both bending and membrane strains [76].

At a smaller scale, only the material close to the surface is deformed by adhesion forces (see Fig. 8b). Therefore, the wafer is described as a semi-infinite material. H. H. Yu and Z. Suo have derived a model using a sinusoidal wave function to describe the surface [77]. K. T. Turner has performed an experimental validation of the model, and further development using the power spectral density (PSD) function [74, chapter 7]. A fractal approach has been recently developed by B.N.J. Persson [78, 79].

At a nanoscopic scale, the surface roughness is considered (see Fig. 8c). Here, the statistical properties of the surface need to be considered. Starting from the Hertz contact theory, several models have been developed to study adhesion of an single elastic sphere on a plane (Derjaguin, Muller and Toporov model and Johnson, Kendall and Roberts model) [80–83]. Afterward, many surface adhesion models have been developed considering that surface roughness can be described as a set of spheres with the same statistical properties [84–88].

Nevertheless, considering the elastic deformation at the nanoscopic scale, may not be appropriate. As previously mentioned, in the case of hydrophilic bonding, the thickness of the water layer is on the same order of magnitude as the topological variation (one water molecule diameter is about 3 Å). N. Miki et al. use the bearing ratio, which describes the area of surface lying above a given depth, in order to derive the effective contact area as a function of the roughness without considering any elastic deformation [89].

Wafers can also be deformed because a particle is present at the interface. The bubble size has been obtained as a function of the adhesion energy and wafer properties [1, chapter 3].

It is interesting to mention that coupling adhesion and elasticity may lead to an

hysteresis effect [90], and also to the generation of some complex patterns when working with soft materials [91].

6 | Aging of the bonded interface

Once the interface is closed, it starts to evolve toward a more energetically favorable state. The evolution of the bonding interface is thermally activated, meaning that it depends on temperature and time. The major part of the literature deals with the temperature dependence, but some earlier reports have discussed the influence of time, even at room temperature (so called aging effect) [58]. In the practice, thermal treatments at elevated temperatures (up to $1200\,^{\circ}C$) are performed to reinforce the bonding interface and the process time is optimized.

Many experimental methods have been used in order to study the bonding interface evolution in time and temperature. A blade insertion test is commonly used to measure the bonding interface energy [92, 93]. Infrared absorption spectroscopy (FTIR-MIR) allows probing the chemical species at the interface [94–97]. X-ray reflectivity measurement has been used to measure the electronic density profile through the bonded interface as a function of the temperature [98–100]. Both infrared light transmission, and acoustic microscopy, are used to detect the interface bubble formation [1, 101–103]. Array of cavities has also been proposed to measure the interface pressure evolution as a function of temperature [104]. Transmission electron microscopy (TEM) has been used to observe the nanometric evolution of the interface [100, 105], see for instance Fig. 9.

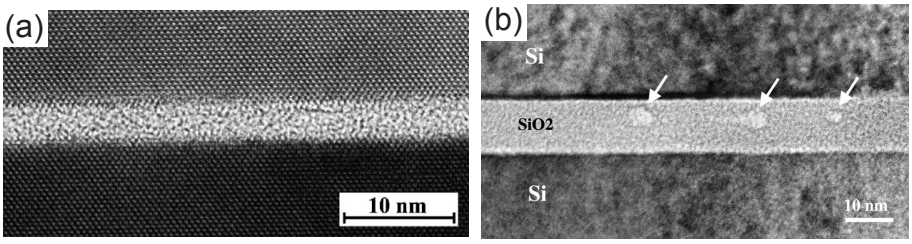

Fig. 9: (a) High resolution transmission electron microscopy (HRTEM) cross-section image of the bonding interface after annealing at $950\,^{\circ}C$ (native oxide, hydrophilic bonding). The crystalline structure of silicon is visible (from [105]). (b) Another example of a TEM cross-section image showing some interface voids in a oxide/oxide hydrophilic bonding (from [100]).

Based on the experimental observations, several theoretical descriptions of the bonding interface evolution have been proposed. The first model was proposed by R. Stengl et al. [59].

The energy rise of the bonded interface is explained by many steps. First, a few water mono-layers are present at the interface. Subsequently, the water molecules adopt a more stable tetramer cluster structure. At high temperature, water diffuses away from the interface, leading to the formation of bonds directly between the hydroxyl groups of each surfaces. Afterward, silanol bonds (Si–O–Si) form by polymerization of the hydroxyl groups,

leading to the production of water molecule. In addition, the water diffuses through the silicon oxide and oxidizes the silicon, leading to hydrogen formation. Part of the hydrogen remains in the silicon oxide, while the hydrogen excess leads to the formation of bubbles along the bonding interface.

Earlier models have considered the interface thickness as homogeneous, while subsequent studies have suggested an heterogeneous description of the bonding interface, due to the surface roughness [99, 100].

Molecular dynamics simulations of the silicon-silicon bonding (UHV and hydrogen passivated) and silicon-oxide/silicon-oxide bonding have been performed, when the interface is free of water [106–108] and also when water is present at the interface [36–38].

Various surface treatments, prior to bonding contact, are suggested in the literature to increase the bonding energy. They are typically considered as "surface activation" [1, p. 57]. In particular, plasma activation prior to bonding is known to increase the interface energy obtained at a lower annealing temperature [109–111]. Despite the large number of experimentals studies, no clear understanding of the physical phenomena related to the mechanisms driven by the plasma is available. Modification of the oxide mechanical properties and water diffusion ability have been suggested. A model has been recently proposed by Plach et al. [112]. The plasma is assumed to increase the amount of water stored in the silicon oxide prior to bonding, leading to additional oxide growth and then to a better interface closure due to the higher oxide density.

Stress corrosion effect. The bonding energy evolution is usually measured by inserting a blade between the two wafers, and by measuring the corresponding crack length [92, 93]. Nevertheless, it has been proved that the atmosphere has an effect on the measurement [12, 113–117]. The covalent Si–O–Si siloxane bonds can be broken by water molecules when under tension, the so called stress corrosion mechanism. Water molecules come from the bonding interface itself and from the atmospheric humidity. Two solutions have been proposed to prevent the atmosphere influence during the blade insertion measurement. The first solution is to use a rapid and constant blade insertion velocity, in such a way that the water atmosphere have no time to reach and react with the bonds at the crack front [115, 116]. The second method is to perform the measurement in an anhydrous atmosphere [117]. A direct comparison of the bonding energy evolution with temperature in case of anhydrous vs. standard humidity has been obtained.

List of the phenomena involved in direct hydrophilic wafer bonding. In order to summarize, a comprehensive list of the phenomena that occur or affect the bonding interface during hydrophilic silicon bonding is given:

- a thin layer of air remain trapped in-between the two wafers.
- adhesion through hydrogen bonding of water molecules adsorbed on the wafer surfaces.
- bonding front propagation, involving the elastic deformation of the wafers.
- the final wafer curvature is influenced by bonding conditions.
- water molecule re-organization in more stable structure, at the interface.
- asperity contact (roughness effect of the surfaces).
- elastic deformation of the material in order to close the interface.
- covalent bond formation following the reaction (which is reversible) : $Si{-}OH \ + \ OH{-}Si \ \rightleftharpoons Si{-}O{-}Si \ + \ H_2O$
- water diffusion, both along the interface and through the silicon oxide.
- silicon oxidation by the water, which products hydrogen : $Si + 2\,H_2O \rightarrow SiO_2 + 2\,H_2$.
- hydrogen diffusion, along the interface, through the silicon oxide, and through the silicon at high temperature.
- formation of water bubble.
- formation of gas bubble (H_2).
- water or hydrogen dissolution inside the oxide.
- silicon oxide properties modification due to the internal water.
- plastic deformation of the oxide (creep), at high temperature.

In the chapter, a global picture of the physics involved in the direct wafer bonding process has been settled, in particular for the hydrophilic direct bonding. The followings thesis chapters focus on the dynamics of the wafer bonding process, i.e. the phenomenon involved during the contacting step of the two wafers.

Chapter II
Bonding Front Propagation

Abstract

During direct bonding, a thin gas film is trapped in-between the two wafers, leading to a coupled fluid/structure dynamic system. A model of bonding dynamics is formulated using the thin plate theory for the wafer, Reynolds equation for the air film, and a specific boundary condition at the bonding front taking into account the work of adhesion. The transient equation is solved numerically in a one dimensional cylindrical case. The entire process, including initiation and propagation of the front, is simulated. The model is supported by experimental data from an original setup involving non-contact optical sensors to measure the vertical movement of the wafer during the bonding sequence. In addition, influence of the work of adhesion, initiation force, wafer curvature, and gas pressure is studied. The model is also extended to the two-wafers case.

Contents

1 | Introduction

1.1 | Propagation phenomena

This chapter focuses on the bonding front propagation phenomena. When the two wafers are brought into contact, an air cushion is trapped between them, preventing the adhesion (see Fig. 1). Because the air layer becomes very thin (less than $\sim 30\mu m$), the gas takes a very long time to escape. The application of an external force is needed to bring the surfaces in contact. Typically, the external force is applied on a single point on surface of the top wafer. Then, adhesion forces allow the spreading of the bonding over the entire wafer surface.

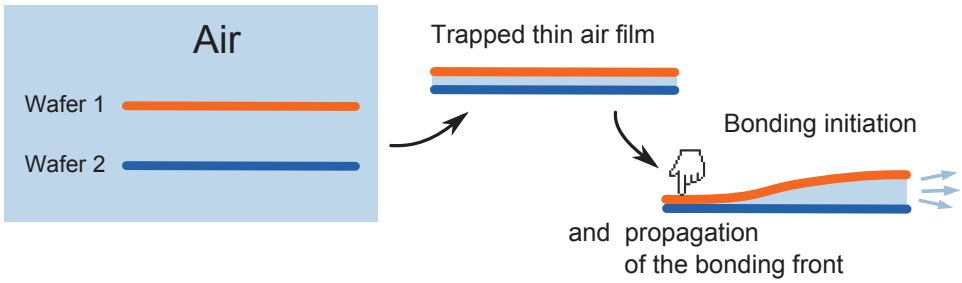

Fig. 1: Schematic view of the air/wafer interaction which lead to the front propagation phenomena.

The present chapter has the following structure: First, a simple analytical model, concerning the lubricated fall of a rigid disk, is derived in order to emphasize the importance of the trapped thin air film (Subsection 1.2). This simple theoretical work deals with the first step of the bonding process only. The entire bonding sequence is described in the following subsection (Subsection 1.3). Some examples of real bonding configuration (i.e. how the wafers are hold) are discussed in Subsection 1.4.

After these preliminary considerations, a theoretical model, coupling the mechanics of the wafer and of the fluid film flow, is derived. Both the numerical resolution and the dedicated experimental measurements are presented in Section 2. A discussion is undertaken about the results and the model hypotheses, in Section 3. Following the discussion part, some examples of model predictions are presented and discussed in Section 4. In Section 5, the model is extended to a more complex bonding configuration, where both wafers are free to move. This extension has a practical interest for the study presented Chapter III. In Section 6, results about the infrared light observation of the bonding front propagation are presented. And finally, in Section 7, possible future works are listed and discussed.

1.2 | The lubricated fall of a rigid disk

The wafer is considered, here, made of a flat and rigid disk of radius R, thickness e, and density ρ, see Fig. 2.

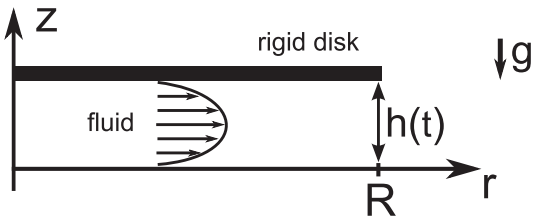

Fig. 2: Schematic description of a simple situation used to emphasize the importance of viscous effect in the thin fluid film. R is the disk radius, g is the gravity, $h(t)$ is the gap height between the disk and the floor.

The dynamics of the system is supposed to be governed by the viscosity of the fluid only (noted μ). This is not a free fall situation where only gravity and inertia act on the wafer. This implies, in practice, that the start of the fall has to be sufficiently close to the substrate (thin air layer) to prevent wafer accumulating more kinetic energy than the air layer can absorb. The motion of the wafer can be described by its vertical position $h(t)$ and its vertical velocity $\dot{h}(t)$ only. Because the thickness of the film fluid is small compared to the lateral dimensions of the system, the fluid velocity vector is assumed to be oriented along the disk plane (horizontal). This assumption leads to a Poiseuille flow, where the velocity profile along the thickness is parabolic. The boundary conditions for the fluid are that the velocity is zero at the interface. The fluid is considered also as incompressible since the expected pressure variation remains low (only the weight of the plate acts on the fluid). Then, the fluid velocity field $\mathbf{v}$ can be entirely written as a function of the plate vertical velocity, by using the conservation law :

$$\mathbf{v}\,(r,\,z) = 3r\,\frac{\dot{h}}{h^3}\,z\,(z-h)\,\mathbf{u_r} \tag{1}$$

where $\mathbf{u_r}$ is the unit vector is the radial direction.

The Navier-Stoke equation, particularized to the condition that only the viscous effects are important, $\mathbf{grad}P = -\mu\Delta\mathbf{v}$, leads to the following pressure equation and corresponding solution considering the boundary condition $P(R) = 0$:

$$\frac{dP}{dr} = 6\mu\frac{\dot{h}}{h^3}r\;; \quad P(r) = -3\mu\frac{\dot{h}}{h^3}\left(R^2 - r^2\right) \tag{2}$$

Finally, mechanical equilibrium between the wafer weight and the fluid pressure leads to writes:

$$\frac{\dot{h}}{h^3} = -\frac{2}{3}\frac{\rho g e}{\mu R^2}$$

This differential equation has an analytical solution, considering the initial height of the wafer $h(0) = h_0$:

$$h(t) = \left(\frac{1}{h_0^2} + \frac{4}{3}\frac{\rho g e}{\mu R^2}t\right)^{-\frac{1}{2}}\;. \tag{3}$$

Fig. 3 shows the variation of the wafer position $h(t)$ as a function of time, for common

parameter values (disk radius is equal to $R = 10\,cm$).

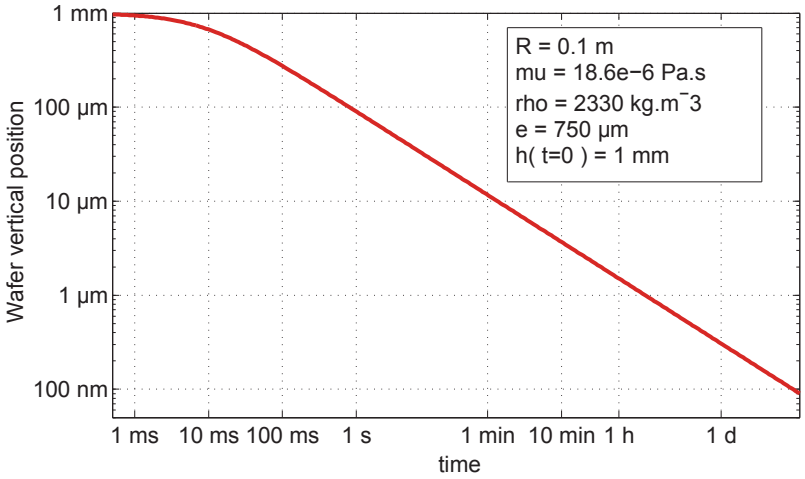

Fig. 3: Calculated variation of the vertical position $h(t)$ of the wafer, considered as a rigid disk, as a function of time for the parameters given in the figure inlet (eq. 3).

This result shows that the air layer trapped between the two plates needs more and more time to escape, as the run off section thickness decreases. More than one day is needed for the air layer to be thinner than $100\,nm$, which is almost the value of the molecular mean free path in air at ambient pressure.

This floating behavior is not experienced on everyday life situations (with a paper sheet for example). The main reason is that typical object surfaces are too rough or present some irregularities such as small particles. Therefore, real contact between surfaces occurs much sooner than with silicon wafers. In a clean room environment, the phenomenon exists and has a real importance during the direct wafer bonding process.

For instance, manual wafer bonding is usually performed on an inclined support (see Fig. 4) in such a way the wafers slide down until end-stops, facilitating the alignment.

In addition, an external force has to be applied locally on the wafers, to bring them into contact in a reasonable time and initiate the bonding. This step is called “initiation of the bonding”. The next paragraph describes the entire bonding sequence.

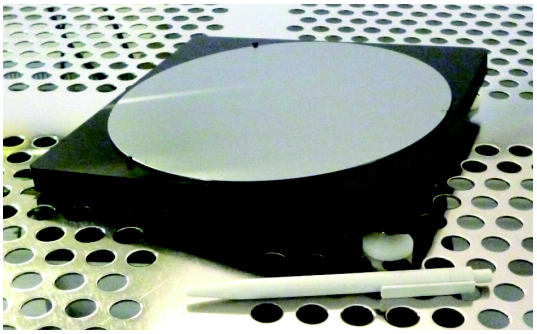

Fig. 4: Image of 200 mm diameter bonded wafers, on the support used for manual bonding. The support is inclined in such way that alignment of two wafers are facilitated.

1.3 | The bonding sequence

The actual bonding process can be described by four different steps, illustrated in Fig. 5:

- "Before initiation" step: The top wafer is released and slowly falls down.
- "Initiation" step: An external force is applied at one point of the top wafer in order to initiate the bonding.
- "Contact" step: The contact occurs between the wafers and the external force is held.
- "Propagation" step: The bonding front propagates across the entire wafer surface. During propagation, the wafer surface is divided into a bonded area and a non-bonded area.

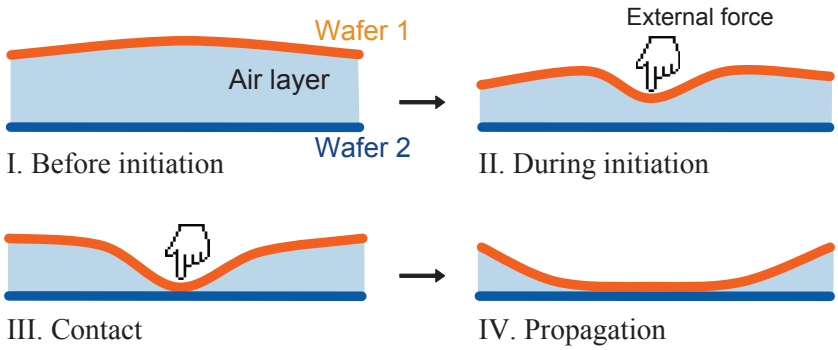

Fig. 5: Sequence of direct wafer bonding I. before initiation only gravity and fluid pressure act on the top wafer; II. an external initiation force is locally applied; III. contact occurs between the wafers at the point of initiation while holding the applied force; IV. adhesion forces lead to the expansion of the bonded area.

For simplicity, the bottom wafer is assumed, in Fig. 5, to be clamped to a rigid and flat support. Consequently, only the movement of the top wafer is considered. In the practice, many different configurations are encountered. Example of the common other configurations are presented in the next paragraph.

1.4 | Bonding configurations

Bonding configuration denotes the way wafers are hold during the bonding process. In the practice, many different configurations are possible. Some of them are illustrated Fig. 6.

The most simple situation is when the bottom wafer is clamped to a rigid support (a), by using a vacuum chuck for example. Then, only the movement of the top wafer has to be considered. For this reason, the following modeling work addresses this specific configuration. In the practice, the bottom wafer is usually not clamped to the support. Then, a second fluid film (air) can be present between the support and the bottom wafer (b). In addition, rigid contact between the bottom wafer and the support can append. In this case, the support points location of the wafers stack are unknown and a non-linear contact problem has to be solved. The effect of the second fluid film can be canceled, if, for example, the support is grooved (c). Nevertheless, in this configuration the non-linear contact problem is still present. In order to overcome this modeling issue, the support has to be restricted to three known contact points only (d). This configuration, as it

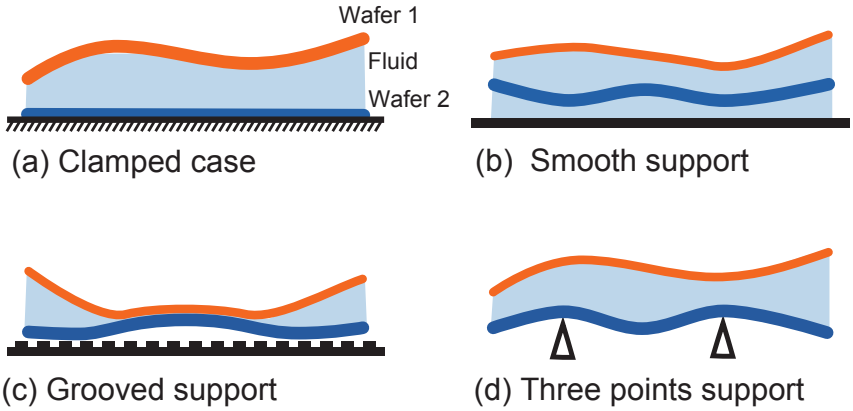

Fig. 6: Common bonding configurations encountered in practice.

will be seen, has many practical advantages. A model extension, to describe both wafers movement, is proposed in Section 5 of this chapter. Moreover, the experiments related to the study of the post bonding wafers curvature use this configuration (Chapter III). Now, for simplicity the equations are written for the clamped case (a).

2 | The bonding propagation model

A model for this problem has been proposed by Rieutord et al. [60], providing a relationship between the work of adhesion and the bonding velocity as a function of the system properties (air viscosity, Young's modulus and thickness of the wafer). In this model, the wafer is described using the plate theory, the air layer by a Poisseuille flow, and the adhesion at the bonding interface through an energy balance. A contact line singularity problem arises, overcome by introducing the air molecular mean free path as a cut-off length. An analytical solution has finally been proposed for the one dimensional permanent regime.

We propose a transient analysis of a similar theoretical system. The entire wafer bonding sequence, including the initiation and propagation steps, is studied. Moreover, a novel experimental method is set-up for the measurement of the out-of-plane movement of the wafer. A comprehensive description of the vertical movement of the wafers before and during the bonding is derived and discussed. This model has been published in Applied Physics Letters as Navarro et al. [118].

The system of a deformable plate coupled with a thin fluid layer can be found in various other situations, such as foil bearing (magnetic tape recording) [119] or a falling sheet of paper [120, 121].

2.1 | Theoretical part

Fig. 7 introduces the notations used herein. The variable $h(x, y, t)$ stands for both the local thickness of the fluid film and the deflection of the top wafer.

The main assumption, regarding the geometry of the system, is that the thickness of the wafer is much smaller than the lateral dimension. This means that the Kirchhoff-Love

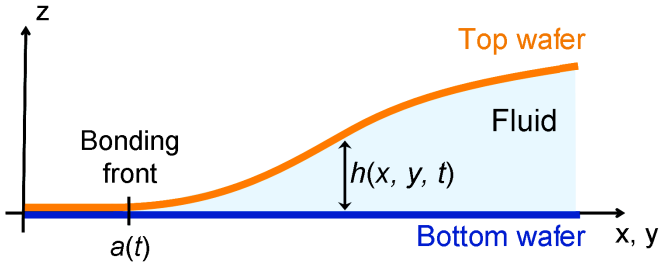

Fig. 7: Schematic description of the direct wafer bonding model. The bottom wafer is considered clamped to a rigid and flat support.

plate theory [122] can be used to describe the mechanics of the wafer as

$$\Delta\Delta h\,(x,\,y) = \frac{F_{\text{surf}}(x,\,y)}{D}\,, \tag{4}$$

where Δ is the Laplacian operator, D is the flexural rigidity, and F_{surf} is the force acting on the surface of the wafer, resulting from the relative gas pressure P and gravity. The inertia of the wafers is considered negligible when compared to the gas pressure.

The thickness of the film of fluid is very small compared to the horizontal dimension. Inertia forces in the fluid can be neglected and the gas is assumed to be incompressible. These approximations, which are discussed later in the chapter (see section 3), lead to the incompressible Reynolds equation [123]:

$$12\mu\frac{\partial h}{\partial t} = div\big(\,h^3\mathbf{grad}P\,\big)\,. \tag{5}$$

A singularity appears when contact occurs at the bonding front. Indeed, Reynolds equation, which derives from the continuum Navier-Stokes equation, is not a proper description of the fluid behavior when the thickness becomes very small. Similarly the kinematics of the interior surface of the wafer, at this scale, is not adequately captured by the plate theory. An efficient solution to model the macroscopic bonding front propagation is to add a cut-off length to the thickness of the fluid through an arbitrary parameter h_c. The physical meaning of this cut-off length is a combination of mechanics and fluid interaction at the nanometer scale. This point is discussed in detail in the Subsection 3.1. h_c must be considered, here, as a phenomenological parameter of the model.

By combining eq. (4) and eq. (5) the two dimensional evolution of the gap height between the wafers writes:

$$\frac{\partial h}{\partial t} = \frac{D}{12\mu}div\Big(\,(h+h_c)^3\,\mathbf{grad}\,(\Delta\Delta h)\,\Big). \tag{6}$$

This is a sixth order non linear partial differential equation. Six boundary conditions are thus required, summarized in Fig. 8. The boundary condition on the edge of the wafer remains the same for the four steps of the bonding. However, the conditions on the interior

boundary depend on the bonding step. Before initiation, the boundary conditions consist only of imposing symmetry. A force is applied to initiate the bonding. During the contact period, the edge of the wafer is clamped and the fluid flow is set to zero. During propagation of the bonding front, the boundary is moving. Therefore, an additional boundary condition must be used, taking into account the work of adhesion W.

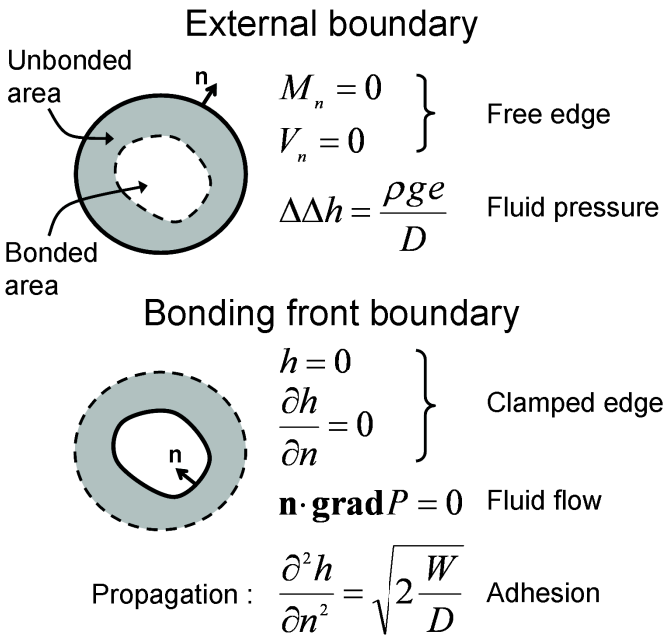

Fig. 8: Boundary conditions used for solving eq. (6); M_n is the momentum normal to the boundary; V_n is the shear force on the boundary; ρ is the density of wafer, e is the wafer thickness; g is the gravity acceleration. The boundary condition on the external edge of the wafer remains the same for the four bonding steps. The conditions on the interior boundary for the contact step are the built in edge and the zero fluid flow. For the propagation step, a last condition is added.

A relationship between the work of adhesion and the curvature of the plate at the bonding front is obtained from an energy balance [124–126], as

$$W = \frac{D}{2}\left(\frac{d^2h}{dx^2}\right)^2. \tag{7}$$

Thanks to this equation, the work of adhesion can be an input value of the model, while the bonding velocity is an output value.

Steady state regime Considering the steady state regime case, i.e. when $\partial h/\partial t = -v\,\partial h/\partial x$, where v is the bonding speed, the following equation is obtained:

$$h^{(5)} = -\frac{12\mu\, v}{D}\frac{h}{(h+h_c)^3} \tag{8}$$

It should be noted that the axisymetric hypothesis can not be used in the permanent regime. By carrying out a dimensional analysis including eq. (7), the following relation is obtained:

$$v \propto \frac{h_0^{\frac{1}{2}} W^{\frac{5}{4}}}{\mu D^{\frac{1}{4}}} \tag{9}$$

where h_0 is a typical height of the system, such as h_c. A similar expression has been reported by Rieutord et al. [60].

2.2 | Numerical resolution details

Numerical solutions of eq. (6) are computed for one dimensional cylindrical symmetry (eq. 10):

$$\frac{\partial h}{\partial t} = \frac{D}{12\mu}\frac{1}{r}\frac{\partial}{\partial r}\left\{ r\,(h+h_c)^3 \frac{\partial}{\partial r}\left[\frac{1}{r}\frac{\partial}{\partial r}\left(r\,\frac{\partial}{\partial r}\left\{\frac{1}{r}\frac{\partial}{\partial r}\left[r\,\frac{\partial h}{\partial r}\right]\right\}\right)\right] \right\} \quad . \tag{10}$$

The equation is discretized in time using a first order implicit scheme. The wafer height $h(r,t)$ and the bonding front position $a(t)$ are computed, for each time iteration, by solving the spatial equation using the Matlab® boundary value problem solver (*bvp4c*, finite difference code). The moving boundary problem is solved by reducing the time dependent resolution domain $[a(t),\, R]$ to $[0,\, 1]$ through a change of variable. Then the front position $a(t)$ becomes a parameter of the equation. A special option of the *bvp4c* solver is used in order to compute this parameter at every time step. For each time step, the previous solution is used as the starting point by the non-linear iterative solver.

Tests conditions are implemented in order to switch between the different bonding steps (see table 1). Due to of the axisymmetric singularity at $r = 0$, the solution domain is reduced to $[r_0,\, 1]$, with r_0 equal to 10^{-2}.

Because the solver *bvp4c* uses an automatic mesh optimization, an interpolation of the solution is needed at every time step. For the same reason, the initial selection of the spatial mesh is not critical. There are about 40 points used for the spatial mesh.

There are many time step adjustments during the computation. The time step is multiplied by a constant factor, which depends of the bonding step. The constant factors are adjusted manually by successive trials and error corrections.

Before initiation to initiation	$h(\,r=0\,) < h_{init}$
Initiation to contact	$h(\,r=0\,) < h_1$
Contact to propagation	$h^{(2)}(\,r=0\,) < h_{BC}^{(ii)}$

Tab. 1: Tests conditions used to switch between bonding periods. h_{init} is fixed according to the experimental result. h_1 is a fixed parameter used in order to prevent the collision between the two wafers (i.e. that height become negative). $h_{BC}^{(ii)}$ is the wafer curvature given by the propagation boundary condition (eq. 7).

2.3 | Experimental methods and results

2.3.1 Out-of-plane displacement sensors

The direct wafer bonding process is usually characterized using infrared light transmission through the wafers stack (silicon is transparent starting from $1.1\,\mu m$). This type of experiment gives information about the bonding velocity and about the front shape during the propagation step. Only an in-plane information is obtained. Therefore, a novel experimental method was needed to characterize the pre-contact step of the bonding step, as well as the out-of-plane wafer movement during the propagation period.

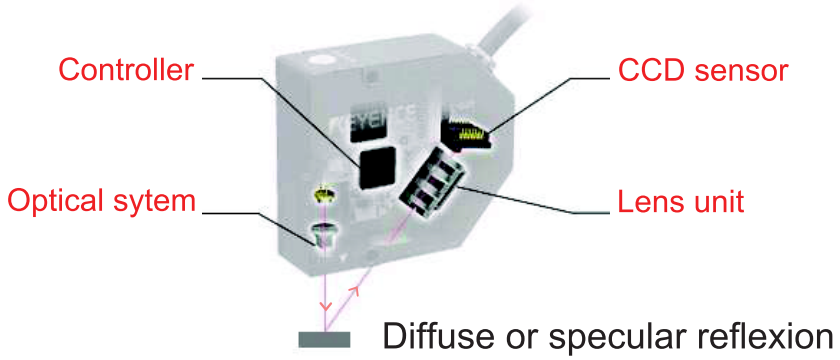

Fig. 9: Measurement principle using triangulation (from the Keyence catalog). The size of the sensor is about $6\times6\times3\,cm$ and the distance from the substrate to the sensor is about $2\,cm$.

The vertical displacement of the top wafer is measured at two different positions by LK-H022K contactless displacement sensors from Keyence®. The specular reflection of a laser beam on the moving surface is recorded using a CCD matrix which tracks the position of the reflected spot (see Fig. 9). The surface height is directly deduced. The resolution is about $0.5\,\mu m$ (minimum height variation detection) and the measurement range is equal to $6\,mm$.

2.3.2 Experimental method

The two sensors are fixed above the wafers at $4\,cm$ and $9\,cm$ from the center, as shown in Fig. 10. The setup is mounted on an anti-vibrating slab. The first wafer is put on the support. After a few minutes, the top wafer is softly placed above the first wafer. Bonding initiation is carried out by pushing down the center of the wafer with a stylus. The whole bonding support is slightly tilted downward, in such a way that two end-stop allow the alignment of the two wafers.

Standard $200\,mm$ bare silicon wafers, $750\,\mu m$ thick, are used for the experiments. Prior to bonding, conventional silicon wet cleaning is performed on the wafers using the SC1 and SC2 standard cleaning sequence [1].

As previously reported [43, 60], the work of adhesion can be different from the work of separation. A work of adhesion equal to $W = 112 \pm 30\,mJ/m^2$ is obtained by a method

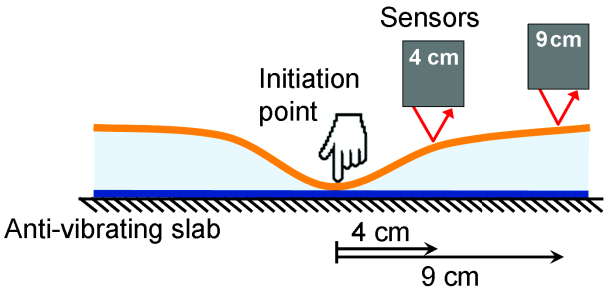

Fig. 10: Schematic of the experimental setup to measure out-of-plane bonding wafer displacement.

similar to the one suggested by Rieutord et al. [60]. The method consists of introducing a small object between the two wafers before the bonding occur. The bonding front is then stopped by the object and the mechanical equilibrium can be written similarly to the common blade insertion test [92]. The measurement protocol has been improved later, and the final accurate procedure is presented in the Chapter IV (see Section 3, p. 87). The measurement presented here corresponds to the first version of the measurement protocol, explaining the large error value.

2.3.3 Results

Fig. 11 shows the vertical displacement of the top wafer at the two sensor positions during the bonding. Acquisition starts a few seconds after the drop. Until time $t = 0$ the top wafer falls freely. At $t = 0$, an initiation force is manually applied on the wafer. Then, some vibration is observed on the signal. The outer part of the wafer moves up by about $10\,\mu m$ in height and oscillates. The fall of the inner part of the wafer accelerates. Then, the curve presents a shoulder. Finally, a constant descent rate is observed until complete bonding occurs. This final descent rate value is the same for both sensor positions.

The simulation is carried out with the following parameters: flexural stiffness $D = 5\,Pa.m^3$; air viscosity $\mu = 18.6.10^{-6}\,Pa.s$; silicon density $\rho = 2330\,kg.m^{-3}$; and work of adhesion $W = 112\,mJ.m^{-2}$.

The initiation step starts when the height of the wafer center reach the value $h_{init} = 24\,\mu m$, fixed according to the experimental curve. Both initiation forces (F_{init}) and cut-off length (h_c) values are adjusted to fit the experimental data. A value of $F_{init} = 5\,N$ is found, consistent with the force measured with an automatic bonding equipment. The cut-off length is $h_c = 35\,nm$, which is the expected scale for the phenomena involved at the solid-solid-fluid contact line. More detailed discussion about this point is undertake in the Subsection 3.1.

The curves predicted by the model at the location of the sensors are shown in Fig. 11 and compared to the experimental profiles. Fig. 12 shows wafer profiles computed at different times, in order to better understand the kinematics of the out-of-plane wafer movement.

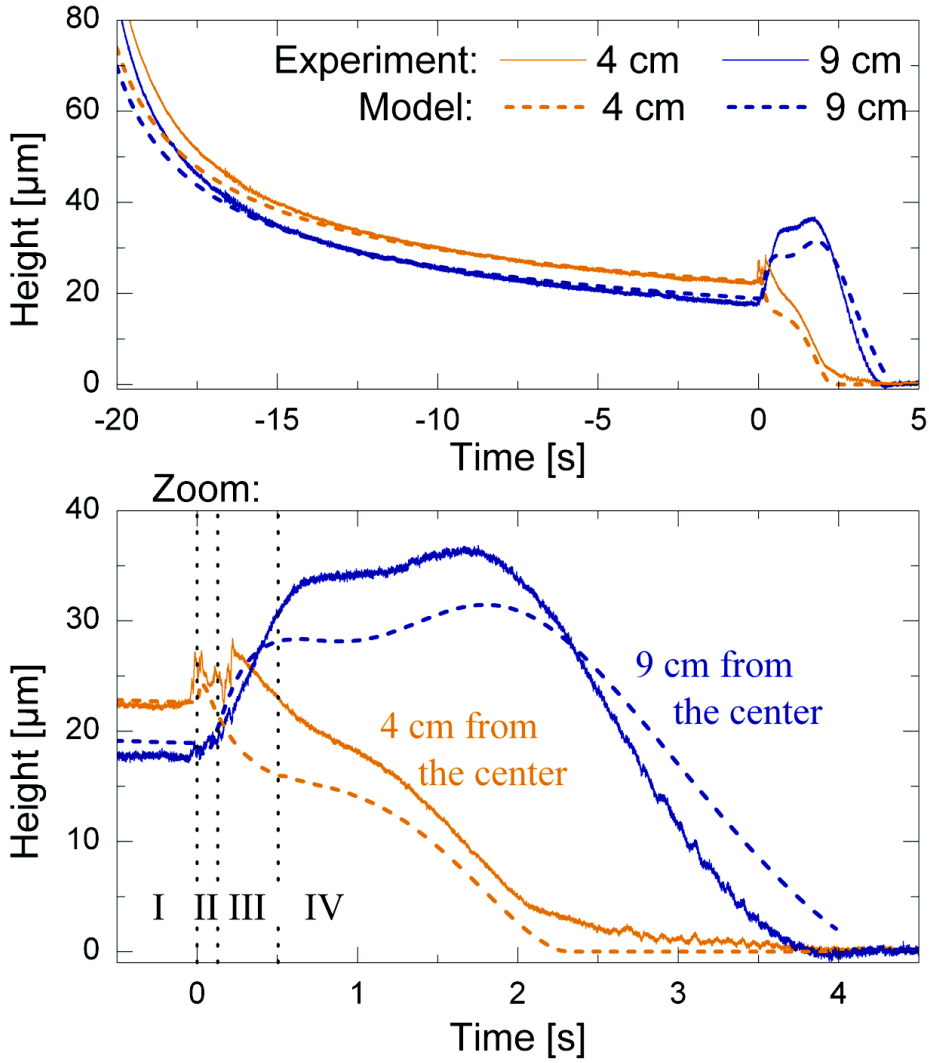

Fig. 11: Experimental (solid line) and simulated (dash line) out-of-plane wafer displacement taken at distances of $4\,cm$ and $9\,cm$ from the wafer center. I-Before initiation, II-Initiation, III-Contact, IV-Propagation. Time ($t = 0$) is fixed relative to the initiation.

Before initiation, because of the pressure gradient in the fluid, the upper wafer is curved downwards, leading to the offset between the two sensors (see Fig. 12). The decrease of the displacement rate can be explained by the lower air run-off section. Evolution of the wafer height during the "before initiation" step is well described by the formula derived in "The lubricated fall of a rigid disk" subsection (1.2). The assumption of negligible bending (i.e. considering a rigid disk) is valid since the gap between the wafers is much larger than the induced warp of the plate (here $\sim 5\,\mu m$).

The decreasing rate of downward displacement emphasizes the fact that the wafer can float on an air cushion a very long time after release and that an external initiation is necessary to bring suddenly surfaces into contact.

As a consequence of the localized application of an initiation force, the wafer becomes significantly curved. When contact occurs, the elastic energy stored inside the wafer is too

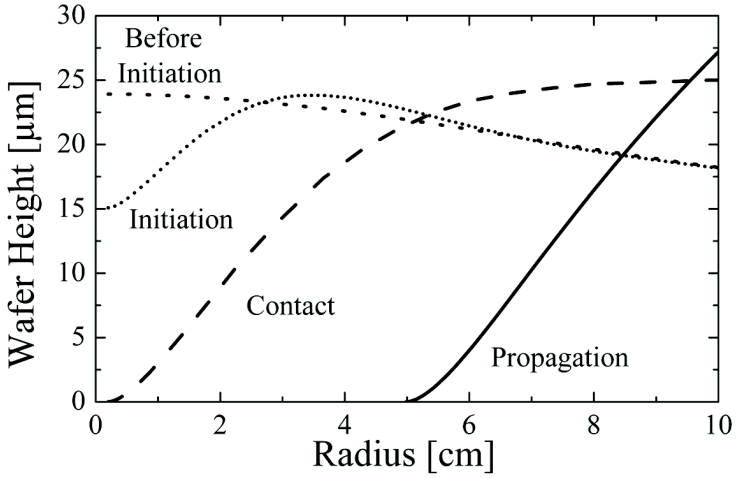

Fig. 12: Simulation results showing different profiles of the top wafer at different time step; each one corresponds to a different step of the bonding; time is relative to the start of initiation.

large to allow the bonded area to be maintained by the adhesion energy. Thus, contact is held until the adhesion boundary condition on the wafer curvature (eq. 7) is satisfied.

During the propagation step, the bonding velocity starts from zero and rapidly increases along the first $2\,cm$ from the center to an almost constant value, which is about $2.4\,cm/s$ for this bonding (see Fig. 13). This first acceleration is due to the axisymetric geometry, resulting in a non-uniform elastic energy release rate (see [75]). A second acceleration is expected to happen near the wafer edge, due to the facilitated evacuation of the air. Unfortunately, the non-linear solver is not able to capture the end of the propagation. According to computation results in the permanent regime, by varying the beam length, an acceleration is expected to occur in the last centimeter to the wafer edge.

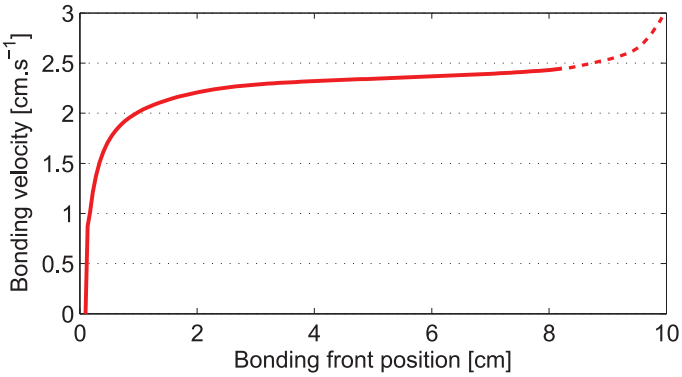

Fig. 13: Theoretical bonding front velocity as a function of the front position. The final shape of the curved (dashed line) is deduced from computation in the permanent regime.

3 | Discussion

3.1 | The cut-off distance

In the propagation model presented in Section 2, a cut-off distance is used in order to take into account, in a simple way, the microscopic phenomena occurring near the bonding front. Actually, a singularity occurs at the bonding front in the fluid viscous dissipation. A similar issue appears, for example, in liquid drop spreading experiments [127]. In the direct bonding case, both fluid and mechanical phenomena are expected to occur at a micrometer scale in order to resolve the singularities.

The thin plate equation describes the neutral fiber height of the wafer. The film fluid thickness is actually the gap thickness between the two interior wafer surfaces. The assumption is made that, these both heights are equal. This assumption is valid since the thickness change of the wafers remains small compared to the gap height. Close to the bonding front, it is expected that this assumption is not valid anymore. At this scale, the appropriate description of the wafer is more related to a crack in an infinite material loaded by a uniform pressure (see Fig. 14). Then, the gap height profile involves a square root shape, instead of the quadratic shape predicted by the plate theory.

It is interesting to note than h_c should, in consequence, depend on the surface layer mechanical properties, while the macroscopic behavior is dictated by the bulk material properties.

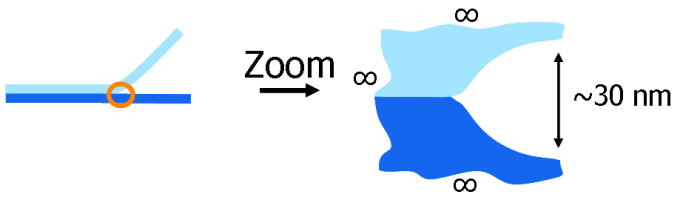

Fig. 14: Schematic view of the expected wafer shape near the bonding front.

In addition, near the bonding front, the fluid pressure becomes very high (up to 10 bars), while the size of the fluid flow becomes very small (some nanometers). For these two reasons, the use of the incompressible Reynolds equation is questionable.

Confined fluid flow regimes are, usually, determined by considering the dimensionless Knudsen number. The Knudsen number is defined as the ratio of the characteristic length scale of the system over the molecular mean free path (λ): $K_n = \lambda/h$.

Many studies in the literature address the issue of gas flow in narrow gaps [128–130]. For instance, this kind of fluid flow regime is present in hard disk drive where the reading head float over an air cushion above the rotating disk (at about 20 nm above the disk). Many phenomenological and theoretical correction models have been proposed to take into account the discrete nature of the gas. Typically, these correction models consist of a slip flow boundary condition on the fluid domain boundary. The slip velocity is then written as

a function of the molecular mean free path. Continuous correction factor could be added to the Reynolds equation and then computed.

The propagation model using such corrections has been tested in the permanent regime (see Appendix A for more details). The molecular mean free path is computed from the gas pressure, which is computed itself from the fourth derivative of the plate deflection. The equation model is, as a consequence, significantly complexified. Anyway, no convincing physical results have been obtained using the model correction (a pressure up to 644 bar at the bonding front is predicted). This can be understood by considering that the molecular mean free path decrease as the gas pressure increase (it is about 10 nm when the pressure is equal to 10 bar). Therefore, taking into account the molecular mean free path inside the model is not sufficient to prevent the singularity issues at the bonding front.

This point is related to the incompressible assumption used inside the model. Because the gas pressure becomes in the same order of magnitude than the atmospheric pressure the compressibility Reynolds equation should be used [123]. Nevertheless, similarly to molecular mean free path issue, the equation is significantly complexified and no numerical results can be obtained, even in the steady state.

This questions, about the mechanical and fluid models validity at the bonding front vicinity, have, in the practice, little importance for the present macroscopic model, since the cut-off length h_c allows to recover what is missing in both the gas flow and mechanical descriptions.

However, the determination of the physical meaning of the cutoff length h_c will require additional work. It is an interesting issue to investigate in more details since the effect of the gas pressure chamber on the bonding velocity has been observed [1]. Because the air viscosity does not depend on pressure, the only remaining possibility is that the cut-off distance is pressure dependent.

3.2 | Wafer support during the measurement

The main difference between the experimental and theoretical curves (Fig. 11) is expected to come from the bottom wafer movement during the bonding. For practical reasons, no active clamping system was used for this experiment (the use of an anti-vibrating slab is more important). A second fluid film is then expected to be present between the support and the bottom wafer. In order to minimize its effect, several minutes of delay are imposed after the bottom wafer is dropped on the support. According to the Fig. 3, an air layer of a few micrometers thickness is still expected to be present. It means that the real bonding configuration is between the “clamped case” (Fig. 6b) and the “smooth support” (Fig. 6c) presented in the Section 1.4. Moreover the final bonded pair of wafers is not perfectly flat, but present a conical shape of about $20\,\mu m$ height (see Chapter III). Thus, the real wafers position and shape during this experiment are more complex than those predicted by the actual model.

4 | Parametric studies

The propagation model is useful to understand the dynamics behavior of the air/wafers coupled system. Many input parameters can be modified and their influence on the bonding dynamics can be studied. Here, the work of adhesion, the initiation force, wafer warp and, finally, the bonding chamber pressure influences for the initiation step, are presented and discussed. Sometimes, the corresponding experimental measurement was possible, in which case they are also presented.

4.1 | Work of adhesion influence

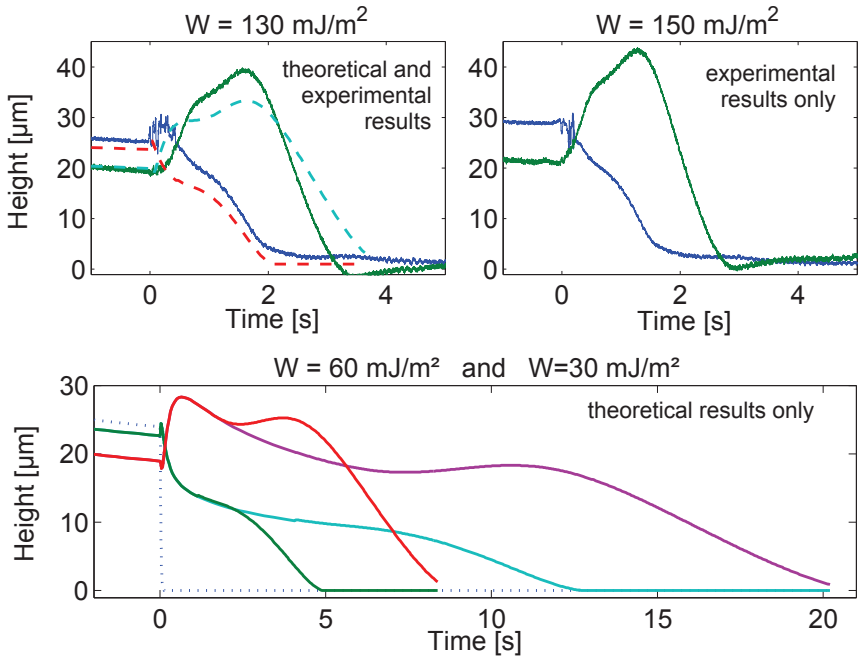

Fig. 15: Influence of the work of adhesion on the evolution of the vertical position of the wafer at the center, at $4\,cm$ and at $9\,cm$ from the center. The work of adhesion is modified by performing plasma activation on both wafers ($\approx 150\,mJ/m^2$), or on only one wafer ($\approx 130\,mJ/m^2$). The bottom graph shows the model predictions for $W = 60\,mJ/m^2$ and $W = 30\,mJ/m^2$. The dotted line is the predicted wafer height at the wafer center.

Similar bonding as those presented in the Section 2.3 have been performed with different work of adhesion values. In the practice, the work of adhesion is modified by using plasma activation (O_2) [1]. A work of adhesion of about $150 \pm 30\,mJ/m^2$ is obtained when the plasma treatment is imposed on both wafers and of about $130 \pm 30\,mJ/m^2$ when the treatment is performed on one wafer only. In addition, simulation results are computed for work of adhesion values equal to $30\,mJ/m^2$, $60\,mJ/m^2$ and $130\,mJ/m^2$. Unfortunately, the non-linear solver is not able to solve the case of $150\,mJ/m^2$. A similar behavior is observed on both experimental and simulation results, see Fig. 15. The first part of the

curves is not modified, while the second bump, observed on the "9 cm" sensor curve, is going higher when the work of adhesion increases.

4.2 | Initiation force influence

Simulation results for various initiation forces are presented in Fig. 16a. As expected, a lower initiation force results in a longer initiation period. It is interesting to note that the time needed to initiate the bonding varies as the logarithm of the initiation force, see Fig. 16b.

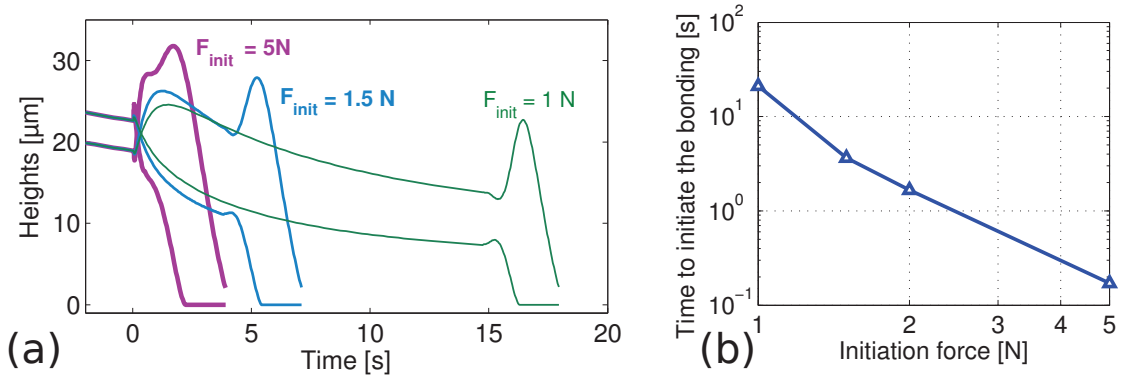

Fig. 16: (a) Influence of the initiation force (theoretical results) on the evolution of the vertical position of the wafer at $4\,cm$ and at $9\,cm$ from the center, for three different initiation forces. The work of adhesion is equal to $W = 112\,mJ/m^2$. (b) The corresponding variation of the initiation time as a function of the initiation force (log-log plot).

Spontaneous initiation case. Spontaneous initiation refers to a situation where initiation occurs without applying an external force on the wafers. As it at be seen in the Subsection 1.2, a very long time is needed for two flat wafers to get into contact. Nevertheless, it is interesting to answer the question of where the contact will occur if enough time is allowed.

Fig. 17 shows the final computation steps of the descent of a flat wafer without any external applied force. The air pressure distribution induces a negative warp to the wafer. This induced warp decreases as the gap between the support decreases. When the gap becomes smaller than the molecular mean free path in the air (about 100 nm at atmospheric pressure) the wafer is no more held, then a sudden fall is expected to occur. The non-linear solver is not able to capture this effect, and then stops (the final minimal gap is here 32 nm after 2 days of descent).

Assuming perfectly flat wafers, a gas bubble is expected to remain trapped in the central part of the wafers, since contact occurs at the edge of the wafer. This is a theoretical answer because, in the practice, for such a small gap between the wafers, the small variation of the flatness of the plate support and of the wafers, as the global system vibrations, become predominant. Therefore, initiation is expected to occur at a random point well before the

prediction given in Fig. 17. The experiment will require a trigger system in order to start the acquisition at the right time.

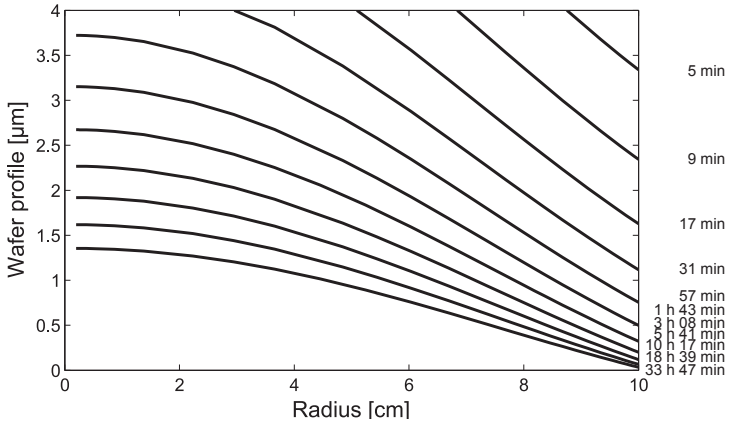

Fig. 17: Final time step of the "before initiation" step when no external initiation force is applied. Time interval are not linear. The gap height at the edge of the wafer for the last computation step is $h(R) = 32\,nm$, and the descent duration is about 1 day and 9 hour.

4.3 | Wafer curvature influence

Processed wafers can have a complex curved shape. For instance, an oxide deposition performed on only one wafer surface leads to a curvature (because of the thermal stress). For similar reasons, wafers having metallic levels, are bowed except if special precautions are taken.

Here, the influence of an uniform curvature k_0 on the bonding dynamics is considered. Because it is easier to figure out, the wafer deflection from center to edge, denoted the bow, is used instead of the curvature. Assuming the wafer profile is quadratic only, i.e. $w(r) = k_0/2\,r^2$, the wafer bow is defined as the deflection of the external wafer edge[1] $bow = k_0/2R^2$.

First, the curvature influence during the "before initiation" step is considered and, secondly, the curvature influence during the propagation step is discussed, in particular the influence on the bonding front velocity.

Initiation step. The time needed for the gap height to become smaller than 100 nm, is computed for different initial bow, when no initiation force is applied (spontaneous initiation case), see Fig. 18. The $100\,nm$ gap is chosen because this is about the molecular mean free path in air at ambient pressure. Below this gap, the adhesion contact is expected to occur.

A small positive curvature increase considerably the needed time for spontaneous initiation to occur. The reason is that the intrinsic curvature balances the induced

[1]This is not the standard bow definition (ASTM).

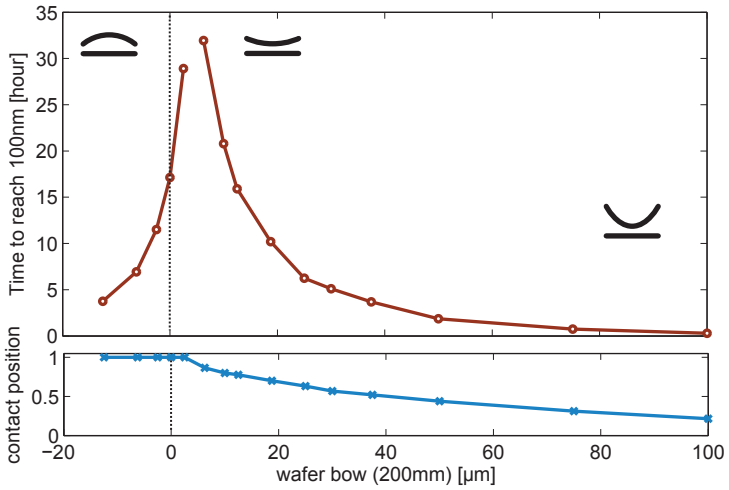

Fig. 18: Variation of the time needed to reach a gap of 100 nm as a function of the initial bow (both concave and convex shape). The contact position is the radius where the contact should occurs, normalized by the wafer radius. Computation is performed for 200 mm diameter wafer.

curvature. Hence, the wafer becomes almost flat when it approaches the bottom surface. On the other hand, a large negative or positive curvature decreases the spontaneous initiation time. It is interesting to note that in the case of a positive curvature, the contact area is not the center of the wafer, but a ring around the wafer center, even for a large curvature (see Fig. 18 and Fig. 19). Thus, an air bubble should remain trapped in central region of the wafer.

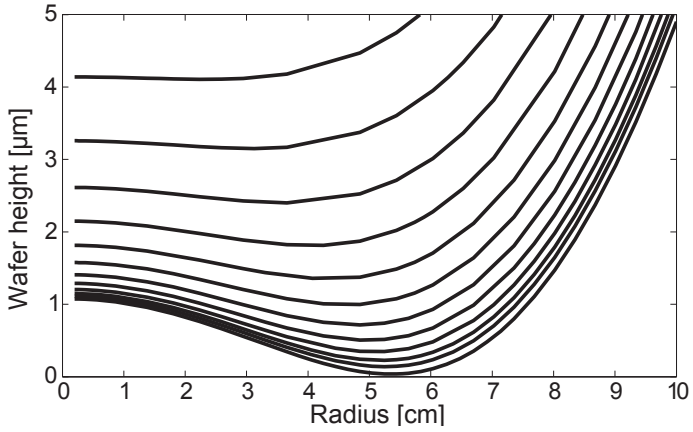

Fig. 19: Final time step of "before initiation" step for a positive initial curvature (here $bow = +37.5\,\mu m$). The spontaneous contact is no longer located at the wafer center, but is a concentric ring. An air bubble is then expected to be trapped in the central region of the wafer.

Propagation step. Wafer curvature has two contributions on the bonding front propagation. On the one hand, the energy balance with the work of adhesion will be modified.

On the other hand, the wafer profile during the propagation will be changed, and then the fluid flow and the viscous dissipation will be affected. The energy balance is modified the same way for both positive or negative curvature, while the viscous dissipation will increase for negative curvature and decrease for positive curvature. Therefore, a model is needed to quantify the importance of the two contributions.

The wafer is assumed to remain flat in the contacted area. Moreover, the geometry is restricted to the 1D plane case (i.e. a beam). The boundary condition on the wafer curvature (eq. 7) is not modified by the initial wafer curvature [126]. Hence, only the boundary condition on the external edge moment is changed: $M_n = Dk_0$.

Computation has been performed in the steady case state, for different initial beam curvatures. The common values are used: $W = 100\,mJ/m^2$, $h_c = 35\,nm$ and $D = 5\,Pa.m^3$. The computed bonding velocity as a function of the equivalent wafer bow is shown in Fig. 20.

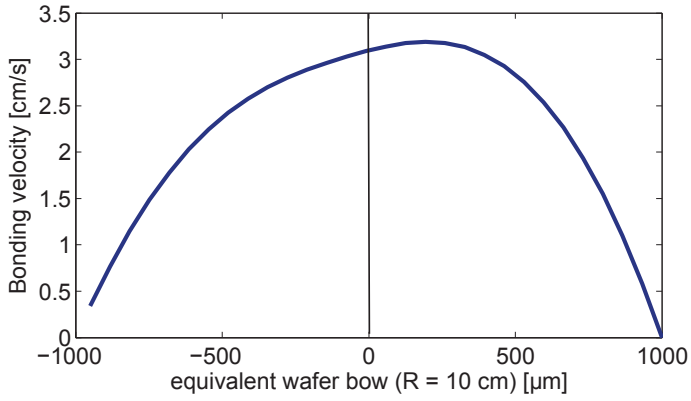

Fig. 20: Bonding speed as a function of the equivalent bow of a 200 mm diameter wafer, computed in the permanent regime. The maximum bow $\pm 1000\,\mu m$ corresponds to the curvature which gives a strain energy equal to the adhesion energy, i.e. $k_{max} = \sqrt{2W/D}$.

It appears that the maximum speed is not obtained with a flat wafer, but with a positive curved wafer. The equivalent bow giving the maximum speed is equal to $193\,\mu m$ for the parameters used here. Nevertheless, the usual bow values, which are in the $\pm 100\,\mu m$ range, have little influence on the bonding speed. It should be noted that for larger bow values, the plane geometry assumption is no more valid.

The fact that an initial wafer curvature can enhance the bonding speed is not intuitive, and an experimental validation is needed.

4.4 | Gas pressure influence during the pre-contact step

Here, only the wafer fall by its own weight is addressed ("spontaneous initiation" case). The fall is slowed down by the air viscosity. Since air is considered as a perfect gas, the viscosity does not depend on the pressure. However, the molecular mean free path is a

function of the pressure. Thus, by using the slip flow model correction (introduced in the discussion Section 3.1, and described in Appendix A), the descent rate of the wafer can be predicted. Several computations with pressure at 1 mbar, 0.1 mbar and 1 bar are shown in Fig. 21.

Since the descent rate is logarithmic, it is not obvious to find out an exact value for the initiation time (from a theoretical point of view, it is infinite). Nevertheless, the model provides some order of magnitude for the spontaneous initiation time : it is about 1 *day* for atmospheric pressure bonding, about 10 *min* at 0.1 mbar, and less than 10 *s* at 1 mbar. This result is coherent with the experimental observation using standard bonding equipment.

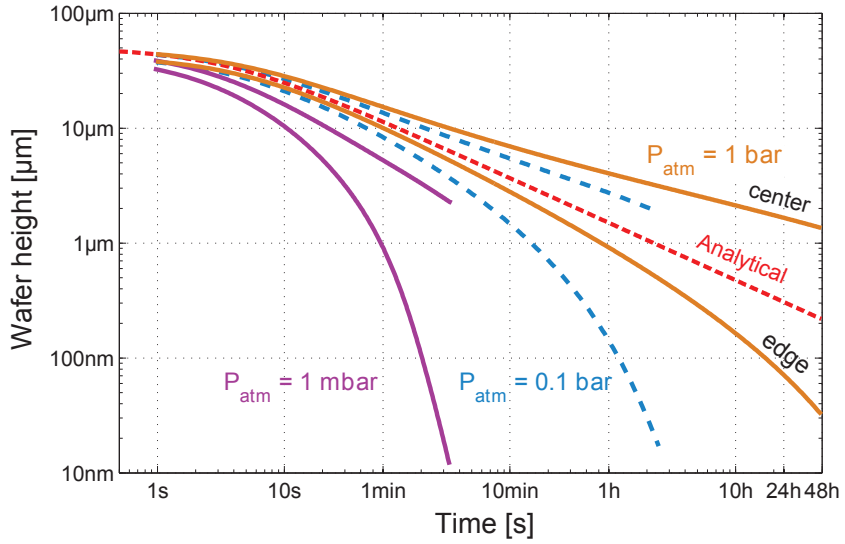

Fig. 21: Predicted descent rate of the central point and of the edge of the wafer as a function of time for three different bonding chamber pressures (1 bar, 0.1 bar and 1 mbar). Computation is performed for 200 mm diameter wafers.

As discussed in Section 3, deriving a model dealing with the ambient pressure for the propagation case is not straightforward. Moreover, inertia of the wafers should be considered for very low pressure.

5 | Extension of the model: two wafers formulation

As explained in the Subsection 1.4, the coupled fluid/structure model could be derived in the configuration where both wafers are free to deform, as long as the contact points with the support are known (case *d* in Fig. 6). In the practice, this condition requires a three points contact between the bottom wafer and the support to be valid. If there are more than three points, the system is overdetermined and an additional computation has to be performed in order to determine where contact occurs. If the number of support points is less than three, the system is unstable. Nevertheless, in order to keep the axisymetric assumption, the “unstable” central point support configuration is considered.

Both theoretical and experimental results in the central point support configuration are presented in the following subsections.

5.1 | Theoretical part

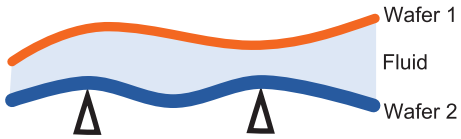

Fig. 22: Two wafers formulation. The top wafer is noted 1 and the bottom wafer, number 2.

Two wafers with different flexural rigidities (D_1 and D_2) are considered (see Fig. 22). Wafer 2 lays on a support in a way that the contact points are always the same whatever the forces acting on the wafers. However, care must be taken that the space below the bottom wafer is sufficient to avoid viscous effects and to prevent unexpected contact points.

The two plate equations for both wafers are:

$$\begin{cases} D_1\, h_1^{(iv)} = +P_{fluid} + G_1 + F_{2\to1} \\ D_2\, h_2^{(iv)} = -P_{fluid} + G_2 - F_{2\to1} + R_{chuck} \end{cases} , \tag{11}$$

where G_i is the weight of the wafer i, P_{fluid} is the fluid pressure, $F_{i\to j}$ is the action of wafer i on the wafer j when wafers are in contact, R_{chuck} are the support forces, and (iv) denotes the fourth spatial derivative.

Instead of working with the wafers vertical position h_1 and h_2, it is more interesting to use the normalized gap thickness, noted g, and the normalized average vertical positions, noted m, defined as:

$$\begin{cases} g = \frac{1}{2D_{eq}} \left(D_1 h_1 - D_2 h_2 \right) \\ m = \frac{1}{2D_{eq}} \left(D_1 h_1 + D_2 h_2 \right) \end{cases} ; \qquad \frac{1}{D_{eq}} = \frac{1}{D_1} + \frac{1}{D_2} \tag{12}$$

where D_{eq} is the equivalent flexural rigidity. Thereby, the two plates equation system becomes:

$$2D_{eq}\, g^{(iv)} = 2P_{fluid} + (G_1 - G_2) + 2F_{2\to1} - R_{support} \tag{13}$$

$$2D_{eq}\, m^{(iv)} = G_1 + G_2 + R_{support} \tag{14}$$

Then, the equation for the average vertical position m (eq. 14) is independent of the fluid pressure, and the gap thickness equation g (eq. 13) is similar to the complete model equation presented before (eq. 6). This simplification is possible because the fluid behavior is only dependent on the thickness of the fluid film and the force acting on it. It does not depend on the average vertical position.

From these equations, the pre-contact dynamics in the two wafers configuration can be

computed. Both experimental and theoretical results are presented in the next subsection. The following paragraph is devoted to the derivation of the propagation boundary condition (eq. 7) when both wafers are free to deform.

Boundary condition for two wafers. The boundary condition used for describing the adhesion at the bonding front, when two wafers are considered, is given by [125]:

$$W = \frac{1}{2}\left[D_1 h_1^{(ii)2} + D_2 h_2^{(ii)2}\right] , \tag{15}$$

where $h^{(ii)}$ is the wafer curvature, at the bonding front position.

The elastic energy of the bonded area is, here, neglected. By substituting h_1 and h_2, using the equation 12, the following relation is obtained:

$$W = \frac{1}{2} D_{eq}\left(g^{(ii)2} + m^{(ii)2}\right) + g^{(ii)}\, m^{(ii)}\, D_{eq}^2 \left(\frac{1}{D_1} - \frac{1}{D_2}\right) . \tag{16}$$

This quadratic equation can be solved to obtain $g^{(ii)}$ as a function of D_1, D_2 and $m^{(ii)}$ which is known. The following relation is obtained :

$$g^{(ii)} = \frac{D_1 - D_2}{D_1 + D_2} m^{(ii)} + \sqrt{\frac{2\,W}{D_{eq}} - \frac{4\,D_{eq}}{D_1 + D_2} m^{(ii)2}} . \tag{17}$$

A similar relation as the one used in the propagation model is obtained (eq. 7) when the effect of gravity is neglected in front of the work of adhesion (i.e. when the $m^{(ii)}$ terms are removed from the above equation).

More work is needed, from this preliminary results, to produce a complete formulation in the two wafers case, which takes into account both gravity effects and the remaining strain energy in the bonded area. Moreover, as it will be presented in Chapter III, additional phenomena have to be taken into account. For this reason, the propagation step in the two-wafers case is not presented here.

5.2 | The central point support configuration

A three contact points support is assumed, in the current derivation. Adding the constraint of a cylindrical geometry leads to the central point support configuration. This situation can be solved using the similar method presented in Section 2 for the one dimensional case. Surprisingly, applying an external force to initiate the bonding, in this configuration, is not necessary.

Both experimental and numerical results are obtained for this configuration. Computed evolution of the wafer profiles are shown in Fig. 23. At the beginning, both wafers involve the same profiles, given by the deflection of a plate under uniform load and hold at the center (dotted line on the left curves). After the first wafer is dropped, the gas pressure increases. The weight of the first wafer is supported by the second wafer, through the gas

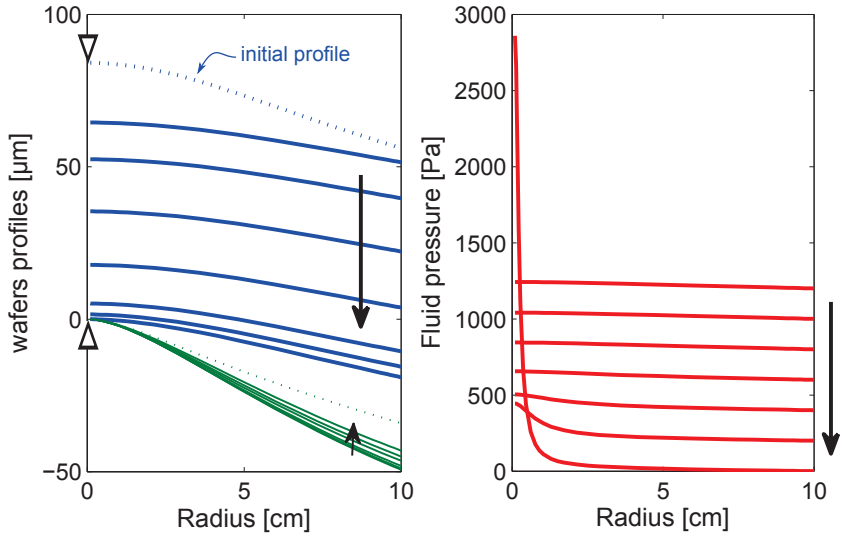

Fig. 23: Wafers profiles (left curves) in the central point support configuration, during the "before initiation" step. The two dotted profiles correspond to the initial state and triangles account for the supports. The right curves show the pressure profile evolution (the curves are shifted by 200 Pa). The pressure rises at the wafer center when contact occurs.

pressure, leading to a change of the second wafer profile. Because the resulting gap between wafers is not uniform, but has a trumpet shape (see Fig. 23), the descent rate increases. Therefore, the spontaneous initiation is achieved in less than 30 seconds, considering 200 mm diameter wafers.

A comparison between experimental and theoretical predictions for gap evolution at the center of the wafers is shown in Fig. 24. Experimental points are obtained by counting the number of interference fringes at the the center of the plate (wavelength equal to 1.1 μm is used).

This bonding configuration is a way to achieve very reproducible bonding. Indeed, no external force is needed to initiate the bonding between the two wafers. Moreover, the

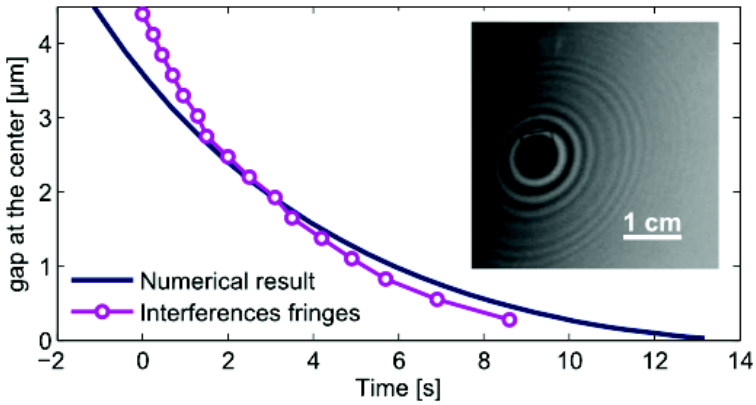

Fig. 24: Evolution of gap between the wafers at the center point of the wafers. The interference pattern, observed by infrared light, is shown in the inset.

interactions between support and wafers are perfectly controlled during the entire bonding sequence, which is not the case when bonding is performed on a flat support. For these reasons, the central point support configuration is used to study the final wafers shape, discussed in Chapter III.

6 | In-plane bonding front observation

Complementary to the presented work, a data treatment method has been developed in order to extract the shape of the bonding front, from the images obtained by infrared light transmission through the silicon wafers stack. In the following, the method is presented and an example of a measurement is discussed.

Because of the additional interface in the non-bonded area, due to the air layer, the non-bonded area appears darker than the bonded area. However, presence of silicon oxide on the surface decreases the optical contrast and, above a certain thickness ($\sim 1\,\mu m$), the contrast could be inverted due to internal interference. Acquisition software allows capturing about 400 pictures at fixed time interval (a good choice is 100 ms). The contrast is not usually very high and there is some noise in the pictures. Moreover, lighting is not homogeneous over the wafer. Thus, image processing is needed in order to extract information, as for example the velocity map, from the set of images.

The idea of the algorithm is to find the transition time (i.e. the image number) between the non-bonded area and the bonded area. For this, the intensity evolution of each pixel is considered independently. Typical intensity evolution curves present a step, corresponding to the transition between the non bonded and the bonded area. For each pixel, the number of the transition image is computed by minimizing the following cost function:

$$f(i) = i\ var\big[\, I_{1\to i}\,\big] + (n-i)\ var\big[\, I_{i+1\to n}\,\big] \tag{18}$$

where i is the image number, n is the total number of images, $I_{i\to j}$ is the set of intensity for images from i to j and $var[\,]$ is the variance function.

Fig. 25 shows two examples of results for 200 mm diameters silicon wafers bonded under similar conditions. Initiation was induced manually at the upper wafer edge. For the second picture, a particle perturbs the propagation, resulting in an interesting propagation pattern.

The first point to note is that the propagation velocity is not constant over the surface wafer. Hence, the bonding front shape is not circular, but has a complex shape. It is expected that the propagation velocity depends both on the distance of the wafer edge, and, in a more complex manner, on the two dimensional induced curvature of the wafer. A curved front shape is not energetically favorable since the wafer is curved on both radial and tangential direction.

How the bonding front propagates across the wafer surface in the 2D general case, as around a defect, is a quite interesting and complex subject to study.

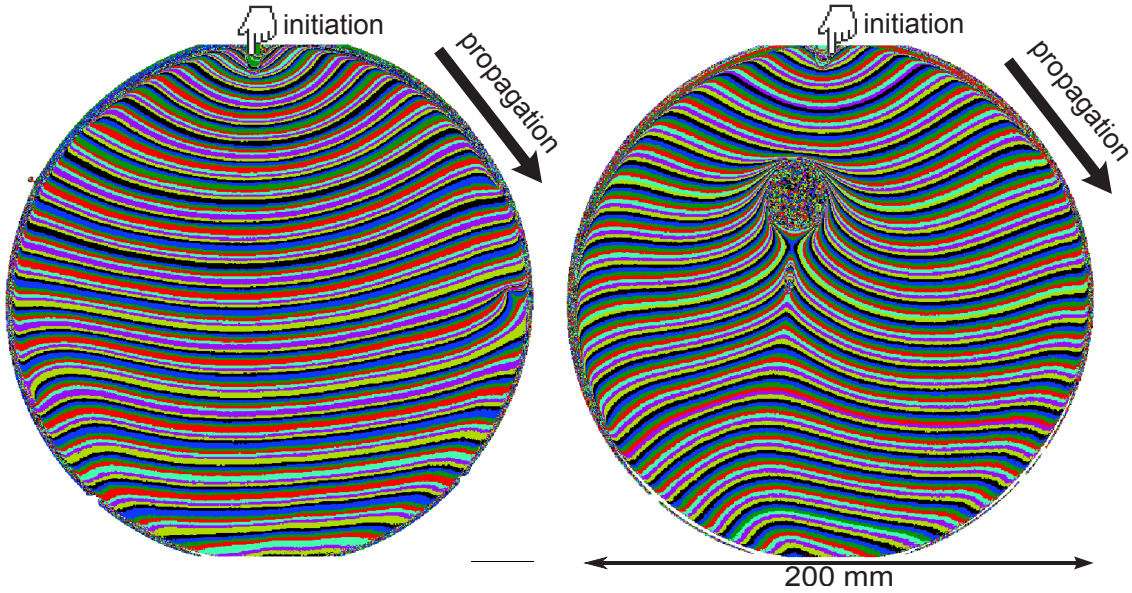

Fig. 25: Example of bonding front characterization after data treatment. Each line represents the bonding front position every 100 ms. For the bonding on the right, a particle is present on the wafer surface, influencing the bonding front propagation and leading to a bubble formation.

7 | Conclusion and perspectives

The contacting step involved in the direct wafer bonding process has been studied, by considering the fluid/structure system formed by the thin air layer, and the elastic deformation of the wafers. The transient equation of the dynamics of wafer bonding front propagation has been numerically solved based on a thin plate theory coupled with the Reynolds equation. The work of adhesion is introduced as a special boundary condition on the curvature of the plate. The contact line singularity is overcome by using an arbitrary cut-off length. The entire bonding process sequence is captured. A novel experimental setup has been used to show that the out-of-plane wafer displacement is accurately predicted by the model. Based on these theoretical and experimental considerations, an improved understanding of the physical phenomena involved in the dynamics of the direct wafer bonding process is achieved.

The following perspectives are indicated:

Concerning the experimental part, the bonding propagation experiments have to be performed using more different process conditions, as for example the support configurations, the wafer material and the thickness, the wafer diameter, the initial bow, the work of adhesion, and how the initiation is performed.

A important future theoretical and experimental work will be to obtain a clear understanding of the physical meaning of the cut-off length. A similar coupled fluid/structure model could be developed at a micrometer scale region around the bonding front, using a 2D elastic model for the wafer (see for example [131]). At this scale, the use of the

incompresible assumption, as the use of the Reynolds equation for the fluid model should be questioned. Then, the dependence of the cut-off length as a function of the absolute pressure and surface mechanical properties, or other parameters could be studied.

Related to the gas flow model, study the fluid flow from the thermodynamic point of view will be interesting. It has been seen that the pressure can rise up to several atmospheres near the bonding front and can encounter rapid change. Defects on the wafer surface, assumed to be induced by the atmospheric water condensation, during the bonding front propagation, have been previously observed [132].

Another substantial theoretical work will be to solve the propagation model in the two dimensions case. A moving boundary problem has, then, to be solved, in addition to the non-linear equation. Level-set methods could constitute an attractive approach to numerically solve this problem.

In addition, layer transfer process involves not necessarily flat and uniform surfaces. Cavities or prominent structures can be present at the interface. Hence, it will be important to understand, based on a 2D model, how the bonding front propagates across a patterned structure.

Chapter III
Post Bonding Wafer Curvature

Abstract

Influence of the wafer bonding dynamics, including the bonding front propagation, on the curvature of the bonded wafers has been observed. This effect can be detrimental for many application, for instance during a circuit layer transfer process. An analytical relation between the final curvature of the stack and the loads acting on the wafers during the bonding, has been derived. Both wafers are described using the thin plate theory. They are bent in the vicinity of the bonding front by the fluid pressure, the gravity, the adhesion forces and the support reaction forces. A strain discontinuity is transferred to the bonding interface because of the elastic deformation in the wafer thicknesses. Because the effect of the fluid pressure appears only if the two wafers are dissimilar, experimentation using two different wafer thicknesses has been performed. The measured bonded wafer profiles are well explained by the proposed model.

Contents

1 | Introduction

It has been previously observed that the bonding process could induce a residual deformation in the final bonded wafers pair. A first mechanical model has been proposed by K. T. Turner et al., considering the curvature induced by a chucking system [64].

However, the bonding dynamics, i.e. the effect of the fluid, which is specific to the direct adhesion case, has not been addressed. The bonding front propagation has an influence on the final bonded wafer macroscopic shape, as repetitively observed at Soitec in experiment. In particular, two flat wafers bonded on a flat support, can lead to a non flat bonded pairs of wafers. In the chapter, the influence of the dynamics of the direct bonding on the bonded wafers curvature is studied.

The main assumption made in the previous study is that the two wafers have the same curvature when they are joined. This assumption, as it will be seen, is no longer required if the bonding front propagation is considered. Because the wafer contact is a dynamic process, and because of the elastic deformation of the wafers in their thicknesses, the two wafers are progressively joined together, while the macroscopic curvatures can be different. Hence, the final shape of the bonded wafers dependents on the both wafer curvatures, at the bonding front position, during the bonding. Therefore, the entire bonding process has to be considered to understand the final residual curvatures.

Based on this idea, an improved physical model is proposed. Theoretical considerations are presented in the first part of the chapter. It includes the derivation of an analytical model which takes into account the bonding front propagation. The second part presents the experimental set-up used to validate the model. Then, the results are presented and discussed. Perspectives for the current work and concluding remarks are included at the end of the chapter.

2 | Theoretical considerations

As mentioned before, the final bonded wafer geometry is influenced by the bonding dynamics. Actually, the final bonded wafer shape is determined by the external loads acting on the system during the bonding initiation and the bonding front propagation.

The analytical derivation of the model follows three sequential steps:

- The final bonded wafer shape is due to a residual moment that induces the bending of the stack of the wafers. The residual moment comes from an elastic strain discontinuity at the interface which is not released during the bonding. In the first part of the derivation, a relation between the residual moment, noted M_i, and the strain discontinuity stored at the interface, noted $\Delta\epsilon$, is obtained.
- In the second part of the derivation, the strain discontinuity is related to the load acting on the bonding front during propagation.

- In the last part of the derivation, the relation between the external loads acting on the two wafers during the bonding process and the load in the vicinity of the bonding front, is given.

The first part of the derivation can actually be found in the work by K. T. Turner et al. [64, 68], and is related to the Stoney formula and its extension for arbitrary film thickness [133, p. 87]. The main new ideas about the effect of the bonding front propagation will be found in the second and third part of the model derivation.

2.1 | The strain discontinuity and the residual bending moment

We experimentally observe, that the final wafer shape can be modified by separating the wafers and bonding them again in a different manner. It means that the deformation is fixed by the bonding interface, and is not irreversible.

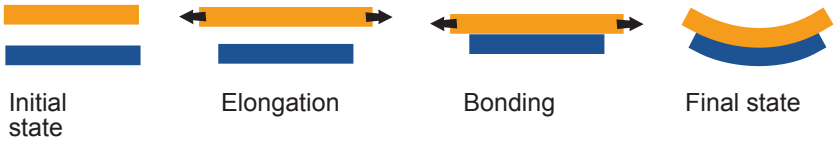

Fig. 1: Schematic representation of the mechanism used to explain how the bonding of two materials can generate a final deformed state.

The mechanism can be understood by considering Fig. 1. Two identical elastic materials are considered. One is elongated by applying in-plane forces. Then, the materials are joined together by keeping the elongation of the first material fixed. Because the interface of the bonding can sustain a shear stress, the final equilibrium of the bonded system is not anymore in the unstrained state. Some elastic strain energy is trapped into the stack. This is the mechanics of the curvature induced by internal stresses in a multilayer structure.

The following derivation is performed to obtain a relation between the elongation fixed during the bonding and the final bonded shape, i.e. between the strain discontinuity $\Delta\epsilon$ imposed during the bonding and the residual internal moment M_i or the final stack curvature k_f.

The thin plate theory is used to model the wafers. A short summary of the thin plate assumption is given first, in order to understand how the bilayer plate model derivation is obtained.

2.1.1 The thin plate theory

The model used to describe the deformation of the bonded wafers pair is derived from thin plate theory [122, 134]. The main assumptions and notations used are described in the following.

The thin plate assumption leads to a linear relation between the moment applied to the plate M, and the resulting curvature $k = \partial^2 w/\partial x^2$ (eq. 1):

$$M = D\,k \quad . \tag{1}$$

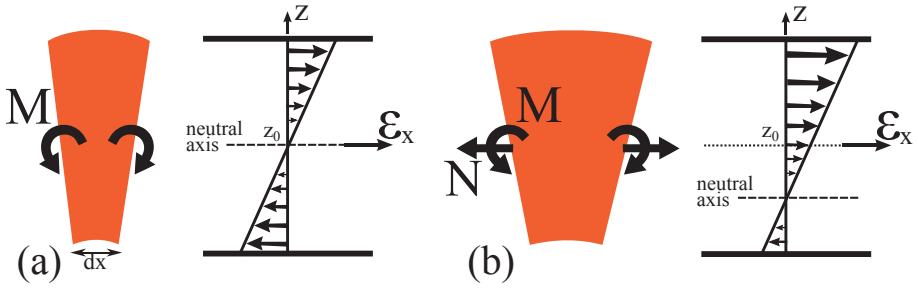

Fig. 2: The in-plane strain is a linear function of the position in the thickness direction. (a) Pure bending case; the neutral axis is at the middle of the plate. (b) When an in-plane load is added; then the neutral axis is moved away from the middle.

The assumption is valid when the deflection of the plate $w(x)$ remains small compared to the plate thickness.

For simplicity, only the one dimensional and plane problem is considered here. The plate curvature along the y dimension is fixed to zero.

The pure bending assumption implies that the strain is linear along the thickness of the plate (see Fig. 2a). The neutral plan is the zero strain plane. Its vertical position is noted z_0. For homogenous material, the neutral plane is located at the middle of the thickness (i.e. $z_0 = t/2$). Then, the strain along the thickness of the plate writes:

$$\epsilon_x(z) = -(z - z_0)\frac{\partial^2 w}{\partial x^2} \quad . \tag{2}$$

In the case of an in-plane load, a constant strain ϵ_0 is added to the bending strain (see Fig. 2b). The relation between the constant strain and the in-plane load N is given by:

$$N = \bar{E}\, t\, \epsilon_0 \tag{3}$$

where $\bar{E} = E/(1-\nu^2)$ is the plane strain modulus, E is the Young's modulus, and ν is the Poisson ratio.

In this case, the reference vertical position used in the curvature relation is still defined with respect to the middle plan (z_0) (which is no more the neutral plane). The in-plane strain becomes (eq. 4):

$$\epsilon_x(z) = -(z - z_0)\frac{\partial^2 w}{\partial x^2} + \epsilon_0 \quad . \tag{4}$$

2.1.2 Bilayer plates model

Due to the initial strain discontinuity at the bonding interface $\Delta\epsilon$, the flat state cannot be reached, and the bilayer system remains in a deformed state. The final curvature k_f will be derived as a function of the strain discontinuity $\Delta\epsilon$.

The first consequence is that the curvatures have to be the same for both plates. The next assumption is that the interface is non-sliding, i.e. a shear stress can be transferred by the interface.

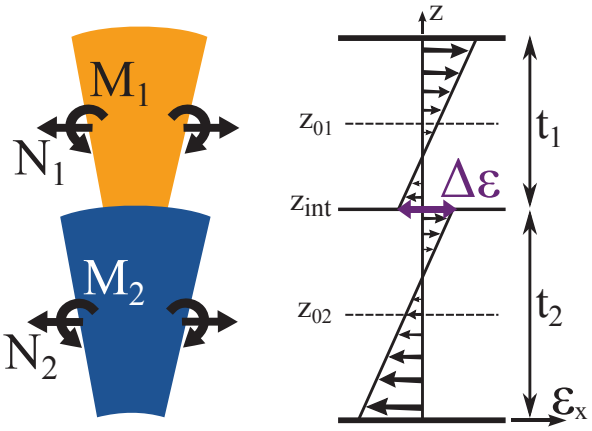

Fig. 3: Notations used herein in order to compute the final curvature.

The top wafer is noted 1 and the bottom wafer is noted 2. The z-axis is the normal to the wafer plane axis. The z-axis origin ($z = 0$) is now located at the bottom surface of the bottom wafer (see Fig. 3).

The strain discontinuity at the interface $\Delta\epsilon$, using an arbitrary sign choice, writes:

$$\Delta\epsilon = \epsilon_1(z_{int}) - \epsilon_2(z_{int}) \tag{5}$$

where z_{int} is the vertical position of the bonding interface (see Fig. 3). Therefore, by combining the strain expression along the z-axes (eq. 4) with the strain discontinuity definition (eq. 5), and by considering that the middle plane positions are $z_{01} = t_2 + t_1/2$ and $z_{02} = t_2/2$, the strain discontinuity writes:

$$\begin{aligned}\Delta\epsilon &= -\left(z_{int} - z_{01}\right)k + \epsilon_{01} + \left(z_{int} - z_{02}\right)k - \epsilon_{02} \\ &= \left(z_{01} - z_{02}\right)k + \epsilon_{01} - \epsilon_{02} \\ &= \frac{t_1 + t_2}{2}\,k + \epsilon_{01} - \epsilon_{02}\end{aligned} \tag{6}$$

Then, the equilibrium curvature ($k = k_f$) of the two plates can be computed, by solving a system of three equations (eq. 7). The two first equations are the force balance and the moment balance. Moments equilibrium is written using the bottom wafer middle plane as the reference plane. The bending moment of the top plate is transferred to the reference plane. The third equation is the constraint on the strain discontinuity $\Delta\epsilon$ at the interface. The three unknowns parameters are the equilibrium curvature k_f and the two constants strain in both wafers ϵ_{01} and ϵ_{02}.

$$\begin{cases} N_1 + N_2 = 0 \\ M_2 + M_1 - \frac{t_1+t_2}{2}N_1 = 0 \\ \Delta\epsilon = \frac{t_1+t_2}{2}k_f + \epsilon_{01} - \epsilon_{02} \end{cases} \tag{7}$$

Therefore, by using the moment equation (eq. 1) and the in-plane force equation (eq. 3)

for both wafers, the following relation is obtained:

$$k_f = \frac{2\left(t_1+t_2\right)\bar{E}_1 t_1 \bar{E}_2 t_2}{\bar{E}_1 t_1 \bar{E}_2 t_2 \left(t_1+t_2\right)^2 + 4\left(\bar{E}_1 t_1 + \bar{E}_2 t_2\right)\left(D_1+D_2\right)} \Delta\epsilon \quad . \tag{8}$$

By considering the equivalent rigidity of the assembled stack D_{12}, a simplified formula can be written (see Appendix C for more details):

$$k_f = \frac{2\Delta\epsilon}{t_1+t_2}\left(1 - \frac{D_1+D_2}{D_{12}}\right) \quad , \tag{9}$$

where D_{12} is given by the following relation [134, p. 232]:

$$D_{12} = \frac{\bar{E}_1^2 t_1^4 + \bar{E}_2^2 t_2^4 + 2\bar{E}_1 t_1 \bar{E}_2 t_2 \left(2t_1^2 + 2t_2^2 + 3t_1 t_2\right)}{12\left(\bar{E}_1 t_1 + \bar{E}_2 t_2\right)} \; ; \quad \bar{E}_i = \frac{E_i}{1-\nu_i^2} \tag{10}$$

In the following, the residual moment M_i is considered instead of the final curvature ($M_i = D_{12}\, k_f$):

$$M_i = \frac{2\Delta\epsilon}{t_1+t_2}\left(D_{12} - D_1 - D_2\right) \quad . \tag{11}$$

2.2 | The origin of the strain discontinuity

In order to determine how the loads which act on the bonding front lead to the strain discontinuity $\Delta\epsilon$, three different scales have to be considered regarding the bonding front mechanics. The smallest, which is nanometric, corresponds to the range of action of the adhesion forces. At a larger scale, which is microscopic, wafers deform elastically through their thickness. At this scale the analogy with a crack propagation in an infinite elastic material is used (see for example ref. [135]). And finally, at the macroscopic scale, wafers are properly described by the thin plate theory, and the bonding front can be seen as the junction of three plates of different thicknesses. A schematic description of the bonding front at the three scales is proposed in Fig. 4.

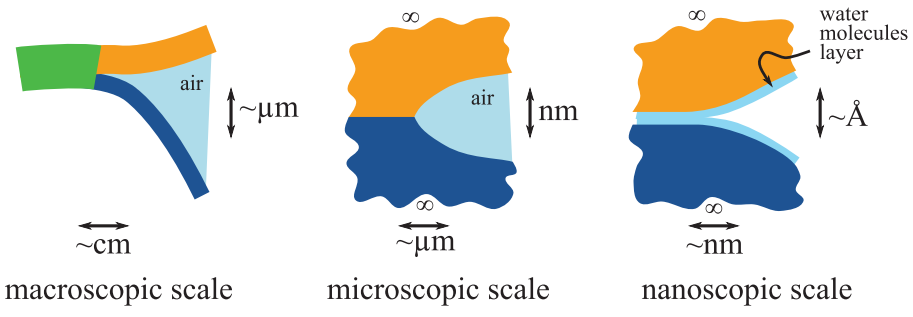

Fig. 4: Schematic picture of the bonding front at the three different scales. At the macroscopic scale the thin plate theory properly describes the wafers shape. At the microscopic scale, analogy with the fracture mechanics theory, can be used. And third, the range of the adhesion forces are nanoscopic, given the thickness of few monolayers adsorbed of the wafers surfaces.

Although the thin plate theory gives an accurate description of the wafer mechanics at the macroscopic scale, it does not explain why a strain discontinuity is produced at the bonding front. Two ideal quadratic surfaces have one contact point only. Therefore, adhesion should not occur. But, since the materials are elastically deformable, and because adhesion forces tend to pull the two surfaces into contact, there is a finite contact area between the two curved wafers. This idea is similar to the Derjaguin, Muller and Toporov model (DMT) or the Johnson, Kendall and Roberts model (JKR) which are both used to study the adhesive contact of an elastic spherical particle to a plane surface [80,81].

Fig. 5 illustrates the expected wafer shape at the bonding front and the shape predicted by the thin plate theory (solid line).

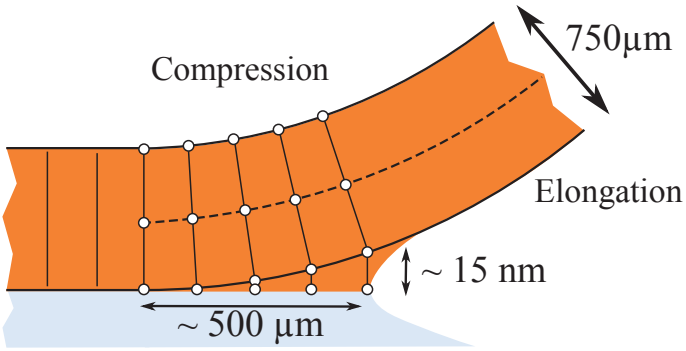

Fig. 5: Schematic representation of the wafer profile near the bonding front. The solid line gives the shape predicted by the thin plate theory. The colored area is the expected real shape. Vertical line represents the normal to the neutral axes line. The upper wafer surface is compressed, while the inner surface is elongated, with respect to the neutral axis. Because the vertical displacement due to the adhesion forces is small in comparison to the plate deformation, the horizontal elongation is expected to remain when both surfaces are pulled into contact. It should be noted, that the scale of this picture is exaggerated. The expected wafer thickness variation is more than one thousand time smaller than the wafer thickness. The real order of magnitude associated to this problem is addressed at the end of the section.

Because the wafers are curved, there is a macroscopic in-plane strain at the inner surface of the wafers. The plate theory allows evaluating this in-plane strain (see eq. 2). The main idea of the present model is to consider that this in-plane strain due to the plate bending is conserved when the interface is created. Indeed, contact between the two wafers occurs while they are both bent with a macroscopically different curvatures.

If absolutely no sliding at the interface, nor shear relaxation occurs after the formation of the bonding interface, the strain discontinuity fixed by the bonding is:

$$\Delta\epsilon_{no\,sliding} = \frac{t_1}{2}\,k_1 + \frac{t_2}{2}\,k_2 = \frac{t_1}{2}\,\frac{M_1}{D_1} + \frac{t_2}{2}\,\frac{M_2}{D_2} \tag{12}$$

The plus sign is because the bonding interface, of the bottom wafer, is above its neutral axis. Then, a positive curvature leads to a negative strain at the interface (compression).

In the case of relaxation or sliding occurs at the bonding interface, the bilayer can be

seen as an unique plate with equivalent stiffness $D_1 + D_2$. In this case, both wafers have the same curvature, noted $k_{sliding}$:

$$k_{sliding} = \frac{M_1 + M_2}{D_1 + D_2} \tag{13}$$

Then, the strain discontinuity writes:

$$\Delta\epsilon_{sliding} = \frac{t_1 + t_2}{2} k_{sliding} = \frac{t_1 + t_2}{2} \frac{M_1 + M_2}{D_1 + D_2} \tag{14}$$

The two situations described above (with or without interface sliding) represent the two extreme cases of the model. The actual behavior of the bonding front at the nanoscale is not known. Therefore, a phenomenological coefficient ϕ is introduced to describe the expected real strain discontinuity (with $\phi \in [0, 1]$):

$$\Delta\epsilon(\phi) = \phi\, \Delta\epsilon_{sliding} + (1 - \phi)\ \Delta\epsilon_{no\,sliding} \quad . \tag{15}$$

The complete relation between the moments applied to the bonding front (M_1 and M_2) and the strain discontinuity is:

$$\Delta\epsilon(\phi) = \phi \frac{t_1 + t_2}{2} \frac{M_1 + M_2}{D_1 + D_2} + (1 - \phi) \left[\frac{t_1}{2} \frac{M_1}{D_1} + \frac{t_2}{2} \frac{M_2}{D_2} \right] \tag{16}$$

where ϕ is a coefficient quantifying to what extend the interface is able to relax the shear stress right after the interface closure.

Same material case. It should be noted that if both wafers are similar, (i.e. same thickness and same material), then the formula 16 simplifies as:

$$\Delta\epsilon_{=} = \frac{t}{2} \frac{M_1 + M_2}{D} \quad . \tag{17}$$

Hence, the value of the sliding coefficient does not matter anymore, because then, the both deformations corresponding to the case with entire relaxation and without are equal.

Estimation of the size of the contact area. By applying the JKR model to the bonding front geometry, the size of the contact area induced by the in-thickness wafer deformation, can be roughly estimated. The two wafers are seen, here, as two elastic hollow spheres in adhesive contact. The following equation, from the JKR model, is used [81]:

$$a^3 = \frac{9}{2} \frac{\pi W}{k_{12}^2 \bar{E}_{12}} \tag{18}$$

where a is the contact area radius, $k_{12} = k_1 + k_2$ is the sum of the two surfaces curvature, and $1/\bar{E}_{12} = 1/\bar{E}_1 + 1/\bar{E}_2$ with $\bar{E}_i = E_i/(1 - \nu_i^2)$.

By considering the following values and assumptions: $E_1 = E_2 = 160\,GPa$, $k_1 = k_2$,

$D_1 = D_2 = 5\,Pa.m^3$, $W = 0.1\,J/m^2$, and $k = 2\sqrt{W/D_2}$ (see next paragraph), the expected radius of the contact area is about $a \sim 480\,\mu m$. Therefore, the corresponding maximum vertical displacement of the surface is about $h_0 = k\,a^2/2 \sim 32\,nm$.

2.3 | External loads at the bonding front

The moments acting at the bonding front can be separated into several contributions, resulting from the gravity, the fluid and from the support reactions. Because the fluid pressure is the same for both wafers, the moment induced by the fluid M_{fluid} is the same for both wafers (opposite sign). Then, the two moments can be written:

$$\begin{aligned} M_1(r) &= +M_{fluid} + M_{g1}(r) \\ M_2(r) &= -M_{fluid} + M_{g2}(r) + M_{support}(r) \end{aligned} \tag{19}$$

It is important to note, that in the case of similar wafers (see eq. 17), the fluid (i.e. the front propagation) has no influence on the final bonded wafer shape, because its effect is symmetric.

The fluid pressure values during the bonding front propagation are complex to known. Nevertheless, as discussed in the second chapter, a simple relation between the wafers curvatures at the bonding front and the adhesion surface energy W can be found (eq. 7, Chapter II, p. 37) [125, 126]. By neglecting the moment due to gravity, as those due to the strain discontinuity stored at the interface, in comparison to the fluid moment, the following relation is obtained:

$$M_{fluid} = \sqrt{2W\frac{D_1 D_2}{D_1 + D_2}} \tag{20}$$

Conclusion of the theoretical part. If the external loads acting on the wafers during the bonding are known, the resulting moments acting in the vicinity of the bonding front can be computed using the equation 19. Then, the strain discontinuity fixed at the interface can be obtained by using equation 16. The residual moment inside the bonded stack is given by equation 11. The last step is to solve the plate equation (in 1D, eq. 1) in order to obtained the final shape of the bonded stack.

3 | Experimental methods

The experimental set-up, used to study the bonded wafer curvatures induced by the bonding, has to satisfy two main constraints. The first one is that all the external forces acting on the wafers have to be known. For this reason, we have used a bonding configuration employing a central point as wafer support. More details are given in the next paragraph. The second constraint on the experiment is that the two wafers have to be dissimilar.

As seen in the theoretical part, there is no effect of the front propagation when identical wafers are used. The simplest solution, to validate the model, is to use two different wafer thicknesses.

The following paragraph details the choice of the bonding configuration. Afterwards, the analytical model is applied specifically to the bonding configuration. And third, the experimental methods are presented. Results are presented and discussed in the Section 4.

3.1 | Choice of bonding configuration

The most common bonding configuration, where the wafers lay on a flat support, is not convenient here because the contact area between the support and the bottom wafer may change during the bonding process. Moreover, when using a flat support, an initiation force must be applied and therefore it has to be known. For these two reasons, another bonding configuration is used, i.e. the central point support configuration, presented in the Chapter II (see p. 52). An illustration of the corresponding bonding sequence is shown Fig. 6.

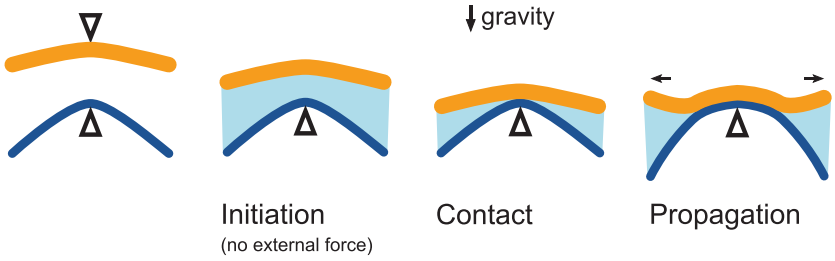

Fig. 6: The bonding sequence in case of the central point support bonding configuration. Triangle represents the support contact point. Both wafers are initially flat and the downward curvature is induced by the gravity.

In this configuration wafers are held only at the center. Then, the support reaction force is always the same whatever the shape taken by the wafers during the bonding.

Moreover, in this configuration there is no need to apply an external force in order to initiate the bonding within a reasonable time. This can be understood by considering that the weight of the first wafer is transferred to the second wafer, by the fluid pressure. Then, the second wafer is more bent than the first. The air layer thickness profile takes a sort of trumpet shape and therefore the air flow is facilitated. Spontaneous initiation is observed less than $30\,s$ after the drop. The model of the fluid/structure system presented in the Chapter II allows the prediction of the movement of both wafers during the initiation step (see Subsection 5.2, Chapter II, p. 52).

Thanks to this bonding configuration, all the external load values acting on the wafers during the bonding process are known, this, using a very simple experimental set-up.

3.2 | Numerical application

Because of the specific configuration of the bonding support, there is no support reaction moment $M_{support}$ to take into account. The two remaining external loads result from gravity $M_{grav}(r)$ and from the fluid M_{fluid}.

The moment induced by the fluid is assumed to remain constant over the radius, while the moment due to the gravity is a function of the bonding front position.

Then, the strain discontinuity formula (eq. 16) is split into two different contributions:

$$\Delta\epsilon(r) = \Delta\epsilon_{grav}(r) + \Delta\epsilon_{fluid} \quad , \tag{21}$$

with the following expression for the two contributions:

$$\Delta\epsilon_{grav}(r) = \phi\,\frac{t_1+t_2}{2}\,\frac{M_{g1}(r)+M_{g2}(r)}{D_1+D_2} + (1-\phi)\left[\frac{t_1}{2}\frac{M_{g1}(r)}{D_1} + \frac{t_2}{2}\frac{M_{g2}(r)}{D_2}\right] \tag{22}$$

$$\Delta\epsilon_{fluid} = (1-\phi)\,\frac{1}{2}\left(\frac{t_1}{D_1} - \frac{t_2}{D_2}\right) M_{fluid} \tag{23}$$

Because the system is circular, the simple one-dimensional linear relation between the bending moment and the curvature cannot be used (see eq. 1). Instead, the axi-symetrical plate equation has to be solved (eq. 24) [122]:

$$M_r = -D\left(\frac{\partial^2 w}{\partial r^2} + \frac{\nu}{r}\frac{\partial w}{\partial r}\right) \quad , \tag{24}$$

where M_r is the radial moment and $\partial w/\partial r$ is the wafer slope. This equation is solved in the case of an uniform pressure $p^\star$ and in the case of a uniform moment $m^\star$, corresponding to the gravity and fluid contribution:

$$w_{grav}\,(r) = -\frac{p^\star}{64D}\,r^2R^2\left[\left(\frac{r}{R}\right)^2 + 2\frac{3+\nu}{1+\nu} - 8\,ln\left(\frac{r}{R}\right)\right] \tag{25}$$

$$w_{fluid}(r) = -\frac{r^2}{2\,(1+\nu)}\frac{m^\star}{D} \tag{26}$$

The expression for the constant moment $m^\star$ is obtained from the strain discontinuity equation (eq. 23) combined with the residual moment equation (eq. 11):

$$m^\star = \frac{D_{12}-D_1-D_2}{t_1+t_2}\,(1-\phi)\left(\frac{t_1}{D_1} - \frac{t_2}{D_2}\right) M_{fluid} \quad . \tag{27}$$

The expression of the uniform load $p^\star$ is obtained from the strain discontinuity equation (eq. 22) combined with the residual moment equation (eq. 11) and, in this case, by considering the linear property of the plate equation:

$$p^\star = \frac{D_{12}-D_1-D_2}{t_1+t_2}\left[\phi\frac{(t_1+t_2)^2}{D_1+D_2} + (1-\phi)\left(\frac{t_1^2}{D_1}+\frac{t_2^2}{D_2}\right)\right]\rho\,g \quad , \tag{28}$$

where ρ is the material density and g is the gravity constant.

M_{fluid} is given as a function of the work of adhesion W by equation 20.

Finally, the total wafer deflection is obtained by summing the fluid and the gravity contributions:

$$w_{total} = w_{grav}(r) + w_{fluid}(r) \quad . \tag{29}$$

3.3 | Experimental procedures

Bulk silicon wafers with 500 and 717 μm thickness have been used. The crystal orientation of the surface plane is (100). Standard cleaning (SC1 and SC2) is performed before bonding. The work of adhesion is equal to $W \approx 90\, mJ/m^2$ (the testing method is presented in details in Chapter IV, Section 3).

The wafer thickness and bow are measured prior to bonding. The wafer thickness variation is less than $\pm 1\, \mu m$, and the bow is less than $5\, \mu m$ for both wafer thicknesses.

Four permutations are possible, relative to gravity, with two different wafer thicknesses: 717/717 μm, 717/500 μm, 500/717 μm, and 500/500 μm.

The central support is a simple plastic element about $2\, mm$ height and $5\, mm$ diameter. No contact is observed between the bottom wafer and the bottom support plate, and the two wafers stack is stable. The bottom support plate is slightly tilted downward, in such a way that two end-stops allow the alignment of the wafers. Moreover infrared light observation of the bonding front propagation is performed during the experiment. An almost circular front shape is observed.

The four bonding permutations have been performed at least two times each and a good reproducibility of the results is obtained.

Final shape measurement. A mechanical profilometer (KLA-Tencor P16) is used to measure the final shape of the bonded wafers. A stylus comes into contact with the surface, and is moved across a diameter ($18\, cm$ only). During measurement, the wafers lay on a three points support. In order to correct for deformation due to the gravity, measurements are made on both sides of the wafer stack. Then, because the thin plate equation is linear, the average of the two profiles gives the wafer shape without any gravity effect. Finally, the resulting curves are leveled with a line going through the first and the last points.

Two diameters orientation are measured for each bonding, one in the <100> direction and the other one in the <110> direction of the silicon wafer crystal structure.

4 | Results and discussion

4.1 | Main results

All the four bonded wafers pairs demonstrate a different profile, ranging from about $-100\, \mu m$ to $+20\, \mu m$ bow (center to edge). Fig. 7 shows the results, for the <110> crystal

direction. The 500/717 μm bonding has the most complex shape. The curvature is positive, except near the wafer center where it is negative. This is the only permutation where the resulting bow is positive. Both the 717/717 μm and the 500/500 μm configurations have a similar shape, except for the amplitude. Wafers are curved downward, and the curvature becomes almost zero at the outer extent of the wafers (even slightly positive in the <100> direction). The configuration 717/500 μm is the most curved bonded pair, with a bow of about $-100\,\mu m$. The shape is almost a pure quadratic curve (constant curvature).

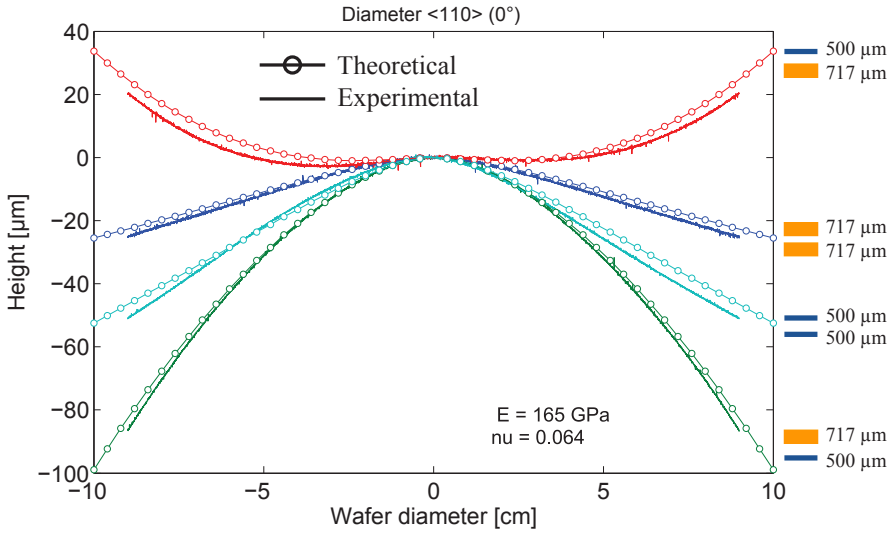

Fig. 7: Results for the four thickness permutations, which are from top to bottom: 500 μm over 717 μm, 717 μm over 717 μm, 500 μm over 500 μm and 717 μm over 500 μm. Measurements are made perpendicular to the notch direction, i.e. in the <110> crystal direction and the gravity effect is corrected. Circles indicate the theoretical prediction using $W = 90\,mJ/m^2$ and $\phi = 0.67$.

In the case of wafers with different thicknesses, the thin wafer acts like if it was pulling the stack in its direction. In other words, the bonded stack is curved towards the thin wafer. The thin wafer is more curved during the bonding (because of the smaller flexural rigidity), and its inner surface is thus more elongated when it is brought in contact with the other wafer. The model provides a very good description of the experimental results.

Moreover, the agreement is quantitative. Theoretical curves are computed using the work of adhesion value of $W = 90\,mJ/m^2$ and an adjusted sliding coefficient of $\phi = 0.67$. The silicon Young's modulus along the <110> direction is taken equal to $E_{110} = 165\,GPa$ and the Poisson ratio is equal to $\nu_{110} = 0.064$ [136]. The same shape and amplitude is found between the measurement and the model prediction using always $\phi = 0.67$.

The sliding coefficient value of $\phi = 0.67$ means that about one third of the deformation induced by the propagation of the bonding front is not released after the interface has closed up.

The small discrepancy between the theoretical and experimental curves could possibly be explained by the strong isotropic assumption made for the model derivation. Wafers

shape profile have been also measured along the <100> crystal direction. The silicon Young's modulus along the <100> direction is taken equal to $E_{100} = 130\,GPa$ and Poisson ratio to $\nu_{100} = 0.3$ [136]. Fig. 8 shows the experimental and the predicted results of the final bonded wafer shape.

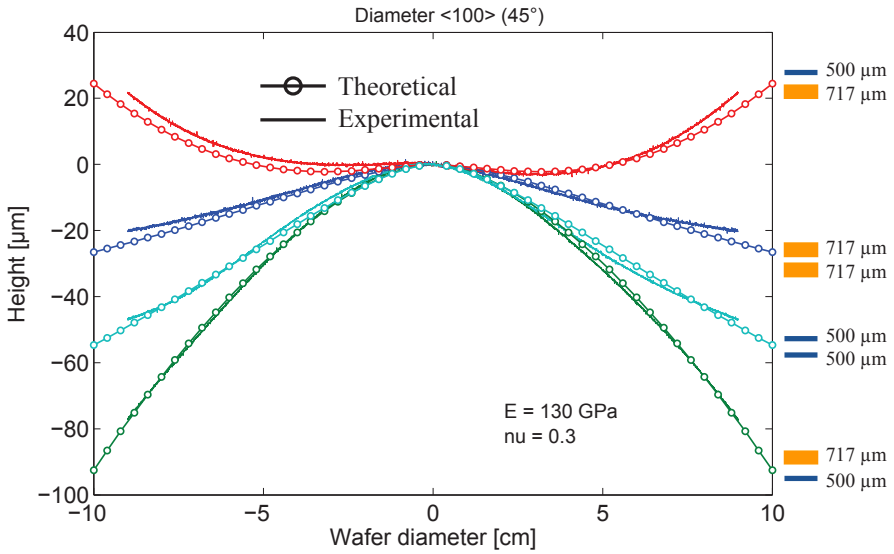

Fig. 8: Post bonding wafer shape profile along the <100> crystal direction. The mechanical properties used are $E_{100} = 130\,GPa$ and Poisson ratio $\nu_{100} = 0.3$.

As shown in Fig. 7 and Fig. 8, the two experimental curves are surrounded by the two isotropic model prediction using two different Young modulus and Poisson ratio.

4.2 | Discussion about model hypotheses

As previously mentioned, some equations of the model are derived assuming the one dimensional plane geometry (eq. 11 and eq. 20). Hence, the axisymetric contribution on the final deformation is not entirely taken into account. Nevertheless, the bonding front propagation is, in this experiment, only radial. Therefore, the strain discontinuity is expected to be mainly along the radial direction, and negligible in the tangential direction.

Although, a sliding coefficient value was suggested from the experimental results, it is difficult to conclude about its actual value, as about its definitive physical meaning. Further work is needed to better understand the bonding interface properties at the nanoscale.

4.3 | Additional results on other configurations

The final shape of the bonded wafers depends strongly on the bonding configuration, i.e. how the wafers are hold during the bonding. For simplicity a specific configuration has been used, here, to validate the proposed model. However, in the practice, many different bonding configurations are encountered, leading to many different final shapes. Some of them are presented in the following.

4.3.1 Final shape in the clamped configuration

When the bottom wafer is rigidly clamped to a flat support, its flexural rigidity can be considered as infinite. In this case, the bonding front propagation has an effect on the final bonded wafer curvature, although the two wafers are similar. Then, the strain discontinuity formula (eq. 16) can be simplified as:

$$\Delta\varepsilon_{clamp} = (1-\phi)\,\frac{t_1 M_1}{2D_1} \quad . \tag{30}$$

The resulting shape after bonding, assuming gravity is negligible, is a positive quadratic shape. This is observed experimentally when a vacuum chuck is used (see Fig. 9a).

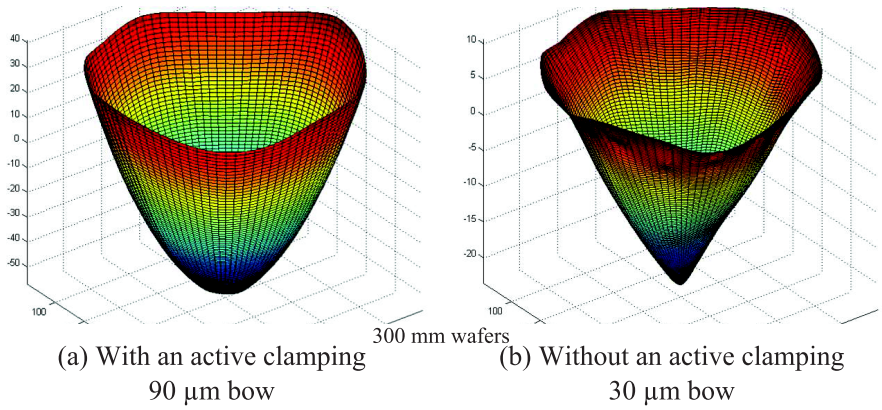

Fig. 9: Final bonded shape of bulk silicon 300 mm diameter wafers, obtained using a flat support during the bonding. (a) An active clamping system is used (vacuum) (b) No active clamping system is used. Moreover, the support is grooved. Initiation are performed, in both case, at the wafer center.

When the bonding is performed without the vacuum active clamping, but on the same support, a conical final shape is observed (see Fig. 9b). In this case, there is no effect of the fluid pressure because both wafers are similar. Moreover, the effect of the gravity seems negligible. It is expected that the wafer weight support is shared between the wafer center and the wafer edge, hence reducing the effect of the gravity. Furthermore, a strong initiation influence is observed. This can be understood by considering that, at the first wafer contact, the top wafer is significantly curved by the initiation force while the bottom wafer remains flat on the support. Then, the curvature difference leads to a strong final positive curvature around the initiation point. This configuration corresponds to the grooved support presented in Chapter II (see Subsection 1.4, Chapter II, p. 34).

4.3.2 Vertical bonding

The most direct way to obtain a flat bonded pair, starting from two flat and similar wafers, is to keep the bonding process symmetric. To remove the non symmetric effect of the gravity and of the initiation, a bonding test was performed along a vertical plane. Two silicon

wafers are first bonded using the conventional process, horizontal, as already described in Chapter II. Afterwards, the bonded pair is placed vertically and manually held at the upper side. The wafers are partially separated (one or two centimeters from the edge) by inserting a plastic blade from the bottom edge. After separation, the blade is completely removed and the wafers re-bonded, still maintained at the upper side. Experiments have been performed in the case of similar wafers (717/717 μm) and in the case of dissimilar wafers (500/717 μm). The obtained profiles are presented Fig. 10.

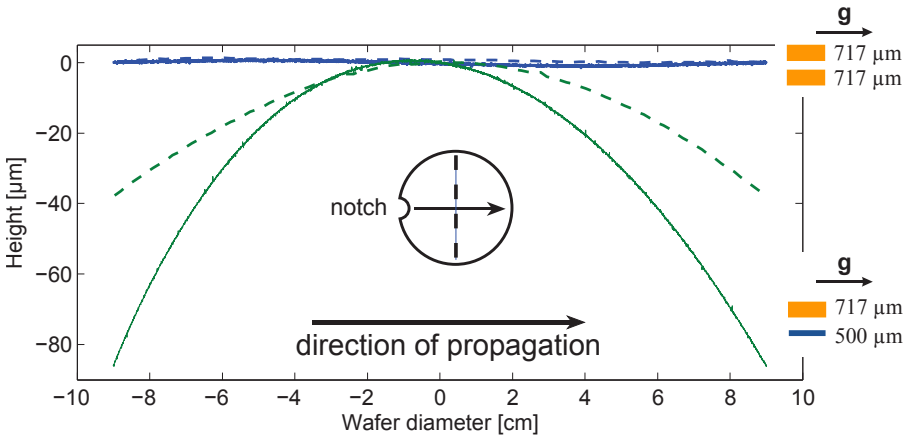

Fig. 10: Experimental profiles of bonded wafers using the vertical configuration. (Blue curves) Both wafers have the same thicknesses. (Green curves) One wafer is thinner, leading to a curvature of the bonded wafers. Dashed lines are the experimental profile in the direction perpendicular to the propagation.

In the case of similar wafers, the resulting final bonded shape deflection is about $\pm 2\,\mu m$, which is on the same order of magnitude as the pre-bond bulk wafer flatness and thickness variation, and within the measurement error. As expected, a symmetric bonding configuration leads to a flat final bonded wafer shape (there is, actually, no need for a complex model to predict this result).

In the case of dissimilar wafers, the situation is no more symmetric and then the resulting bonded stack is curved. As predicted by the model, the final stack is curved toward the side of the thin wafer. However, more work is needed to obtained an accurate model prediction for this bonding configuration, in particular because the actual bonding front shape is unknown for this experiment.

5 | Conclusion and perspectives

A new model has been proposed to explain the residual curvatures of bonded wafers. In this model, the specific direct bonding dynamics is considered. Due to the bonding front propagation, the deformation can be progressively locked at the interface, along the bonding front path. The deformation due to the bending of the wafer is transferred to the bonding interface, because of the mechanical deformation around the bonding front at the microscopic scale.

The model predicts that the propagation has an effect when the two wafers are dissimilar only (or if one is clamped). A specific bonding configuration has been used, in such a way that all the loads acting on the wafers during the bonding have been known. Wafers with two different thicknesses have been bonded together using four different permutations.

A good agreement between the theory and the measurement is obtained for the four bonding permutations. Moreover, the model allows to understand the final shape of the bonded wafers obtained for other bonding configuration, in particular when one wafer is clamped. A sliding coefficient has been introduced in the model in order to take into account the relaxation by sliding of the bonding interface. More work is needed to conclude about its physical meaning and value.

Additional experiments are possible to extend and validate the model to other situations. The first one, could be to change the work of adhesion, still with wafers of different thicknesses. In addition, because the thickness of the wafer appears in the theoretical model, both in the flexural rigidity expression and as a geometrical parameter (in the strain expression), it should be interesting to dissociate this two effects by changing the flexural rigidity without changing the thickness of the wafer. This can be achieved using different materials for the wafers.

Another experience could be to change only the material of the surface. Since the strain discontinuity storage involves local deformation of the wafer near its surface, changing only the surface material could have an influence on the final bonded shape, while the two parameters used in the present model will remain the same (the flexural rigidity and the wafer thickness).

Moreover, a better mechanical description of the bonding front at the microscopic scale is needed, as to write the complete two dimensional equations of the model. Further perspectives will consider no initially flat wafers and other bonding configurations.

Chapter IV
Work of Adhesion

Abstract

The work of adhesion is the energy per unit area which drives the bonding front propagation. It is due, at the nanometer scale, to the hydrogen bond interaction between water molecules adsorbed on the wafer surfaces. Moreover, the surface presents some roughness at a larger scale. A model is derived to take into account both the interface roughness, and the amount of water present at the interface. The interface energy for adhesion is found different than for separation because of the different distribution of water along the interface gap. In addition, a new method to accurately measure the work of adhesion using entire wafers is proposed. A thin piece of polymer is intentionally placed on the wafer surface prior to bonding, in order to create a bubble between the two bonded wafers. The measurement of the deflection profile of the wafers and a simple mechanical model allow the determination of the work of adhesion.

Contents

1 | Introduction

In the case of direct wafer bonding, the work of adhesion is defined as the energy per unit area driving the bonding front propagation. In other words, it is the gain in energy made by the bonding system when the bonding front moves over a certain area.

As discussed in Chapter I (Section 2, p. 17) many issues are related to the work of adhesion, in the case of direct hydrophilic wafer bonding.

One issue concerns the fact that the bonding interface energy, which is usually measured by opening the interface, is different than the actual value of the work of adhesion, driving the interface contact. Moreover, the actual value of the work of adhesion is critical since it is an input parameter of the bonding propagation model (discussed in Chapter II) and is also needed to explain the influence of the bonding propagation on the final wafers curvature (discussed in Chapter III).

The first section of the chapter is devoted to the derivation of a microscopic model of the hydrophilic bonding interface. This model allows the prediction of the work of adhesion as a function of the surface roughness and the amount of water adsorbed on surfaces and is based on molecular dynamics simulations obtained by D. J. Cole et al. [38]. The observed interface energy hysteresis between closure and opening of the interface can be explained by considering water diffusion along the bonding interface.

The second section of the chapter describes a novel experimental method, developed to directly measure the work of adhesion.

2 | Bonding interface model

2.1 | Consideration of length scales

Wafers interface adhesion involves many phenomena taking place at the nanometer scale up to micrometer scale. In the case of hydrophilic direct bonding, the wafer surfaces are covered by hydroxyl groups ($-OH$) and the bonding interface is filled with a few layers of water molecules. In addition, the surfaces involve a roughness that impact the adhesion contact.

The chemical aspects of the bonding interface have been studied using molecular dynamics simulations [36–39]. Molecular dynamics simulations are based on the computation of Newton's law of motion for a few thousands atoms in a periodic box, which is about $30\times30\times20$ Å in size, in the study of interested here. The interaction forces description between atoms constitute the main input parameters. They are fixed in such a way that the macroscopic properties of material are retrieved or to match other simulation results based on quantum mechanics (Density Functional Theory).

Surface roughness is usually measured using atomic force microscopy (AFM), which consists in approaching the surface with a micro-fabricated tip, thanks to a piezoelectric material, and to observe its vertical displacement using a reflected laser beam. Root mean

square values are typically equal to about $1-2\,\text{Å}$ RMS for a native silicon oxide surface or for a thin oxide layer. Hence, the surface height variation is on the same order of magnitude as the water molecule size ($\sim 3.1\,\text{Å}$).

A portion of an experimental AFM profile, the thickness of one monolayer of water and the box size of the molecular dynamic simulation are shown, in Fig. 1, in order to figure out what are the different length scales playing a role in the adhesion of two surfaces. In addition, the AFM tip is schematically represented by an ellipse.

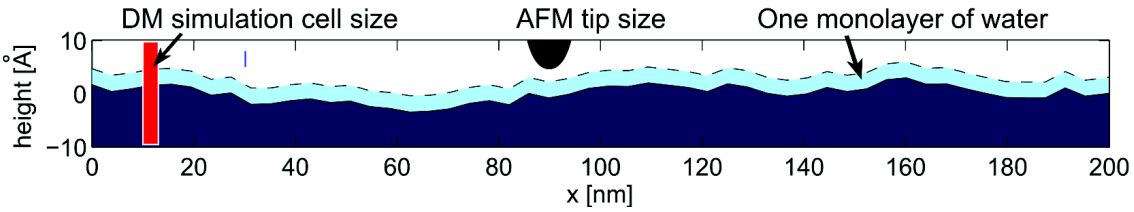

Fig. 1: The dark area is a small part of an experimental AFM profile. Each point is located at every $\Delta x \approx 40\,\text{Å}$ ($2\,\mu m$ long scan for 512 points). The dashed line represents one monolayer of water molecules ($3\,\text{Å}$) and the rectangle represents the box size of the molecular dynamic simulation ($30\times30\times20\,\text{Å}^3$). The AFM tip radius is typically about $10\,nm$. It should be noted that the x-axis scale is ten times larger than the z-axis scale. The roughness value for the entire AFM scan ($2\times2\,\mu m^2$) is about $1\,\text{Å}$ RMS.

Some assumptions can be made from the Fig. 1. First, the surface topology is extremely flat, meaning that the curvature of the surface should not have an effect on the water layer, and then its thickness, and its chemical state, should be uniform over the wafer surface. However, once the interface is closed, the interface gap height is expected to play an important role, since a constraint is added on the local thickness of the water layer. Secondly, the silica (or silicon) material can be considered non-deformable, as long as, one or a few monolayers of water are present between the two surfaces. Thirdly, the molecular dynamics simulation cell is too small to account for surface roughness obtained from an AFM.

Therefore, a model of the bonding interface, at a micrometer scale, is required. This model should take into account the surface roughness, the water diffusion along the interface and the resulting inhomogeneity of the water coverage.

The molecular dynamics simulation results. D. J. Cole et al. [38] have computed, using molecular dynamics simulation, the force between the two substrates as a function the separating distance, called z, and as a function of the amount of water filling the gap, noted ML (number of mono-layers), see Fig. 2. Because this force is produced at a nanometer scale, it is noted in the following, $f_{nm}(z, ML)$.

The interface roughness. The roughness of a surface is usually defined as the root mean square value (RMS) of the surface height statistical distribution. In case of bonding,

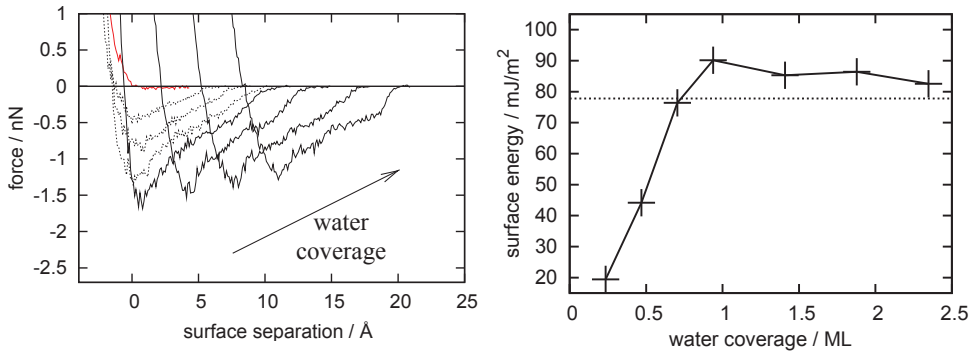

Fig. 2: (left) Force-separation curves for two hydroxylated amorphous silica surfaces. From left to right, the curves correspond to approximately 0.25, 0.50, 0.75, 1.00, 1.50, 2.00 and 2.50 ML water coverage on each surface. (right) Variation of the surface energy (i.e. half of the interface energy) as a function of the water coverage in case of amorphous silica hydrophilic bonding. The reference surface area for the force computation is $30 \times 30\,\text{Å}^2$. Data points are obtained by integrating the force curves. The dotted line represents the surface tension of water ($\sim 72\,mJ/m^2$). Both graphs are taken from D. J. Cole et al. [38].

the interface gap height has to be considered, which is given by the statistical distribution of the distance between the two surfaces in front of one another. Then, the interface roughness σ, is defined as the standard deviation (i.e. the root mean square value) of the interface gap height distribution, and it is determined from the two surface roughnesses σ_1 and σ_2, by the relation $\sigma^2 = \sigma_1^2 + \sigma_2^2$, where both surfaces topographies are assumed to be uncorrelated.

The height distribution of the surface, and then of the bonding interface, is well described by a Gaussian distribution:

$$G(z,\,\sigma) = \frac{1}{\sigma\sqrt{2\pi}} \exp\left(-\frac{z^2}{2\sigma^2}\right) . \tag{1}$$

2.2 | Theoretical considerations

2.2.1 Description of the model

Two cases are distinguished in the interface model: the first corresponds to the adhesion of the two surfaces, and the second corresponds to the separation of the interface. The difference between both cases is given by how the water is distributed along the bonding interface. Fig. 3 is a schematic representation of the bonding interface, before the contact (a), just after the contact (b), and before the separation (c).

Before the bonding, the water layer is assumed to be uniformly distributed on the wafer surface (Fig. 3a). As discussed before, the variation of the surface topography is too small to have an effect on the water coverage distribution. When the two surfaces are brought in contact, the water layer is, at some point, in compression and at other point under tension (Fig. 3b). Because the water layer consists of some mono-layers of molecules only,

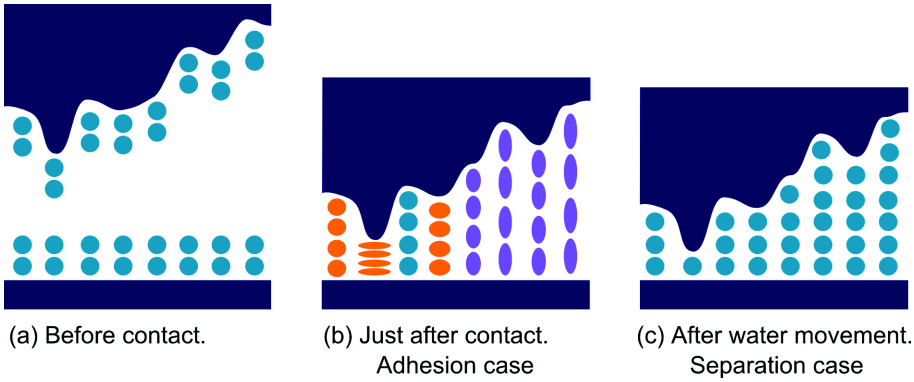

Fig. 3: Schematic representation of the bonding interface. The plain circle represents monolayer of water molecules. (a) Before surfaces are brought in contact, they are covered by an uniform layer of water. (b) Configuration just after the bonding of the two surfaces. The water layer is in compression at some surface points (orange) and in elongation at other points (purple). The work of adhesion is calculated using this configuration as reference. (c) After some time, the water distribution along the interface is assumed to be not uniform anymore. The local amount of water is then a function of the local interface gap, in such a way that the global system energy is minimized. The work of separation is calculated using this configuration as reference.

the water movement along the interface is assumed slower than the characteristic time of the bonding, i.e. the water does not flow along the interface during the bonding, and then the water molecular layer can be under tension. This point is discussed later. The molecular dynamics simulation gives the attractive or repulsive forces as a function of the distance gap and as a function the quantity of water molecules (Fig. 2a). Then, by solving the mechanical equilibrium, the average distance between the two surfaces just after the contact and, then, the work of adhesion can be calculated.

A few moment after the creation of the interface, the water is expected to move (diffuse) along the bonding interface in order to reduce the energy of the entire system. Then, the water coverage at each point of the surface will be a function of the gap height between the two surfaces (Fig. 3c). The work of separation can be calculated, in this case, using as input values the results of the molecular dynamics simulation.

The detail of the model derivation is presented in the following, both in the adhesion case and in the separation case.

2.2.2 The adhesion model

The idea is to compute the average force between the two substrates, as a function of the average gap separation distance z, for a given quantity of water ML_0 and for a given interface roughness standard deviation σ. Because the calculation considers a surface size in the micrometer range, the average force is noted $F_{\mu m}$:

$$F_{\mu m}(z,\, \sigma,\, ML_0) = \int_{-\infty}^{+\infty} G(z' - z)\, f_{nm}(z',\, ML_0)\, dz' \,. \tag{2}$$

Then, mechanical equilibrium corresponds to an average force equal to zero:

$$z_{eq} \quad \text{such that} \quad F_{\mu m}(z_{eq},\, \sigma,\, ML_0) = 0\ . \tag{3}$$

And finally, the work of adhesion W is obtained as the work performed by the microscopic forces when the two surfaces are brought in contact, from an infinite separation distance to the equilibrium distance z_{eq}:

$$W(\sigma,\, ML_0) = -\int_{z_{eq}}^{+\infty} F_{\mu m}(z,\, \sigma,\, ML_0)\, dz\ . \tag{4}$$

The work of adhesion can be, therefore, obtained as a function of the interface roughness σ, and as a function of the amount of water at the interface ML_0. Integration and root finding are performed numerically, using Matlab®, from the interpolated values proposed by D. J. Cole et al. (see Fig. 2a). The results are shown in Fig. 4.

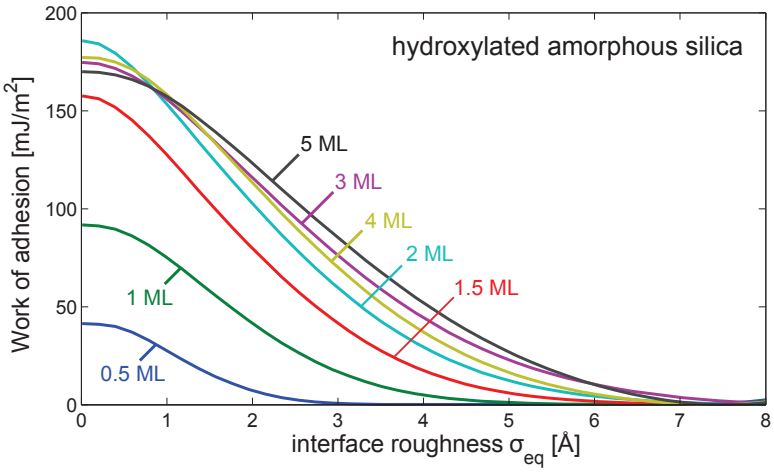

Fig. 4: Theoretical work of adhesion calculated from the molecular dynamics results and by considering the interface roughness σ and the amount of water at the interface ML_0 (these values are twice those given by D. J. Cole et al. because, here, the interface is considered).

2.2.3 The separation model

After the interface is closed, the water is expected to diffuse along the bonding interface in order to reduce the system energy. Therefore, the quantity of water ML_{eq}, at a certain point of the surface, will be a function of the interface gap height at this point, noted z, in such a way that $f_{nm}(z, ML_{eq}) = 0$.

For simplicity, the equilibrium quantity of water ML_{eq} is considered to be a linear function of the gap height: $ML_{eq} = z/t_{water}$, where $t_{water} \approx 3\,\text{Å}$ is the thickness of one water mono-layer. This assumption will be discussed later.

Because the bonding interface is considered as a closed system, the entire amount of

water has to remain constant. Its value is noted ML_0. If not enough water is present to fill the entire interface gap, the equilibrium quantity of water ML_{eq} could not be satisfied for all possible surface locations. Then, two configurations have to be distinguished, depending if there is enough water to entirely fill the interface gap, or not (see Fig. 5).

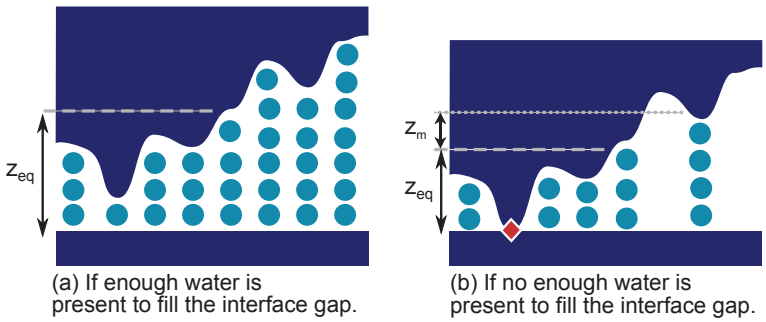

Fig. 5: Schematic representation of the bonding interface after aging. (a) Configuration where the water layer entirely fills the interface gap. (b) Configuration when not enough water is present to fill the entire interface gap. In consequence, "hard" contact occurs at some points of the interface (diamond symbol).

In case of a large quantity of water (Fig. 5a), the average gap separation between the two surfaces z_{eq}, is determined by: $z_{eq}^{(a)} = ML_0\, t_{water}$. Indeed, because the statistical height distribution is symmetric around the average height value, the quantity of water above the mean value is the same as the missing quantity below the mean value.

In this case, the macroscopic work of separation, noted $E_{\mu m}^{(a)}(\sigma,\, ML_0)$, is obtained by averaging the nanoscopic work of separation $E_{nm}(ML_{eq})$ over the interface gap height distribution:

$$E_{\mu m}^{(a)}(\sigma,\, ML_0) = \int_{-\infty}^{+\infty} E_{nm}\left(\frac{z - z_{eq}^{(a)}}{t_{water}}\right) G(z,\sigma)\, dz \tag{5}$$

where the nanoscopic work of separation $E_{nm}(ML)$ is obtained from the molecular dynamics results (see Fig. 2b).

The case of a small quantity of water is more complex, because "hard" contacts are expected to occur between the two surfaces (see Fig. 5b). The "hard" contact corresponds to the configuration where no intermediate water layer is present between the two surfaces, i.e. there is a direct adhesion through hydroxyl groups, or covalent bonds. In this case, the average separation distance between the two surfaces $z_{eq}^{(b)}$ is determined by the interface area in "hard" contact. This issue is related to the rough surface adhesion models, taking into account the elastic deformation of the surfaces (see Section 5 in Chapter I). For simplicity, here, the average separation distance is fixed to $z_{eq}^{(b)} = 3\sigma$, meaning that about 0.13 % of the surface is undergoing a "hard" contact.

Because there is not enough water to fill the entire interface gap, some voids are expected to be present in the large part of the interface gap. It is assumed that the water fills first the small interface gap, until a certain maximum gap height, noted z_m. This hypothesis will be discussed in Subsection 2.3.

Therefore, the maximum height z_m is calculated by solving the equation:

$$z_m \quad \text{such that} \quad ML_0 = \int_{-z_{eq}^{(b)}}^{z_m} \frac{z - z_{eq}^{(b)}}{t_{water}} G(z,\sigma)\, dz \ . \tag{6}$$

The macroscopic work of separation, noted now $E_{\mu m}^{(b)}$, is obtained by averaging the nanoscopic work of separation $E_{nm}(ML)$ over the interface gap height distribution, but now, the integration range is limited by the constant water quantity constraint, i.e. from $-z_{eq}^{(b)}$ to z_m:

$$E_{\mu m}^{(b)}(\sigma,\, ML_0) = \int_{-z_{eq}^{(b)}}^{z_m} E_{nm}\left(\frac{z - z_{eq}^{(b)}}{t_{water}}\right) G(z,\sigma)\, dz \ . \tag{7}$$

Finally, the choice of the case (a) instead of the case (b) is determined by the following condition:

$$ML_0 > \int_{-z_{eq}^{(b)}}^{+\infty} \frac{z - z_{eq}^{(b)}}{t_{water}} G(z,\sigma)\, dz \ . \tag{8}$$

Similar to the adhesion situation, integration and root finding are performed numerically. The results are shown in Fig. 6.

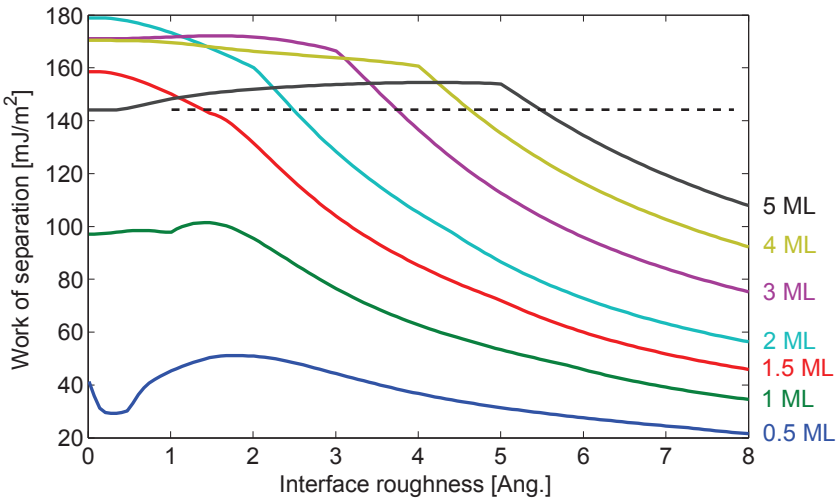

Fig. 6: Variation of the theoretical work of separation values calculated from the molecular dynamics results as a function of the interface roughness for different amount of water at the interface (these values are twice those given by D. J. Cole et al. because, here, the interface is considered). The dashed line indicates twice the surface tension of water.

2.3 | Experimental methods and results

The bonding propagation velocity and bonding interface energy (i.e. the separation case) have been measured for different silicon oxide surface roughness. Experimental methods and results are presented in the followings.

Control of surface roughness. A $1\,\mu m$ thick silicon oxide layer was thermally grown on 200 mm diameter silicon wafers. The oxide layer was then etched by using a diluted hydrofluoric acid solution (HF) in order to roughen the surfaces prepared for bonding. Three types of surfaces have been elaborated: no oxide was removed (Type A), after etching about $150\,nm$ (Type B) and after etching about $600\,nm$ (type C). The surface roughness was measured using a NanoScope DIM3000 AFM from Veeco Metrology, in tapping mode, on a $2{\times}2\,\mu m^2$ scan. The AFM noise is estimated equal to 0.5 Å. Values equal to $\sigma_A \approx 1.0$ Å, $\sigma_B \approx 2.4$ Å and $\sigma_C \approx 3.5$ Å are measured. Therefore, permutations of the surface type allow testing up to six different interface roughnesses (AA, AB, BB, AC, BC, and CC).

Work of adhesion measurements. The work of adhesion W can be roughly estimated from the bonding velocity v using the relationship: $W = \beta\, v^{5/4}$, where β is a constant (see Chapter II and ref. [60]). The value of the constant is estimated equal to $\beta \approx 6.5\times10^{-3}\, J.m^{-3/4}.s^{-5/4}$ according to the bonding velocity and work of adhesion values used in the chapter II ($v_{ii} = 2.4\,cm/s$ and $W_{ii} = 112\,mJ/m^2$). It is worth mentioning that the bonding velocity depends on the bonding configuration and the location on the wafer. For this experiment, the bonding propagation velocity was recorded using an infrared light observation system. The bonding initiation was performed at the wafer edge, and the bonding velocity was taken at the center of the wafer.

Interface energy measurement (separation case). The bonding energy is measured using the common blade insertion method. The opened crack length is measured using infrared light transmission observation and the beam formula is used despite the circular wafer geometry. For this reason a large error value is expected on the bonding interface energy values.

It is worth mentioning that the wafer bonding as well as the interface energy measurements are performed in a clean room environment where the relative humidity is about 40 %.

The measured variations of the work of adhesion values and bonding interface energy values, as a function of the interface roughness, are shown on the Fig. 7.

The work of adhesion is found to decrease with the interface roughness from about $140\,mJ/m^2$ down to $40\,mJ/m^2$. The bonding interface energy values decrease from about $160\,mJ/m^2$ down to $100\,mJ/m^2$.

The work of adhesion appears to be more sensitive to the roughness than the interface energy (separation). According to the proposed model, the water movement along the interface allows compensating the roughness effect by filling the interface gap.

In addition, the model prediction for 1 *ML* and 2.5 *ML* (i.e. 2 and 5 monolayers of water at the interface) are plotted on the both adhesion and separation figures. A relatively good agreement is obtained between the general theoretical predictions and the measurements. Nevertheless, the large uncertainty on the measured values does not allow an accurate verification of the model predictions.

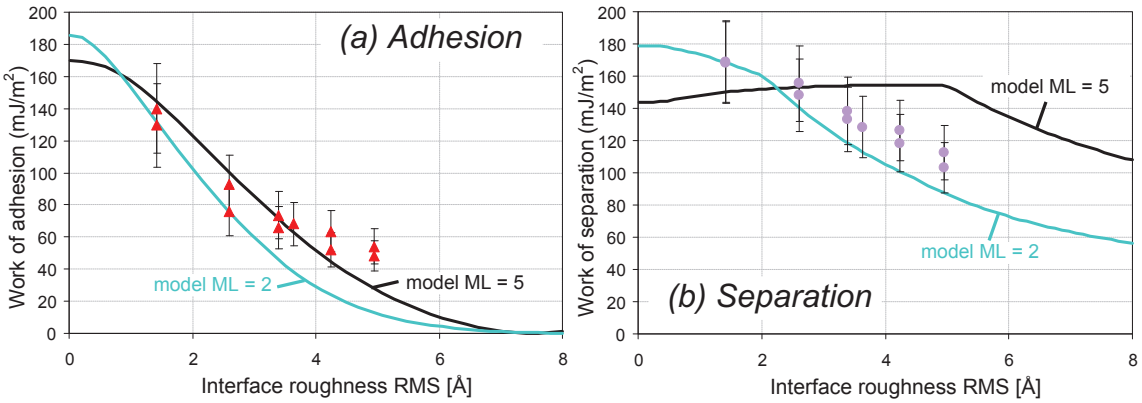

Fig. 7: Theoretical and experimental results about the interface roughness effect on the work of adhesion (a) and the work of separation (b). The solid line are the model predictions for the quantity of water $ML = 2$ and $ML = 5$ at the interface.

2.4 | Discussion and perspectives

In the following, a more detailed discussion about model hypotheses, and future model improvements, are presented.

One of the main assumption of the model is that the characteristic time of the water flow movement along the interface is larger than the characteristic time of the interface bonding. Considering a bonding velocity of $2\,cm/s$, the bonding front needs $0.1\,ms$ to go through the $2\times2\,\mu m^2$ AFM scan area. The self-diffusion coefficient of water is equal to $D_{H_20} \approx 2\times10^{-9}\,m^2.s^{-1}$ at $25°C$ [137]. This value can be considered as a upper bound estimation of the actual diffusion coefficient of water along the bonding interface. The characteristic time of diffusion is $\tau \sim l^2/D_{H_20} \sim 2\,ms$, where $l = 2\,\mu m$. Therefore, it can be assumed that the water diffusion along the interface does not contribute to the work of adhesion, i.e. to the bonding front propagation, while it contributes to the bonding interface toughness, as long as opening occurs some time after the interface bonding contact (between some milliseconds to some seconds).

In the separation model, the quantity of water at equilibrium ML_{eq} is assumed to depend linearly on the gap separation distance. According to the molecular dynamics simulation results, this assumption is valid for more than $1\,ML$ per surfaces (see Fig. 2a). Below this value, the equilibrium separation gap remains almost constant. However, defining the gap separation distance for a small water coverage is not straightforward, since the water molecules, the hydroxyl groups and the last layer of silicon oxide can be all mixed together at around the same height value. In addition, effects of the discrete nature of the water may be possible, i.e. a full layer of water molecules will be more stable even if the height gap is a little higher or lower than the equilibrium.

Considering only the total amount of water may be not sufficient to describe the entire chemical state of the interface. The hydroxyl group density, as their types, could constitute additional input parameters for the model.

Another hypothesis used for the separation model is that the large interface gaps are

free of water molecules. It is not obvious that, even for the large gap, a small quantity of water will not remain adsorbed on hydroxyl groups. In this case, the derivation of the entire quantity of water should be modified. It is worth noting that the extreme case of this situation looks like the capillary adhesion between rough surfaces, where bridges of water form between the two surfaces, leading to existence of liquid/void interfaces.

A small difference between the direct bonding of native silicon oxide surfaces case and the bonding of amorphous silica surface case has been observed by D. J. Cole et al. [38]. This difference is explained by the long range force (van der Waals) between the substrates and the resulting influences on the ordering of the water layers. Here, the case of amorphous silica surface have been presented only, but a similar derivation can be performed in the native oxide silicon case.

Semi-analytical model may be not sufficient to take into account all the complex behaviors of the interface. Hence, building a numerical model based on Monte Carlo methods, combined with additional molecular dynamics simulations may be interesting.

The interface model presented in this chapter can be used as a starting point to build a quantitative model of the interface aging. For instance, the covalent bonds formation effect on the interface energy can be included, by changing the input data of the model (Fig. 2b). Indeed, the surface energy corresponding to zero monolayer of water can be fixed to the surface energy equivalent of covalent bonds. However, since both water molecules and covalent bond will be present at the interface, and that the interface energy measurement involves stress on the interface, the stress corrosion effect has to be taken into account.

In addition, since covalent bonds are created, the elastic deformation of the surfaces should be considered. Two effects are expected: the statistical distribution of the interface gap height and the energetic balance will be affected.

3 | Measurement of the work of adhesion with entire wafers

3.1 | Description of the method

The bonding interface energy is usually measured by inserting a blade in-between the two wafers and by measuring the induced crack length [92]. This method gives an estimate of the separation energy, which, as discussed previously, is different than the work of adhesion [6, 43]. It has been reported that similar test, but where the blade is used to stop the bonding propagation instead of opening the interface, will give access to the work of adhesion value [43, 60].

However, the use of the same blade system during wafer bonding is not appropriate, mainly because the blade is usually thick and the resulting non-bonded area will be too large compared to the entire wafer surface. In addition, the conventional experimental set-up has many drawbacks, such as the inaccuracy of the measured crack length using infrared light observation and the inappropriate use of the formula which is derived in 1D plane geometry while the actual wafer geometry is more complex [138].

D. Pasquariello et al. have proposed to created a circular non-bonded area by introducing a well-defined defect at the bonding interface prior to bonding. The small defect is defined using lithography techniques and the surface of the resulting non-bonded area, measured by infrared light observation, is used to calculate the adhesion surface energy [139]. Recently, a similar method has been used to measure the interface adhesion between a graphene layer deposited on a silicon substrate, using for the defect, a nano-particle placed between the graphene layer and the substrate [140].

Y. Bertholet et al. have suggested to measure the wafer deflection using a mechanical profilometer, instead of using the infrared light observation [141]. Therefore, the accuracy of the crack length measurement and, at the same time, that of the blade thickness value are significantly increased.

Based on these previous reports, a new method has been developed here to accurately measure the work of adhesion. It consists of placing a small particle on the wafer surface in order to locally prevent the bonding propagation and to create a bubble along the bonded interface. The deflection profile of the wafer, around the bubble, is measured using a mechanical profilometer. Therefore, both the bubble height and the lateral size are obtained from the measurement. A mechanical model of the wafer deflection allows extracting the work of adhesion. In order to derive a simple analytically model, the induced bubble should preferably involve a 1D long profile.

In this experiment, a thin strip of polymer material, $\sim 10\,\mu m$ thick, $4\,mm$ width and $70\,mm$ long, is manually placed on top of one wafer surface, along the radius, prior to bonding. The bottom wafer is held at its center only, leading to a spontaneous initiation of the bonding front propagation (see Chapter II, Section 5.2, p. 52). Fig. 8 shows the bonding front propagation for one of the experiments.

It is worth mentioning that this method allows to probe the interface with same

conditions that the actual bonding process and it can be applied to non-transparent substrates, for instance involving metallic layers.

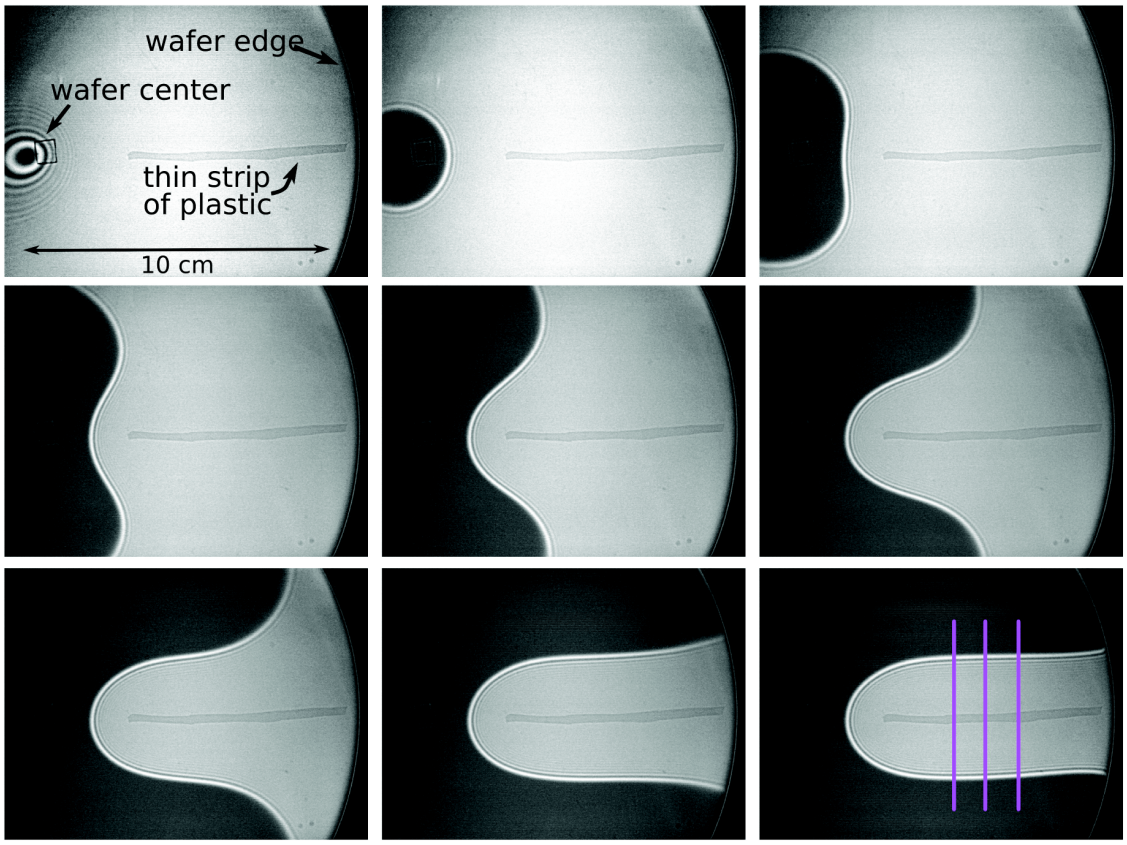

Fig. 8: Infrared observation of the bonding front propagation. Only one half of the wafer is shown. The time delay between each pictures is $1\,s$. The square near the wafer center is the plastic piece use to support the wafers. Interference fringes are visible during the initiation step (picture one). The three vertical (purple) lines indicate where the profile scan measurements have been performed. It should be noted that, here, the bonded area is darker than the non-bonded because of the interferences in the silicon oxide layer ($1\,\mu m$ thick).

3.2 | Formula derivation of bubble profile

A theoretical model of the deflection of both wafers is needed to extract the work of adhesion. The notations are given in the Fig. 9.

The thin plate equation, for the wafer number i, and the appropriate boundary conditions are

$$w_i^{(4)}(x) = 0\,; \quad w_i(0) = w_{i0}\,; \quad w_i(a) = 0 \quad \text{and} \quad w_i'(a) = w_i'(0) = 0 \tag{9}$$

where $w_0 = w_{10} + w_{20}$ is the particle height. The boundary condition at the bubble edge $x = a$ is a built-in edge condition, and the boundary condition at the bubble center $x = 0$ is a fixed position and symmetry.

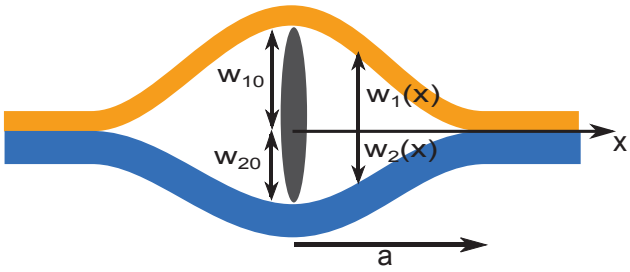

Fig. 9: Cross-section representation of bubble shape. The total particle height is $w_0 = w_{10} + w_{20}$.

The solution of the equation is

$$w_i(x) = w_{i0}\left[1 - 3\left(\frac{x}{a}\right)^2 + 2\left(\frac{x}{a}\right)^3\right] \quad ; \quad x \in [0,\, a] \ . \tag{10}$$

Because the two wafers can be different, the deflection at the bubble center may be different for each wafers, and need to be calculated. The force balance on the particle gives: $D_1\, w_1^{(3)}(0) = D_2\, w_2^{(3)}(0)$. Therefore, using the wafer deflection equation (eq. 10), the equality $D_1\, w_{10} = D_2\, w_{20}$ is obtained. Afterwards, the relationships between the wafers deflection at the center (w_{10} and w_{20}) and the total particle height $w_0 = w_{10} + w_{20}$ is derived as a function of the flexural rigidity D_1 and D_2:

$$w_{10} = \frac{D_2}{D_1 + D_2} w_0 \quad \text{and} \quad w_{20} = \frac{D_1}{D_1 + D_2} w_0 \ . \tag{11}$$

The equilibrium bubble size a is calculated using an energy balance. The elastic strain energy inside the two plates writes

$$U(a) = 2\frac{D_1}{2}\int_0^a w_1''^2\, dx + 2\frac{D_2}{2}\int_0^a w_2''^2\, dx \tag{12}$$

$$= \frac{12}{a^3}\left(D_1\, w_{10}^2 + D_2\, w_{20}^2\right) \tag{13}$$

$$= \frac{12\, w_0^2}{a^3}\frac{D_1\, D_2}{D_1 + D_2} \ . \tag{14}$$

The bubble surface energy can be defined as: $\Gamma(a) = 2a\, W$, where W is the work of adhesion. The equilibrium bubble size a_{eq} corresponds to a minimum of the total energy:

$$\frac{d\Gamma}{da}(a_{eq}) + \frac{dU}{da}(a_{eq}) = 0 \ . \tag{15}$$

Finally, the work of adhesion expression is derived as

$$W = \frac{18\, w_0^2}{a^4}\frac{D_1\, D_2}{D_1 + D_2} \ . \tag{16}$$

3.3 | Measurements and results

The wafer deflection profile, perpendicular to the bubble, is measured using a mechanical profilometer. The bonded wafers are hold by a three points support in such a way that there is no contact between the bubble and the support. The position of the profiles is indicated in the last picture of Fig. 8 and one example of the obtained wafer defection profile is shown in Fig. 10a.

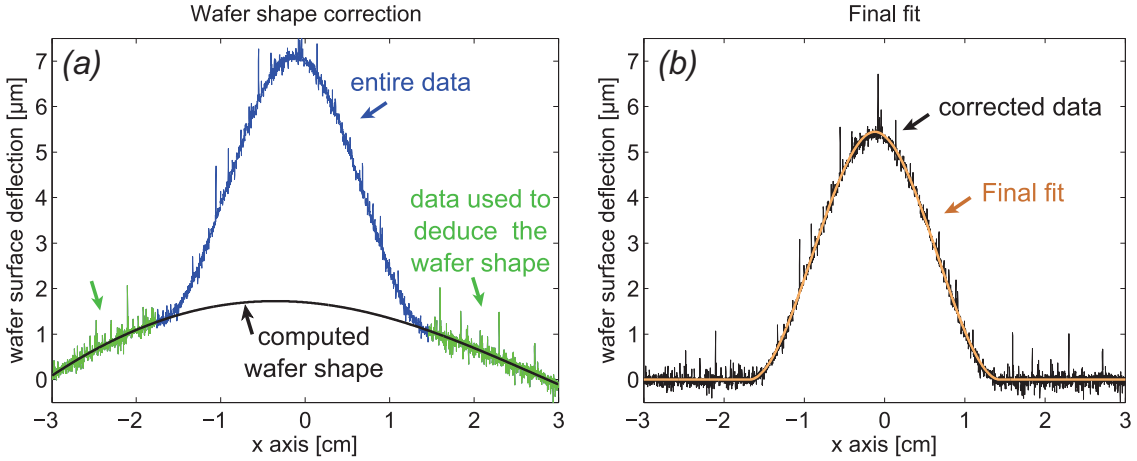

Fig. 10: (a) The wafer deflection obtained with a mechanical profilometer. The external extent of the profile (green line) is used to fit a fourth order polynomial function from which the global wafer shape is derived (black line). (b) The wafer deflection profile after the correction was applied. A non-linear fit is performed using the theoretical bubble shape (eq. 10) (orange line).

The measured wafer deflection profile has to be corrected from the global wafer shape. The global wafer shape comes from both wafers curvature induced by the bonding propagation (see Chapter III) and the gravity action during the profile measurement. It is assumed that the pure bubble deflection can be obtained by subtracting the global wafer shape. The simplest way to know the global shape, is to interpolate the profile under the bubble. A fourth order polynomial function is used to perform the interpolation of the global wafer shape. For this reason, it is important to acquire enough data on both sides of the bubble, during the measurement.

Afterwards, the theoretical bubble profile (eq. 10) is used to fit the corrected experimental profile (see Fig. 10b). Then, the partial bubble height w_{10}, the bubble radius a, and the bubble center position x_0 are obtained. The values, for this example, are

$$w_{10} = 5.55\,\mu m \quad ; \; a = 1.56\,cm \quad ; \; x_0 = -0.26\,cm\,. \tag{17}$$

It is worth noting that such a measurement gives the deflection of one wafer only. The entire bubble height w_0 is deduced using the equation 11.

Using equation 16, a work adhesion equal to $W = 90\,mJ/m^2 \pm 7\,mJ/m^2$ is obtained, for this specific example.

3.4 | Discussion

3.4.1 Error estimate

The error impacting the determination of the work of adhesion (eq. 16) can be evaluated in the following way

$$\frac{\Delta W}{W} = 4\frac{\Delta a}{a} + 3\frac{\Delta t}{t} + 2\frac{\Delta w_0}{w_0} + \frac{\Delta \bar{E}}{\bar{E}} \tag{18}$$

where t is the wafer thickness and $\bar{E}$ is the plane strain modulus. As for the blade insertion test, the most critical parameter is the crack length a. The in-plane measurement accuracy is, actually, determined by the XY motorized stage of the profilometer (the tip is fixed, and the wafer is moving during a profile measurement). The accuracy is estimated to $\pm 20\,\mu m$ for 200 mm range (The minimum increment step is much smaller). Another error on the bubble radius measurement comes from the angle between the perpendicular direction of the bubble and the real scan direction. This error is equal to $(1/cos(\theta) - 1)$, where θ is the misalignment angle. An error smaller than $\pm 0.15\%$ is found for $\pm\,3°$ angle shift. Finally, the error on the radius is estimated equal to $\Delta a/a \approx 1\%$. The error on the particle height is estimated equal to $\pm\,0.05\,\mu m$, i.e. $\pm 1\%$, mainly because of the noise in the recorded data and because it has to be taken two times into account since it is also used during the global wafer shape correction. The error on the wafer thickness is about $\pm 3\,\mu m$, i.e. $\pm 0.3\%$. By summing all the contributions, an error value on the measured work of adhesion is found equal to $\Delta W/W \approx \pm 7\%$.

3.4.2 What if the particle is elastic ?

The particle can be deformed by the wafer action, and hence the mechanical equilibrium will be modified. The derivation of the formula is performed, here, considering a spring of rigidity k and free length w_{free} instead of the rigid particle. The equilibrium bubble height is still noted w_0, but it is now a function of the bubble lateral size a. The elastic energy of the system, which includes now the spring energy, writes

$$U(a) = U_{plate}(a) + U_{spring}(a) \tag{19}$$

$$= \frac{12\,w_0^2(a)}{a^3} D_{eq} + \frac{1}{2} k \big(w_{free} - w_0(a)\big)^2 \tag{20}$$

where $D_{eq} = D_1 D_2/(D_1 + D_2)$. Writing the force balance on the spring leads to the equilibrium bubble height $w_0(a)$ expression:

$$w_0(a) = \frac{k}{k + \frac{12}{a^3} D_{eq}}\, w_{free}\ . \tag{21}$$

Finally, the work of adhesion is obtained considering that the total energy $U(a)$ should be minimum:

$$W = \frac{18\,w_{free}^2}{a^4} D_{eq}\, \frac{a^9\,k^3}{(12\,D_{eq} + a^3\,k)^3}\ . \tag{22}$$

It is the same expression that has been found previously (eq. 16) which is modified by a factor which is a function of the stiffness of the both wafers and of the particle elastic properties. The plastic particle rigidity is estimated equal to $k \sim 8 \times 10^{11}\, N.m^{-2}$, using a Young's modulus for a polymer equal to $2\, GPa$, leading to an error on W less than 0.01% .

3.4.3 Why a punctual particle did not work ?

Our original idea was to used a small square shaped particle, and to derive the mechanical model in the axisymetric case assuming the particle at the center. Fig. 11 shows the infrared pictures of a bonding propagation attempt, where a small square particle is present. Surprisingly, the resulting bubble is not a circle, but looks like an "egg shape". Much more complex phenomena seem to occur when the bubble get closed. A certain amount of air is trapped inside the bubble, leading to a non-bonded surface which is larger than the one the particle alone would have induced. Therefore, its is expected that the particle is not any more in contact with both wafers. In addition, an hysteresis on the surface energy is needed to explain why the bubble is not circular. Indeed, the more energetically favorable state is when the particle is perfectly round. But, because it is more difficult for the bonding front to recede than to advance, the bubble dimension remains smaller on the particle side, which leads to "egg shape". For this reason the "wire" shape particle was finally selected for the measurement of the work of adhesion.

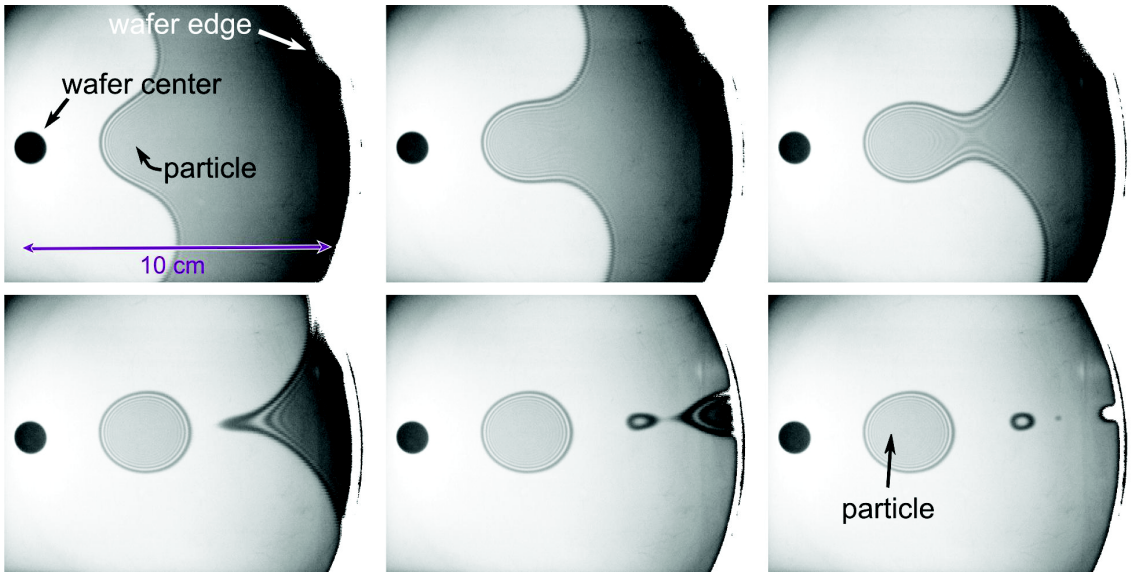

Fig. 11: Observations of the bonding front propagation when a punctual particle is present on the wafer surface. Delay between images is $1\, s$. The final bubble is neither centered around the particle, nor circular.

3.4.4 What if a water meniscus forms at the crack front ?

The humidity of the atmosphere could condense at the bonding front if enough time is allowed, leading to a water meniscus. In this case, the deduced work of adhesion value

should be equal to twice the surface tension of water whatever the value of the surface roughness or the initial amount of water adsorbed on the wafer surfaces.

The same bubble profile has been measured two months after bonding and no difference has been observed. However, the bubble profile measurement was typically performed about 2 hours after the bonding experiments. Additional experiments are needed to verify that no significant modification of the bubble profile occurs shortly after bonding.

4 | Conclusion and perspectives

In this chapter, a model of the bonding interface is proposed, taking into account the interface roughness and the distribution of the quantity of water along the bonding interface. The model is based on previous molecular dynamics simulation results obtained by D. J. Cole et al. The hysteresis effect between the adhesion and the separation of the interface can be explained. The experimental results are coherent with the model predictions. However, because of the uncertainty on the current experimental values, a more accurate validation is probably needed.

In the second part of the chapter, a novel method for accurate measurement of the work of adhesion, in the specific case of direct wafer bonding, has been proposed. The method uses a pre-defined bonding defect to prevent the propagation over a certain area on the wafer. A bubble is then created between the two wafers, and a mechanical profilometer is used to measure both the height and the radius of the bubble. A theoretical mechanical model of the wafer deflection allows the determination the work of adhesion value.

Several perspectives work are suggested. In order to complete the validation of the current interface adhesion model, a more detailed experimental study is needed, including for instance, the study of the impact of the surface roughness, of the surface activation (e.g. plasma treatment) and of the relative humidity of the bonding environment. Moreover, it should be interesting to study the dynamical behavior of the bonding interface, i.e. the water diffusion along the interface, and the covalent bond formation (and therefore the stress corrosion effect).

In relation with the Chapter III, it will be important to study the interface shear toughness. Furthermore, considering two flat and parallel surfaces which get closer, may be not appropriate at a larger scale. Building a coherent description of the bonding front from the scale of the molecular dynamics simulation, to the scale of the plate theory, could be an interesting future work (see for example Fig. 4 in Chapter III, p. 63).

Conclusion and Perspectives

Direct bonding refers to the adhesion between two solid materials without the use of any adhesive inter-layer. This method is commonly used in microelectronic industry to assemble wafers, in particular to transfer a thin layer of material from a donor wafer to a handling wafer. Because a thin air layer remains trapped in between the two wafers when they are brought close to each other, a coupled system is formed, constituted by the thin fluid layer, the mechanical deflection of the wafers, and the strong adhesion forces. A fascinating front propagation phenomenon occurs during the contacting step, leading, in some cases, to a final deformation of the assembled stack, which is detrimental for specific applications.

The present thesis has been focused on the mechanical and dynamical aspects of the direct wafer bonding process, to identify the main physical phenomena, to develop models, and to validate them by experimental results. Three different topics are covered and investigated in the thesis.

A theoretical description of the fluid/structure bonding system is established. The wafer bonding sequence is described as made of four different steps, including the initiation step, allowing a numerical solution strategy, in the transient regime, within a one dimensional framework. An original experimental method has been set up, involving non-contact optical sensors, to measure the vertical movement of the wafer during the bonding. Thanks to the simulation results, validated by the measurements, a comprehensive description of the entire bonding dynamics is obtained.

Arising from the obtained understanding of the bonding dynamics, a new model has been proposed to explain the final curvature of the bonded wafers. During the bonding process, the wafers are significantly deformed in the vicinity of the bonding front, by all the load components acting on the wafers. Wafers are assumed to be, progressively, joined together, while conserving their two different macroscopic curvatures, due to in-thickness elastic deformations of the wafers. Therefore, a strain discontinuity is locked-in at the interface along the bonding front path. In order to test the proposed model, wafers with different thicknesses have been bonded. A specific bonding configuration has been used to control the external load components acting on the wafers during the bonding. A very good agreement between the measured final wafer profile and the model prediction is obtained.

It is worth noting that the models presented in Chapter II and III consider the bonding dynamics from a macroscopic perspective. It comes out that many important phenomena

occur at the vicinity of the bonding front, at micrometer and even nanometer scales. Indeed, both models use experimental parameters: the cut-off length h_c which accounts for the viscous dissipation inside the fluid and the sliding coefficient ϕ which accounts for the shear stress relaxation at the interface. These two coefficients are directly related to the work of adhesion.

For these reasons, a study of the work of adhesion, in case of hydrophilic direct wafer bonding, is performed in Chapter IV. A theoretical description of the bonded interface, at the micrometer scale, has been derived, considering the interface roughness, the amount of water adsorbed on the wafer surfaces and the force-distance function previously computed by D. J. Cole et al. using molecular dynamics simulation. An explanation of the interface hysteresis, i.e. the higher value for the work of separation than for the work of adhesion, is proposed, considering the water movement along the interface, few seconds after the bonding, driven by the inhomogeneity of the interface gap height.

In addition, a new method to accurately measure the work of adhesion is proposed. A defect is intentionally generated on the surface of one wafer prior to bonding, in such a way that an elongated bubble is created between the two bonded wafers. The value of the work of adhesion is calculated from the measurement of the deflection profile of the wafers feeding a simple mechanical model.

Based on the results presented in the thesis, many new questions and interesting future works emerge. The perspectives mentioned at the end of the chapters, can be summarized as following. The first perspective concerns the understanding of the phenomena occurring at the bonding front at the micrometer and nanometer scale. The second one is about extending and applying the current macroscopic models to more complex situations, related to actual issues encountered in industrial applications.

At the nanometer scale, molecular dynamics simulation of the bonding interface could be performed, on the one hand, to refine the microscopic model of the interface, and, on the other hand, to test the ability of the interface to slide under shear stress. At the micrometer scale, it would be interesting to extend the coupled fluid/structure model, using, for instance, the analogy with a crack in an infinite medium. Then, both the viscous dissipation during the propagation, and how the elastic strain is transferred to the bonding interface, should be studied. Experimental studies are quite challenging since direct observation will be difficult. However, the improvement of the experimental methods presented here, could allows probing the behavior of the bonding front.

Additional work is needed to extend the current models to complex bonding problems. Bonding dynamics could be significantly modified in the case of very large wafers (e.g. $450\,mm$ diameter wafer is forecast), or in the case of very thin, flexible, wafer. A challenging issue is to design a more robust numerical solver, which can also compute the equations of the bonding process dynamics expressed in two dimensions. Propagation of the bonding front around small particles, and over patterned structures will be an interesting extension,

with many important industrial applications. Another work will concern the extension of the current model of the wafer deformation to the two dimensional case, by considering the actual bonding front shape.

Appendices

A | The rarefaction gas model

The molecular mean free path varies as the inverse of the gas pressure. It is obtained from the following equation : $\lambda = \frac{k_B T}{\pi\sqrt{2}d^2 P}$ where T is the temperature (in Kelvin), k_b is the Boltzmann constant, P is the gas absolute pressure (in Pascal) and d is the diameter of the gas particles (an average value of $0.3\,nm$ is used for air).

For Knudsen number, Kn, between 0.01 and 0.1, the slip flow model can be used. In this regime, a coefficient, $\widehat{Q}$, is inserted in the Reynolds equation [128]:

$$\frac{dh}{dt} = \mu \mathrm{div}\Big(h^3\, \widehat{Q}\, grad\, P \Big) \tag{1}$$

$\widehat{Q}$ is an normalized flow rate dependent of Kn by the relation :

$$\widehat{Q} = 1 + 6\alpha Kn + 12\epsilon Kn^2 \tag{2}$$

with the constants coefficients $\alpha = 1.11$ and $\epsilon = 0.31$. Notations are similar of those used in ref. [128], even though the transformation is used $\widehat{Q} = Kn.\overline{Q}$.

B | Boundary condition for adhesion

Here, the derivation of the formula used for the plate boundary condition for adhesion (page 37 Chapter II) and used for the moment due to the fluid M_{fluid} (page 66, Chapter III) is detailed. In addition, the assumption made to neglect the gravity action and the remaining strain energy is discussed.

One wafer case. The simplest case is considered first, see Fig. 1a. The wafer is assumed initially flat, and in adhesion with a flat and rigid support. No elastic deformation is assumed to remain in the bonded part of the wafer and the geometry is assumed plane. The energy balance is written when the bonding front advances by a small distance da, i.e. the variation of internal energy is equal to the work done by the external forces and moments. The energy variation and the work done by the moment M_1 write

$$\Delta E = -\frac{M_1^2}{2D}\, da - W\, da \quad ; \quad T = M_1\, \Delta\theta = -\frac{M_1^2}{D}\, da\ . \tag{3}$$

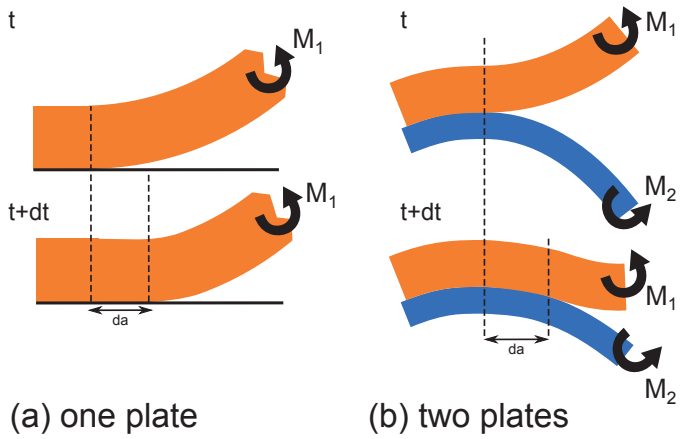

Fig. 1: Schematic illustration of the plate near the bonding front when one wafer is considered only (a) and when the two wafers are considered (b).

where $\Delta\theta$ is the variation of the slope of the plate. Then, the relation $\Delta E = T$ leads to writes

$$W = \frac{M_1^2}{2D} = \frac{D}{2}\,k^2 \tag{4}$$

The work done by the external forces is a second order quantity (da^2).

Similar result has been previously obtained, see ref. [124–126]. However, the bending elastic energy is not considered in ref. [124] leading to a factor 2 in the formula.

Two wafers case. The similar derivation can be performed when two plates are considered and when an elastic strain energy remains in the bonded part of the plates, see Fig. 1b. After the bonding, the bilayer plate is still deformed by the moment $M_1 + M_2$ and a remaining strain energy E_R is locked in the plate due to the strain discontinuity $\Delta\epsilon$ (see Chapter III and Appendix C). Hence, the energy variation writes, in this case

$$\Delta E = \frac{(M_1+M_2)^2}{2D_{12}}\,da + E_R\,da - \frac{M_1^2}{2D_1}\,da - \frac{M_2^2}{2D_2}\,da - W\,da \tag{5}$$

The work done by both moments writes

$$T = M_1\left(k_{12} - \frac{M_1}{D_1}\right)da + M_2\left(k_{12} - \frac{M_2}{D_2}\right)da \tag{6}$$

where $k_{12} = k_f + (M_1+M_2)/D_{12}$ is the curvature of the bilayer plate. Hence, the following equation is obtained

$$W = \frac{(M_1+M_2)^2}{2D_{12}} + E_R - \frac{M_1^2}{2D_1} - \frac{M_2^2}{2D_2} - M_1\left(k_{12} - \frac{M_1}{D_1}\right) - M_2\left(k_{12} - \frac{M_2}{D_2}\right) \tag{7}$$

Both E_R and k_{12} can be written in terms of $\Delta\epsilon$, M_1 and M_2:

$$W = \frac{M_1^2}{2D_1} + \frac{M_2^2}{2D_2} - \frac{(M_1+M_2)^2}{2D_{12}} + \frac{2\Delta\epsilon}{t_1+t_2}\left(1 - \frac{D_1+D_2}{D_{12}}\right)\left[\frac{D_1+D_2}{t_1+t_2}\Delta\epsilon - M_1 - M_2\right] \tag{8}$$

The two unknowns for this equation are M_{fluid}, included in the loads M_1 and M_2, and the strain discontinuity $\Delta\epsilon$. Therefore, by using the relation between $\Delta\epsilon$ and the loads M_1 and M_2 given by the geometric constraint on $\Delta\epsilon$ (eq. 16, page 65), a system of two equations and two unknowns is obtained. This system can be solved to obtain M_{fluid} and $\Delta\epsilon$ as a function of the gravity action M_{g1} and M_{g2}, the work of adhesion W and the sliding coefficient ϕ.

In case of vertical bonding. If the effect of fluid is considered only, i.e. $M_1 = -M_2 = M_{fluid}$, the above equation simplifies to:

$$W = \frac{M_{fluid}^2}{2}\left(\frac{1}{D_1}+\frac{1}{D_2}\right) + 2\Delta\epsilon^2\left(1-\frac{D_1+D_2}{D_{12}}\right)\frac{D_1+D_2}{(t_1+t_2)^2} \tag{9}$$

And the "geometric" equation simplifies to

$$\Delta\epsilon = (1-\phi)\frac{M_{fluid}}{2}\left(\frac{t_1}{D_1}-\frac{t_2}{D_2}\right) \tag{10}$$

Finally, an expression for M_{fluid} is obtained in terms of W only:

$$M_{fluid} = \sqrt{2W}\left[\frac{1}{D_1}+\frac{1}{D_2}+(1-\phi)^2\left(\frac{t_1}{D_1}-\frac{t_2}{D_2}\right)^2\left(1-\frac{D_1+D_2}{D_{12}}\right)\frac{D_1+D_2}{(t_1+t_2)^2}\right]^{-\frac{1}{2}} \tag{11}$$

The left part of this equation correspond to the one used in Chapter III (eq. 20, page 66). Hence, contribution of the remaining curvature on the energy balance can be evaluated. The error on M_{fluid} is about 4.5% only, considering $\phi = 0$, and $t_1 = 500\,\mu m$ and $t_2 = 717\,\mu m$.

C | Graphical demonstration of final wafer curvature

Another demonstration of the relation between the strain discontinuity $\Delta\epsilon$ and the final curvature k_f (eq. 11, p. 63) is presented here. The idea is to consider that, the two wafers are joined together both deformed at the same virtual curvature $k^\star$. Then, the strain discontinuity at the interface writes :

$$\Delta\epsilon = \frac{t_1+t_2}{2}\,k^\star \quad . \tag{12}$$

The two wafers are deformed by applying on them, respectively, the moments M_1 and M_2. The two separated wafers can be seen as an unique plate which have the equivalent rigidity $D_{eq} = D_1 + D_2$. Indeed, the following linear relation can be written: $M_1 + M_2 = (D_1 + D_2)\,k^\star$.

The two stacked wafers are, actually, a plate of thickness $t_{12} = t_1 + t_2$ and of rigidity D_{12} (the interface is not sliding). The bonded plate has a residual curvature k_f. The corresponding plate equation is: $M = D_{12}\,(k - k_f)$. The both wafers are joined together

at the curvature $k = k^\star$, by applying the moment $M = M_1 + M_2$. Then, the two plates equations lead to (see Fig. 2):

$$k_f = \left(1 - \frac{D_1 + D_2}{D_{12}}\right) k^\star \tag{13}$$

Finally, the strain discontinuity $\Delta\epsilon$ (eq. 12) is used instead of the virtual curvature:

$$k_f = \frac{2\Delta\epsilon}{t_1 + t_2}\left(1 - \frac{D_1 + D_2}{D_{12}}\right) \tag{14}$$

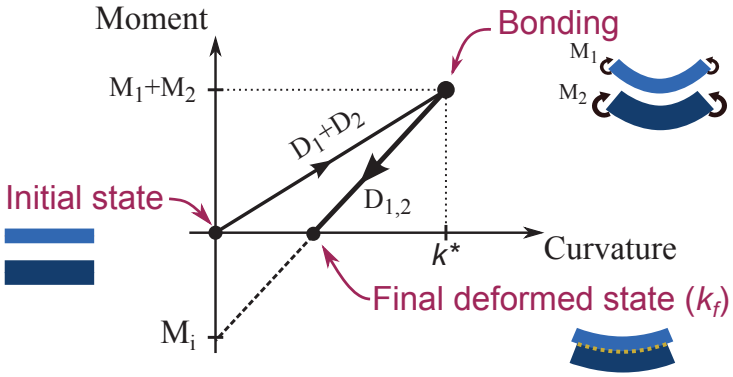

Fig. 2: Schematic illustration of the mathematical derivation. $k^\star$ is used as a virtual bonding curvature.

Remaining strain energy. The elastic strain energy which remains locked in the stack corresponds to the area of the triangle formed by the bold lines on Fig. 2. It writes

$$E_R = \frac{D_1 + D_2}{2} k^{\star 2} - \frac{D_{12}}{2}(k^\star - k_f)^2 \tag{15}$$

$$= \frac{D_1 + D_2}{2}\left(1 - \frac{D_1 + D_2}{D_{12}}\right)\left(\frac{2\Delta\epsilon}{t_1 + t_2}\right)^2 \tag{16}$$

Initially curved wafers. The same idea can be used to solved the problem when both wafers are initially curved (at the curvatures k_{01} and k_{02}). Then the first plate equation, before the bonding, writes :

$$M_1 + M_2 = (k^\star - k_{0eq})(D_1 + D_2) \;\; with \quad k_{0eq} = \frac{k_{01}D_1 + k_{02}D_2}{D_1 + D_2} \quad , \tag{17}$$

where k_{0eq} is like an equivalent initial curvature. The bonded plate equation remains the same. Then, the final curvature writes:

$$k_f = \left(1 - \frac{D_1 + D_2}{D_{12}}\right) k^\star + \frac{D_1 + D_2}{D_{12}} k_{0eq} \tag{18}$$

which leads to:

$$k_f = \frac{2\Delta\epsilon}{t_1 + t_2}\left(1 - \frac{D_1 + D_2}{D_{12}}\right) + \frac{k_{01}D_1 + k_{02}D_2}{D_{12}} \tag{19}$$

Starting from this point, more work is needed in order to obtain the full deformation model in the initially warped wafers case.

D | Light reflection of bonded SOI wafers.

How various can be the color of the silicon-on-insulator wafers is fascinating. SOI wafers consist of a thin single crystalline silicon layer lying on a thin amorphous silica layer, which lies, itself, on a thick silicon material. The visible color of the stack is then a function of the thickness of each layer and of the optical properties of the materials (index of refraction and extinction coefficient).

The reflection coefficient can be calculated using the transfer matrix method [142]. Here, the equations are given is the case where the incidence direction is normal to the surfaces ($\phi = 0$).

For each interfaces ($i \to j$), and for each layer (i) the corresponding matrix is computed:

$$I_{ij} = \frac{1}{t_{ij}} \begin{bmatrix} 1 & r_{ij} \\ r_{ij} & 1 \end{bmatrix} \quad ; \quad L_i = \begin{bmatrix} \exp(-\iota\beta_j) & 0 \\ 0 & \exp \iota\beta_j \end{bmatrix} \quad ; \quad \beta_i = \frac{2\pi d_i N}{\lambda} \tag{20}$$

where d_i is the thickness of the layer number i, N is the complex index of refraction $N = n + \iota k$, and ι is the imaginary number unit. The reflection and transmission coefficients are:

$$r_{ij} = \frac{N_j - N_i}{N_i + N_j} \quad ; \quad t_{ij} = \frac{2\,N_i}{N_i + N_j} \tag{21}$$

Then, the scattering matrix S of the entire system writes: $S = I_{01}\,L_1\,I_{12}\,L_2\,I_{23}$, where the layer 0 is air, layer 1 is silicon, layer 2 is silicon oxide and layer 3 is the bulk silicon. The global reflectance coefficient R is calculated from the matrix S:

$$R(d_1,\, d_2) = \left| \frac{S_{21}}{S_{11}} \right|^2 \tag{22}$$

Then, the reflection coefficient of the stack is computed as a function of the incident light wavelength λ, using the known values of refractive index $n(\lambda)$ and extinction coefficient $k(\lambda)$, for silicon and silicon oxide. The reflected spectrum corresponding to an incident white light, assumed to be simply constant, for each top silicon layer thickness d_1 and each oxide layer thickness d_2, is computed.

The next part of the derivation involves the vision of the colors by the human eye. The reflected spectrum has to be break down on the red, green and blue components of the color (RGB). How each wavelength contributes to each color component is given by the three color matching functions[1]. Subsequently, a transformation has to be performed in order to shift between color spaces (XYZ to RGB). Here, the following matrix is used, and

[1] http://www.cvrl.org/cmfs.htm

the colors outside the RGB space are truncated[2]:

$$RGB = \begin{bmatrix} 2.3706743 & -0.9000405 & -0.4706338 \\ -0.5138850 & 1.4253036 & 0.0885814 \\ 0.0052982 & -0.0146949 & 1.0093968 \end{bmatrix} \times xyz \quad ; \quad xyz = \frac{XYZ}{X+Y+Z} \tag{23}$$

The obtained color map of the SOI is shown Fig. 3. The whole variety of colors of the SOI is retrieved, from green to purple, corresponding to the actual color of SOI (some examples is given Fig. 4). However, more work is needed to properly calibrate the printer or the screen, and to improve the color space transformation.

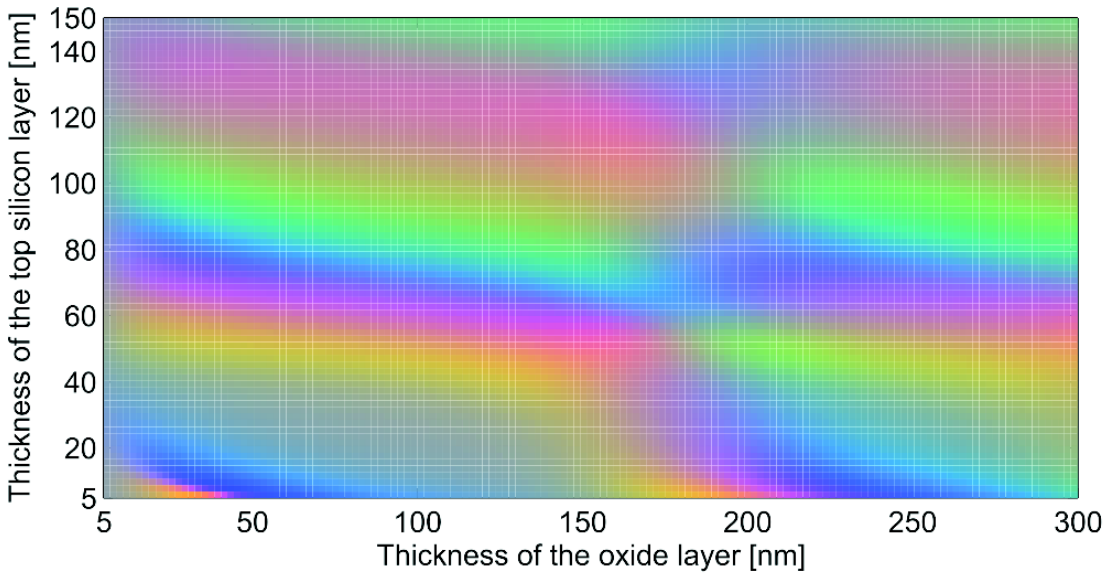

Fig. 3: Color map of the silicon-on-insulator wafer.

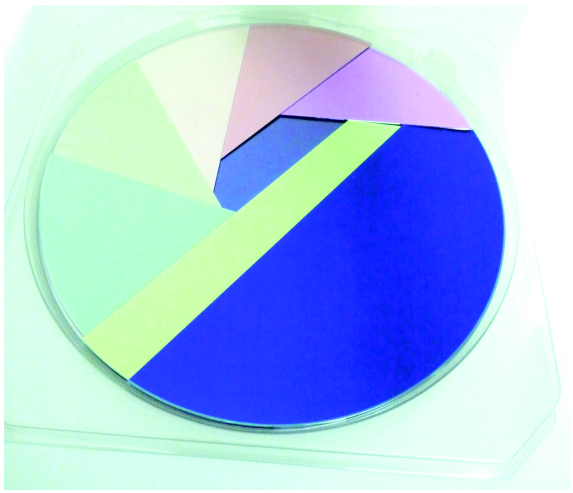

Fig. 4: Picture showing an example of eight variations of thicknesses in the silicon-on-insulator stack, leading to different colors.

[2]see for example: http://mintaka.sdsu.edu/GF/explain/optics/rendering.html

Bibliography

[1] Q.-Y. Tong and U. Gösele, *Semiconductor wafer bonding: Science and technology*. John Wiley (New York), 1999. (cited on pages 15, 18, 19, 21, 23, 25, 26, 39, 44 and 45)

[2] M. Alexe and U. Gösele, *Wafer bonding: applications and technology*. Springer, 2004, vol. 75. (cited on page 16)

[3] A. Plößl and G. Kräuter, "Wafer direct bonding : tailoring adhesion between brittle materials," *Materials Science and Engineering*, vol. 25, pp. 1–88, 1999. (cited on page 15)

[4] J. Haisma and G. A. C. M. Spierings, "Contact bonding , including direct-bonding in a historical and recent context of materials science and technology , physics and chemistry Historical review in a broader scope and comparative outlook," *Materials Science and Engineering R*, vol. 37, pp. 1–60, 2002. (cited on page 15)

[5] J. Obreimoff, "The splitting strength of mica," *Proceedings of the Royal Society of London. Series A, Containing Papers of a Mathematical and Physical Character*, vol. 127, no. 805, pp. 290–297, 1930. (cited on page 15)

[6] L. Rayleigh, "A study of glass surfaces in optical contact," *Proceedings of the Royal Society of London. Series A-Mathematical and Physical Sciences*, vol. 156, no. 888, pp. 326–349, 1936. (cited on pages 15, 20 and 87)

[7] M. Shimbo, K. Furukawa, K. Fukuda, and K. Tanzawa, "Silicon-to-silicon direct bonding method," *Journal of Applied Physics*, vol. 60, no. 8, pp. 2987–2989, 1986. (cited on page 15)

[8] J. B. Lasky, "Wafer bonding for silicon-on-insulator technologies," *Applied Physics Letters*, vol. 48, no. 1, pp. 78–80, 1986. (cited on pages 15 and 16)

[9] M. Bruel, "Process for the production of thin semiconductor material films," Patent, Dec. 20, 1994, uS Patent 5,374,564. (cited on page 16)

[10] M. Bruel, "Silicon on insulator material technology," *Electronics letters*, vol. 31, no. 14, pp. 1201–1202, 1995. (cited on page 16)

[11] T. Yonehara, K. Sakaguchi, and N. Sato, "Epitaxial layer transfer by bond and etch back of porous si," *Applied Physics Letters*, vol. 64, no. 16, pp. 2108–2110, 1994. (cited on page 16)

[12] J. Bagdahn, H. Knoll, M. Wiemer, and M. Petzold, "A new approach for handling and transferring of thin semiconductor materials," *Microsystem Technologies*, vol. 9, no. 3, pp. 204–209, 2003. (cited on pages 16 and 26)

[13] K. Tanabe, D. J. Aiken, M. W. Wanlass, A. F. i Morral, and H. A. Atwater, "Lattice-Mismatched Monolithic GaAs/InGaAs Two-Junction Solar Cells by Direct Wafer Bonding," in *Photovoltaic Energy Conversion, Conference Record of the 2006 IEEE 4th World Conference on*, vol. 1, 2006, pp. 768–771. (cited on page 16)

[14] F. Dimroth, M. Grave, P. Beutel, U. Fiedeler, C. Karcher, T. N. D. Tibbits, E. Oliva, G. Siefer, M. Schachtner, A. Wekkeli, A. W. Bett, R. Krause, M. Piccin, N. Blanc, C. Drazek, E. Guiot, B. Ghyselen, T. Salvetat, A. Tauzin, T. Signamarcheix, A. Dobrich, T. Hannappel, and K. Schwarzburg, "Wafer bonded four-junction GaInP/GaAs//GaInAsP/GaInAs concentrator solar cells with 44.7% efficiency," *Progress in Photovoltaics: Research and Applications*, 2014. (cited on page 16)

[15] J. Prima, F. Roy, H. Leininger, C. Cowache, J. Vaillant, L. Pinzelli, D. Benoit, N. Moussy, and B. Giffard, "Improved colour separation for a backside illuminated image sensor with 1.4 μm pixel pitch," in *Proc. of 2009 International Image Sensor Workshop, paper*, vol. 4, 2009, pp. 22–28. (cited on page 16)

[16] J. A. Burns, B. F. Aull, C. K. Chen, C.-L. Chen, C. L. Keast, J. M. Knecht, V. Suntharalingam, K. Warner, P. W. Wyatt, and D.-R. Yost, "A wafer-scale 3-d circuit integration technology," *Electron Devices, IEEE Transactions on*, vol. 53, no. 10, pp. 2507–2516, 2006. (cited on pages 16 and 17)

[17] S. J. Koester, A. M. Young, R. R. Yu, S. Purushothaman, K.-N. Chen, D. C. J. La Tulipe, N. Rana, L. Shi, M. Wordeman, and E. J. Sprogis, "Wafer-level 3D integration technology," *IBM Journal of Research and Development*, vol. 52, no. 6, pp. 583–597, 2008. (cited on page 16)

[18] C. S. Tan, R. J. Gutmann, and L. R. Reif, *Wafer level 3-D ICs process technology*. Springer, 2008. (cited on page 16)

[19] L. Parameswaran, C. Hsu, and M. A. Schmidt, "A merged mems-cmos process using silicon wafer bonding," in *Electron Devices Meeting, 1995., International*. IEEE, 1995, pp. 613–616. (cited on page 17)

[20] M. A. Schmidt, "Silicon wafer bonding for micromechanical devices," in *Solid-State Sensor and Actuator Workshop*, vol. 6, 1994, pp. 127–131. (cited on page 17)

[21] M. A. Schmidt, "Wafer-to-wafer bonding for microstructure formation," *Proceedings of the IEEE*, vol. 86, no. 8, pp. 1575–1585, 1998. (cited on page 17)

[22] A. London, A. Ayon, A. Epstein, S. Spearing, T. Harrison, Y. Peles, and J. Kerrebrock, "Microfabrication of a high pressure bipropellant rocket engine," *Sensors and Actuators A: Physical*, vol. 92, no. 1, pp. 351–357, 2001. (cited on page 17)

[23] A. Mehra, X. Zhang, A. A. Ayón, I. A. Waitz, M. A. Schmidt, and C. M. Spadaccini, "A six-wafer combustion system for a silicon micro gas turbine engine," *Microelectromechanical Systems, Journal of*, vol. 9, no. 4, pp. 517–527, 2000. (cited on page 17)

[24] M. Nielsen, R. Feidenhans'l, P. Howes, J. Vedde, K. Rasmussen, M. Benamara, and F. Grey, "The interface structure in directly bonded silicon crystals studied by synchrotron x-ray diffraction," *Surface Science*, vol. 442, no. 1, pp. L989 – L994, 1999. (cited on page 17)

[25] F. Fournel, H. Moriceau, N. Magnea, J. Eymery, J. Rouviere, K. Rousseau, and B. Aspar, "Ultra thin silicon films directly bonded onto silicon wafers," *Materials Science and Engineering: B*, vol. 73, no. 1, pp. 42–46, 2000. (cited on page 17)

[26] F. Fournel, H. Moriceau, N. Magnea, J. Eymery, D. Buttard, J. Rouvière, K. Rousseau, and B. Aspar, "Nanometric patterning with ultrathin twist bonded silicon wafers," *Thin Solid Films*, vol. 380, no. 1, pp. 10–14, 2000. (cited on page 17)

[27] K. Autumn, M. Sitti, Y. A. Liang, A. M. Peattie, W. R. Hansen, S. Sponberg, T. W. Kenny, R. Fearing, J. N. Israelachvili, and R. J. Full, "Evidence for van der waals adhesion in gecko setae," *Proceedings of the National Academy of Sciences*, vol. 99, no. 19, pp. 12 252–12 256, 2002. (cited on pages 17 and 18)

[28] W. Sun, P. Neuzil, T. S. Kustandi, S. Oh, and V. D. Samper, "The nature of the gecko lizard adhesive force," *Biophysical journal*, vol. 89, no. 2, pp. L14–L17, 2005. (cited on page 17)

[29] T. Martin, Z. S. Derewenda *et al.*, "The name is bond-h bond," *nature structural biology*, vol. 6, no. 5, pp. 403–406, 1999. (cited on page 18)

[30] J. N. Israelachvili, *Intermolecular and surface forces: revised third edition*. Academic press, 2011. (cited on pages 18 and 19)

[31] R. K. Iler, *The Chemistry of Silica: Solubility, Polymerization, Colloid and Surface Properties, and Biochemistry*, Wiley-Interscience ed., New york, 1979. (cited on page 19)

[32] L. T. Zhuravlev, "The surface chemistry of amorphous silica. Zhuravlev model," *Colloids and Surfaces*, vol. 173, pp. 1 – 38, 2000. (cited on page 19)

[33] R. N. Lamb and D. N. Furlong, "Controlled wettability of quartz surfaces," *J. Chem. Soc., Faraday Trans. 1*, vol. 78, pp. 61–73, 1982. (cited on page 19)

[34] R. R. Thomas, F. B. Kaufman, J. T. Kirleis, and R. A. Belsky, "Wettability of polished silicon oxide surfaces," *Journal of The Electrochemical Society*, vol. 143, no. 2, pp. 643–648, 1996. (cited on page 19)

[35] J. W. Whalen and K.-Y. Lai, "Adhesional wetting on modified soda-lime glass surfaces," *Journal of Colloid and Interface Science*, vol. 59, no. 3, pp. 483–489, 1977. (cited on page 19)

[36] D. Timpel, M. Schaible, and K. Scheerschmidt, "Molecular dynamics studies of silica wafer bonding," *Journal of applied physics*, vol. 85, no. 5, pp. 2627–2635, 1999. (cited on pages 19, 26 and 77)

[37] D. A. Litton and S. H. Garofalini, "Modeling of hydrophilic wafer bonding by molecular dynamics simulations," *Journal of Applied Physics*, vol. 89, no. 11, pp. 6013–6023, 2001. (cited on pages 19, 26 and 77)

[38] D. J. Cole, M. C. Payne, G. Csányi, S. M. Spearing, and L. C. Ciacchi, "Development of a classical force field for the oxidized Si surface: Application to hydrophilic wafer bonding," *The Journal of chemical physics*, vol. 127, p. 204704, 2007. (cited on pages 19, 26, 77, 78, 79 and 86)

[39] S. Leroch and M. Wendland, "Simulation of forces between humid amorphous silica surfaces: A comparison of empirical atomistic force fields," *The Journal of Physical Chemistry C*, vol. 116, no. 50, pp. 26 247–26 261, 2012. (cited on pages 19, 20 and 77)

[40] D. B. Asay and S. H. Kim, "Effects of adsorbed water layer structure on adhesion force of silicon oxide nanoasperity contact in humid ambient," *The Journal of Chemical Physics*, vol. 124, no. 17, 2006. (cited on pages 19 and 21)

[41] K. Jinesh and J. Frenken, "Experimental evidence for ice formation at room temperature," *Physical review letters*, vol. 101, no. 3, p. 036101, 2008. (cited on page 19)

[42] K. Jinesh and J. Frenken, "Capillary condensation in atomic scale friction: how water acts like a glue," *Physical review letters*, vol. 96, no. 16, p. 166103, 2006. (cited on page 19)

[43] D. S. Grierson and K. T. Turner, "Characterization of Hysteresis of Surface Energy in Room-Temperature Direct Bonding Processes," in *ECS Transactions*, vol. 33, no. 4, 2010, pp. 573–580. (cited on pages 20, 39 and 87)

[44] K. T. Turner and S. M. Spearing, "Mechanics of direct wafer bonding," *Proceedings of the Royal Society A: Mathematical, Physical and Engineering Science*, vol. 462, no. 2065, pp. 171–188, 2006. (cited on page 20)

[45] R. Maboudian and R. T. Howe, "Critical review: adhesion in surface micromechanical structures," *Journal of Vacuum Science & Technology B: Microelectronics and Nanometer Structures*, vol. 15, no. 1, pp. 1–20, 1997. (cited on page 21)

[46] C. Mastrangelo, "Adhesion-related failure mechanisms in micromechanical devices," *Tribology Letters*, vol. 3, no. 3, pp. 223–238, 1997. (cited on page 21)

[47] C. Mastrangelo and C. Hsu, "Mechanical stability and adhesion of microstructures under capillary forces. i. basic theory and ii. experiments." *Microelectromechanical Systems, Journal of*, vol. 2, no. 1, pp. 33–55, 1993. (cited on page 21)

[48] F. W. DelRio, M. P. de Boer, J. A. Knapp, E. D. Reedy, P. J. Clews, and M. L. Dunn, "The role of van der waals forces in adhesion of micromachined surfaces," *Nature materials*, vol. 4, no. 8, pp. 629–634, 2005. (cited on page 21)

[49] M. De Boer and T. Michalske, "Accurate method for determining adhesion of cantilever beams," *Journal of applied physics*, vol. 86, no. 2, pp. 817–827, 1999. (cited on page 21)

[50] L. Bocquet, E. Charlaix, S. Ciliberto, and J. Crassous, "Moisture-induced ageing in granular media and the kinetics of capillary condensation," *Nature*, vol. 396, no. 6713, pp. 735–737, 1998. (cited on page 21)

[51] M. de Boer and P. de Boer, "Thermodynamics of capillary adhesion between rough surfaces," *Journal of Colloid and Interface Science*, vol. 311, no. 1, pp. 171–185, 2007. (cited on page 21)

[52] T. C. Halsey and A. J. Levine, "How sandcastles fall," *Physical Review Letters*, vol. 80, no. 14, p. 3141, 1998. (cited on page 21)

[53] Z. Liau, "Semiconductor wafer bonding via liquid capillarity," *Applied Physics Letters*, vol. 77, no. 5, pp. 651–653, 2000. (cited on page 21)

[54] B. Cappella and G. Dietler, "Force-distance curves by atomic force microscopy," *Surface Science Reports*, vol. 34, no. 1, pp. 1–104, 1999. (cited on page 21)

[55] J. Yu, L. Chen, L. Qian, D. Song, and Y. Cai, "Investigation of humidity-dependent nanotribology behaviors of Si (100)/SiO2 pair moving from stick to slip," *Applied Surface Science*, 2012. (cited on page 21)

[56] S. Bengtsson, K. Ljungberg, and J. Vedde, "The influence of wafer dimensions on the contact wave velocity in silicon wafer bonding," *Applied physics letters*, vol. 69, no. 22, pp. 3381–3383, 1996. (cited on page 21)

[57] U. Gösele, S. Hopfe, S. Li, S. Mack, T. Martini, M. Reiche, E. Schmidt, H. Stenzel, and Q.-Y. Tong, "What determines the lateral bonding speed in silicon wafer bonding?" *Applied physics letters*, vol. 67, no. 6, pp. 863–865, 1995. (cited on page 21)

[58] G. Spierings, J. Haisma, and T. Michelsen, "Surface-related phenomena in the direct bonding of silicon and fused-silica wafer pairs," *Philips Journal of Research*, vol. 49, no. 1, pp. 47–63, 1995. (cited on pages 21 and 25)

[59] R. Stengl, T. Tan, and U. Gösele, "A model for the silicon wafer bonding process," *Japanese Journal of Applied Physics*, vol. 28, no. part 1, pp. 1735–1741, 1989. (cited on pages 21 and 25)

[60] F. Rieutord, B. Bataillou, and H. Moriceau, "Dynamics of a bonding front," *Physical Review Letters*, vol. 94, no. 23, Jun. 2005. (cited on pages 21, 35, 38, 39, 40, 84 and 87)

[61] D. Kubair and S. Spearing, "Cohesive zone model for direct silicon wafer bonding," *Journal of Physics D: Applied Physics*, vol. 40, no. 10, p. 3070, 2007. (cited on page 22)

[62] D. V. Kubair, D. J. Cole, L. C. Ciacchi, and S. M. Spearing, "Multiscale mechanics modeling of direct silicon wafer bonding," *Scripta Materialia*, vol. 60, no. 12, pp. 1125–1128, 2009. (cited on page 22)

[63] D. V. Kubair and S. M. Spearing, "Cohesive zone modelling of wafer bonding and fracture: effect of patterning and toughness variations," *Journal of Physics D: Applied Physics*, vol. 39, no. 6, p. 1050, 2006. (cited on page 22)

[64] K. T. Turner, M. D. Thouless, and S. M. Spearing, "Mechanics of wafer bonding: Effect of clamping," *Journal of applied physics*, vol. 95, no. 1, pp. 349–355, 2004. (cited on pages 22, 23, 59 and 60)

[65] D. Feijoó, I. Ong, K. Mitani, W. Yang, S. Yu, and U. Gösele, "Prestressing of bonded wafers," in *Proceedings of the First International Symposium on Semiconductor Wafer Bonding: Science, Technology, and Applications*, vol. 92, 1991, p. 7. (cited on page 23)

[66] C. Himcinschi, M. Reiche, R. Scholz, S. Christiansen, and U. Gösele, "Compressive uniaxially strained silicon on insulator by prestrained wafer bonding and layer transfer," *Applied physics letters*, vol. 90, no. 23, pp. 231 909–231 909, 2007. (cited on page 23)

[67] C. Himcinschi, I. Radu, F. Muster, R. Singh, M. Reiche, M. Petzold, U. Gösele, and S. Christiansen, "Uniaxially strained silicon by wafer bonding and layer transfer," *Solid-State Electronics*, vol. 51, no. 2, pp. 226–230, 2007. (cited on page 23)

[68] K. T. Turner, "Fabricating strained silicon substrates using mechanical deformation during wafer bonding," *ECS Transactions*, vol. 16, no. 8, pp. 321–328, 2008. (cited on pages 23 and 60)

[69] M. Broekaart, A. Castex, K. Landry, R. Fontaniere, and C. Lagahe-Blanchard, "Distortion free wafer bonding technology for backside illumination image sensors," *ECS Transactions*, vol. 50, no. 7, pp. 371–377, 2013. (cited on page 23)

[70] G. Gaudin, G. Riou, D. Landru, C. Tempesta, I. Radu, M. Sadaka, K. Winstel, E. Kinser, and R. Hannon, "Low temperature direct wafer to wafer bonding for 3d integration: Direct bonding, surface preparation, wafer-to-wafer alignment," in *3D Systems Integration Conference (3DIC), 2010 IEEE International*, 2010, pp. 1–4. (cited on page 23)

[71] S. E. Steen, D. LaTulipe, A. W. Topol, D. J. Frank, K. Belote, and D. Posillico, "Overlay as the key to drive wafer scale 3d integration," *Microelectronic engineering*, vol. 84, no. 5, pp. 1412–1415, 2007. (cited on page 23)

[72] K. T. Turner, S. Veeraraghavan, and J. K. Sinha, "Predicting distortions and overlay errors due to wafer deformation during chucking on lithography scanners," *Journal of Micro/Nanolithography, MEMS, and MOEMS*, vol. 8, no. 4, pp. 043 015–043 015, 2009. (cited on page 23)

[73] K. T. Turner, S. Veeraraghavan, and J. K. Sinha, "Relationship between localized wafer shape changes induced by residual stress and overlay errors," *Journal of Micro/Nanolithography, MEMS, and MOEMS*, vol. 11, no. 1, pp. 013 001–1–013 001–8, 2012. (cited on page 23)

[74] K. T. Turner, "Wafer bonding: mechanics-based models and experiments," Ph.D. dissertation, Massachusetts Institute of Technology, 2004. (cited on page 24)

[75] K. T. Turner and S. M. Spearing, "Modeling of direct wafer bonding: Effect of wafer bow and etch patterns," *Journal of Applied Physics*, vol. 92, no. 12, pp. 7658–7666, 2002. (cited on pages 24 and 42)

[76] C. Majidi and R. S. Fearing, "Adhesion of an elastic plate to a sphere," *Proceedings of the Royal Society A: Mathematical, Physical and Engineering Science*, vol. 464, no. 2093, pp. 1309–1317, 2008. (cited on page 24)

[77] H. H. Yu and Z. Suo, "A model of wafer bonding by elastic accommodation," *Journal of the Mechanics and Physics of Solids*, vol. 46, no. 5, pp. 829–844, 1998. (cited on page 24)

[78] B. N. J. Persson, "Adhesion between an elastic body and a randomly rough hard surface," *The European Physical Journal E*, vol. 8, no. 4, pp. 385–401, 2002. (cited on page 24)

[79] A. G. Peressadko, N. Hosoda, and B. N. J. Persson, "Influence of surface roughness on adhesion between elastic bodies," *Phys. Rev. Lett.*, vol. 95, p. 124301, Sep 2005. (cited on page 24)

[80] B. Derjaguin, V. Muller, and Y. Toporov, "Effect of contact deformations on the adhesion of particles," *Journal of Colloid and Interface Science*, vol. 53, no. 2, pp. 314–326, 1975. (cited on pages 24 and 64)

[81] K. L. Johnson, K. Kendall, and A. D. Roberts, "Surface energy and the contact of elastic solids," *Proceedings of the Royal Society of London. A. Mathematical and Physical Sciences*, vol. 324, no. 1558, pp. 301–313, 1971. (cited on pages 24, 64 and 65)

[82] K. L. Johnson and J. A. Greenwood, "An adhesion map for the contact of elastic spheres," *Journal of Colloid and Interface Science*, vol. 192, no. 2, pp. 326–333, 1997. (cited on page 24)

[83] E. Barthel, "Adhesive elastic contacts: JKR and more," *Journal of Physics D: Applied Physics*, vol. 41, no. 16, p. 163001, 2008. (cited on page 24)

[84] J. A. Greenwood and J. B. P. Williamson, "Contact of nominally flat surfaces," *Proceedings of the Royal Society of London. Series A. Mathematical and Physical Sciences*, vol. 295, no. 1442, pp. 300–319, 1966. (cited on page 24)

[85] K. N. G. Fuller and D. Tabor, "The effect of surface roughness on the adhesion of elastic solids," *Proceedings of the Royal Society of London. A. Mathematical and Physical Sciences*, vol. 345, no. 1642, pp. 327–342, 1975. (cited on page 24)

[86] D. Maugis, "On the contact and adhesion of rough surfaces," *Journal of adhesion science and technology*, vol. 10, no. 2, pp. 161–175, 1996. (cited on page 24)

[87] C. Gui, M. Elwenspoek, N. Tas, and J. G. E. Gardeniers, "The effect of surface roughness on direct wafer bonding," *Journal of Applied Physics*, vol. 85, no. 10, pp. 7448–7454, 1999. (cited on page 24)

[88] F. Rieutord, H. Moriceau, R. Beneyton, L. Capello, C. Morales, and A.-M. Charvet, "Rough surface adhesion mechanisms for wafer bonding," *ECS Transactions*, vol. 3, no. 6, pp. 205–215, 2006. (cited on page 24)

[89] N. Miki and S. M. Spearing, "Effect of nanoscale surface roughness on the bonding energy of direct-bonded silicon wafers," *Journal of Applied Physics*, vol. 94, no. 10, pp. 6800–6806, 2003. (cited on page 24)

[90] P. Attard, "Interaction and deformation of elastic bodies: origin of adhesion hysteresis," *The Journal of Physical Chemistry B*, vol. 104, no. 45, pp. 10 635–10 641, 2000. (cited on page 25)

[91] A. Ghatak and M. K. Chaudhury, "Adhesion-induced instability patterns in thin confined elastic film," *Langmuir*, vol. 19, no. 7, pp. 2621–2631, 2003. (cited on page 25)

[92] W. P. Maszara, G. Goetz, A. Caviglia, and J. B. McKitterick, "Bonding of silicon wafers for silicon-on-insulator," *Journal of Applied Physics*, vol. 64, no. 10, pp. 4943–4950, 1988. (cited on pages 25, 26, 40 and 87)

[93] Ö. Vallin, K. Jonsson, and U. Lindberg, "Adhesion quantification methods for wafer bonding," *Materials Science and Engineering: R: Reports*, vol. 50, no. 4, pp. 109–165, 2005. (cited on pages 25 and 26)

[94] A. Milekhin, M. Friedrich, K. Hiller, M. Wiemer, T. Gessner, and D. Zahn, "Characterization of low-temperature wafer bonding by infrared spectroscopy," *Journal of Vacuum Science & Technology B: Microelectronics and Nanometer Structures*, vol. 18, no. 3, pp. 1392–1396, 2000. (cited on page 25)

[95] D. Feijoo, Y. Chabal, and S. B. Christman, "Silicon wafer bonding studied by infrared absorption spectroscopy," *Applied Physics Letters*, vol. 65, no. 20, pp. 2548–2550, 1994. (cited on page 25)

[96] C. Himcinschi, M. Friedrich, K. Hiller, T. Gessner, and D. Zahn, "Infrared spectroscopic investigations of the buried interface in silicon bonded wafers," *Semiconductor science and technology*, vol. 19, no. 5, p. 579, 2004. (cited on page 25)

[97] M. Weldon, Y. Chabal, D. Hamann, S. Christman, E. Chaban, and L. Feldman, "Physics and chemistry of silicon wafer bonding investigated by infrared absorption spectroscopy," *Journal of Vacuum Science & Technology B: Microelectronics and Nanometer Structures*, vol. 14, no. 4, pp. 3095–3106, 1996. (cited on page 25)

[98] F. Rieutord, J. Eymery, F. Fournel, D. Buttard, R. Oeser, O. Plantevin, H. Moriceau, and B. Aspar, "High-energy x-ray reflectivity of buried interfaces created by wafer bonding," *Physical Review B*, vol. 63, no. 12, pp. 125 408–125 408, 2001. (cited on page 25)

[99] C. Ventosa, F. Rieutord, L. Libralesso, C. Morales, F. Fournel, and H. Moriceau, "Hydrophilic low-temperature direct wafer bonding," *Journal of Applied Physics*, vol. 104, no. 12, 2008. (cited on pages 25 and 26)

[100] C. Ventosa, C. Morales, L. Libralesso, F. Fournel, A. Papon, D. Lafond, H. Moriceau, J. Penot, and F. Rieutord, "Mechanism of thermal silicon oxide direct wafer bonding," *Electrochemical and Solid-State Letters*, vol. 12, no. 10, pp. H373–H375, 2009. (cited on pages 25 and 26)

[101] K. Mitani and U. Gösele, "Formation of interface bubbles in bonded silicon wafers: a thermodynamic model," *Applied Physics A*, vol. 54, no. 6, pp. 543–552, 1992. (cited on page 25)

[102] S. Vincent, I. Radu, D. Landru, F. Letertre, and F. Rieutord, "A model of interface defect formation in silicon wafer bonding," *Applied Physics Letters*, vol. 94, no. 10, 2009. (cited on page 25)

[103] S. Vincent, J.-D. Penot, I. Radu, F. Letertre, and F. Rieutord, "Study of the formation, evolution, and dissolution of interfacial defects in silicon wafer bonding," *Journal of Applied Physics*, vol. 107, no. 9, 2010. (cited on page 25)

[104] S. Mack, H. Baumann, and U. Gösele, "Gas development at the interface of directly bonded silicon wafers: investigation on silicon-based pressure sensors," *Sensors and Actuators A: Physical*, vol. 56, no. 3, pp. 273–277, 1996. (cited on page 25)

[105] Reznicek, A and Scholz, R and Senz, S and Gösele, U, "Comparative tem study of bonded silicon/silicon interfaces fabricated by hydrophilic, hydrophobic and uhv wafer bonding," *Materials chemistry and physics*, vol. 81, no. 2, pp. 277–280, 2003. (cited on page 25)

[106] K. Scheerschmidt, D. Conrad, and U. Gösele, "Molecular dynamics simulations to investigate wafer bonded interfaces," *Computational Materials Science*, vol. 7, pp. 40 – 47, 1996. (cited on page 26)

[107] D. Conrad, K. Scheerschmidt, and U. Gösele, "Molecular dynamics simulations of silicon wafer bonding," *Applied Physics A*, vol. 62, no. 1, pp. 7–12, 1996. (cited on page 26)

[108] D. Conrad, K. Scheerschmidt, and U. Gösele, "Molecular dynamics studies of interacting hydrogenated si (001) surfaces," *Applied physics letters*, vol. 71, no. 16, pp. 2307–2309, 1997. (cited on page 26)

[109] P. Amirfeiz, S. Bengtsson, M. Bergh, E. Zanghellini, and L. Börjesson, "Formation of silicon structures by plasma-activated wafer bonding," *Journal of the Electrochemical Society*, vol. 147, no. 7, pp. 2693–2698, 2000. (cited on page 26)

[110] D. Pasquariello, C. Hedlund, and K. Hjort, "Oxidation and induced damage in oxygen plasma in situ wafer bonding," *Journal of the Electrochemical Society*, vol. 147, no. 7, pp. 2699–2703, 2000. (cited on page 26)

[111] T. Suni, K. Henttinen, I. Suni, and J. Mäkinen, "Effects of plasma activation on hydrophilic bonding of Si and SiO2," *Journal of the Electrochemical Society*, vol. 149, no. 6, pp. G348–G351, 2002. (cited on page 26)

[112] T. Plach, K. Hingerl, S. Tollabimazraehno, G. . Hesser, V. Dragoi, and M. Wimplinger, "Mechanisms for room temperature direct wafer bonding," *Journal of Applied Physics*, vol. 113, no. 9, pp. 094 905–094 905, 2013. (cited on page 26)

[113] T. Martini, J. Steinkirchner, and U. Gösele, "The crack opening method in silicon wafer bonding: How useful is it?" *Journal of The Electrochemical Society*, vol. 144, no. 1, pp. 354–357, 1997. (cited on page 26)

[114] J. Bagdahn, M. Petzold, M. Reiche, and K. Gutjahr, "Characterization of directly bonded silicon wafers by means of the double cantilever crack opening method," in *Proceedings of the Fourth International Symposium on Semiconductor Wafer Bonding: Science, Technology, and Applications, Electrochemical Society Proceedings Vol. PV97-36*, 1998, pp. 291–298. (cited on page 26)

[115] Y. Bertholet, F. Iker, J. Raskin, and T. Pardoen, "Steady-state measurement of wafer bonding cracking resistance," *Sensors and Actuators A*, vol. 110, pp. 157–163, 2004. (cited on page 26)

[116] V. Masteika, J. Kowal, N. S. J. Braitwaite, and T. Rogers, "The effect of atmospheric moisture on crack propagation in the interface between directly bonded silicon wafers," *Microsystem Technologies*, pp. 1–8, 2013. (cited on page 26)

[117] F. Fournel, L. Continni, C. Morales, J. Da Fonseca, H. Moriceau, F. Rieutord, A. Barthelemy, and I. Radu, "Measurement of bonding energy in an anhydrous nitrogen atmosphere and its application to silicon direct bonding technology," *Journal of Applied Physics*, vol. 111, no. 10, 2012. (cited on page 26)

[118] E. Navarro, Y. Bréchet, R. Moreau, T. Pardoen, J.-P. Raskin, A. Barthelemy, and I. Radu, "Direct silicon bonding dynamics: A coupled fluid/structure analysis," *Applied Physics Letters*, vol. 103, no. 3, p. 034104, 2013. (cited on page 35)

[119] K. J. Stahl, J. W. White, and K. L. Deckert, "Dynamic response of self-acting foil bearings," *IBM Journal of Research and Development*, pp. 513–520, 1974. (cited on page 35)

[120] M. Argentina, J. Skotheim, and L. Mahadevan, "Settling and Swimming of Flexible Fluid-Lubricated Foils," *Physical Review Letters*, vol. 99, no. 224503, pp. 1–5, 2007. (cited on page 35)

[121] A. E. Hosoi and L. Mahadevan, "Peeling , Healing , and Bursting in a Lubricated Elastic Sheet," *Physical Review Letters*, vol. 93, no. 13, 2004. (cited on page 35)

[122] S. Timoshenko and S. Woinowsky-Krieger, *Theory of plates and shells*, McGraw-Hill ed., 1959. (cited on pages 36, 60 and 68)

[123] M. Chipot and M. Luskin, "The compressible Reynolds Lubrication equation," *IMA Preprint*, no. 232, 1986. (cited on pages 36 and 44)

[124] L. D. Landau and E. M. Lifshitz, *Course of Theoretical Physics Vol 7: Theory of Elasticity*. Pergamon, 1969. (cited on pages 37 and 100)

[125] C. Majidi and G. Adams, "A simplified formulation of adhesion problems with elastic plates," *Proceedings of the Royal Society A*, no. February, pp. 1–14, 2009. (cited on pages 37, 52, 66 and 100)

[126] C. Majidi and G. Adams, "Adhesion and delamination boundary conditions for elastic plates with arbitrary contact shape," *Mechanics Research Communications*, vol. 37, no. 2, pp. 214–218, 2010. (cited on pages 37, 49, 66 and 100)

[127] P. G. de Gennes, "Wetting : statics and dynamics," *Reviews of Modern Physics*, vol. 57, no. 3, p. 827, 1985. (cited on page 43)

[128] N. G. Hadjiconstantinou, "The limits of Navier-Stokes theory and kinetic extensions for describing small-scale gaseous hydrodynamics," *Physics of Fluids*, vol. 18, no. 11, p. 111301, 2006. (cited on pages 43 and 99)

[129] P. Bahukudumbi and A. Beskok, "A phenomenological lubrication model for the entire knudsen regime," *Journal of Micromechanics and Microengineering*, vol. 13, no. 6, p. 873, 2003. (cited on page 43)

[130] Y. Peng, X. Lu, and J. Luo, "Nanoscale effect on ultrathin gas film lubrication in hard disk drive," *Journal of tribology*, vol. 126, no. 2, pp. 347–352, 2004. (cited on page 43)

[131] H. D. Bui, C. Guyon, and B. Thomas, "On viscous fluid flow near a moving crack tip," in *Continuum Thermomechanics*, ser. Solid Mechanics and Its Applications, G. A. Maugin, R. Drouot, and F. Sidoroff, Eds. Springer Netherlands, 2002, vol. 76, pp. 63–74. (cited on page 56)

[132] A. Castex, M. Broekaart, F. Rieutord, K. Landry, and C. Lagahe-Blanchard, "Mechanism of edge bonding void formation in hydrophilic direct wafer bonding," *ECS Solid State Letters*, vol. 2, no. 6, pp. P47–P50, 2013. (cited on page 56)

[133] L. B. Freund and S. Suresh, *Thin film materials: stress, defect formation and surface evolution*. Cambridge University Press, 2003. (cited on page 60)

[134] E. Ventsel and T. Krauthammer, *Thin Plates and Shells: Theory, Analysis, and Applications*, M. Dekker, Ed., 2001. (cited on pages 60 and 63)

[135] G. Barenblatt, "The formation of equilibrium cracks during brittle fracture. General ideas and hypotheses. Axially-symmetric cracks." *Journal of Applied Mathematics and Mechanics*, vol. 23, no. 3, pp. 434–444, 1959. (cited on page 63)

[136] M. A. Hopcroft, W. D. Nix, and T. W. Kenny, "What is the Young's Modulus of Silicon?" *Microelectromechanical Systems, Journal of*, vol. 19, no. 2, pp. 229–238, 2010. (cited on pages 70 and 71)

[137] M. Holz, S. R. Heil, and A. Sacco, "Temperature-dependent self-diffusion coefficients of water and six selected molecular liquids for calibration in accurate 1h nmr pfg measurements," *Physical Chemistry Chemical Physics*, vol. 2, no. 20, pp. 4740–4742, 2000. (cited on page 85)

[138] K. T. Turner and S. M. Spearing, "Accurate characterization of wafer bond toughness with the double cantilever specimen," *Journal of applied physics*, vol. 103, no. 1, p. 013514, 2008. (cited on page 87)

[139] D. Pasquariello and K. Hjort, "Mesa-spacers: Enabling nondestructive measurement of surface energy in room temperature wafer bonding," *Journal of the Electrochemical Society*, vol. 147, no. 6, pp. 2343–2346, 2000. (cited on page 87)

[140] Z. Zong, C.-L. Chen, M. R. Dokmeci, and K.-t. Wan, "Direct measurement of graphene adhesion on silicon surface by intercalation of nanoparticles," *Journal of Applied Physics*, vol. 107, no. 2, pp. 026 104–026 104, 2010. (cited on page 87)

[141] Y. Bertholet, "Measurement, optimization and multiscale modeling of silicon wafer bonding interface fracture resistance," Ph.D. dissertation, Ph. D thesis, Université Catholique de Louvain, 2006. (cited on page 87)

[142] E. Centurioni, "Generalized matrix method for calculation of internal light energy flux in mixed coherent and incoherent multilayers," *Applied Optics*, vol. 44, no. 35, pp. 7532–7539, 2005. (cited on page 103)